January 2012

Novel blends of sulfur-tolerant water-gas shift catalysts for biofuel applications

Timothy Michael Roberge
University of South Florida, troberge@mail.usf.edu

Novel Blends of Sulfur-Tolerant Water-Gas Shift Catalysts

for Biofuel Applications

by

Timothy Michael Roberge

A thesis submitted in partial fulfillment
of the requirements for the degree of
Master of Science in Chemical Engineering
Department of Chemical and Biomedical Engineering
College of Engineering
University of South Florida

Major Professor: John N. Kuhn, Ph.D.
Aydin Sunol, Ph.D.
Scott Campbell, Ph.D.

Date of Approval:
March 9, 2012

Keywords: spinel, WGS, ceria, molybdenum doping, cobalt

DEDICATION

This work is dedicated to Karen, without whose love, patience, and temperament, this thesis would ne'er be written.

This work is dedicated to Sophie; who always maintained I should "be busy", especially at bedtime. I will always cherish your involvement with this work.

This work is dedicated to Samantha; your coming to the world was the catalyst for completing this process. Your addition to the family fills me with such peace and hope.

This work is dedicated to Tom McFarland, whose proclivity for encouragement was a great source of motivation for this work.

This work is dedicated to my parents, who instilled the importance of hard work and character in all my ventures.

This work is dedicated to all fathers who study, work, and strive to be a positive force in their family, for their community, for their country, and for their field of expertise.

ACKNOWLEDGEMENTS

I would like to thank my mentor, Dr. John Kuhn, for his invaluable mentorship for this project. I would not be able to finish this process without his trust and support. If ever I had a question or problem, Dr. Kuhn, like any great mentor, would lead me to think for myself based on engineering principles that he knew I already understood. I will always appreciate the fact that he encouraged me to learn on my own. Dr. Kuhn always stressed the importance of organization, preparation, and hard work. I am indebted to him for his well- researched presentations, courses, and vast knowledge of current trends in literature and beyond. I've learned many things by simply being around the culture of learning he has promoted for his students' well-being.

I would also like to thank Dr. Paul Matter and his company pH Matter for funding this research.

I am personally grateful to Selasi Blavo for his assistance on this project. When my course load inhibited my involvement, Selasi was able to run characterization experiments to keep this project going.

I am thankful for the personal network of support that our research group had during my tenure as a graduate student: Sandy Pettit, Vanessa Castillo, Selma Hokenek, Michael Mankbadi, Erum Qayyum, Devin Walker, Lyndsey Baldyga, Yolanda Daza and Selasi Blavo. Each one of these members was influential in one way or another.

I'd also like to thank my committee members Drs. Aydin Sunol and Scott Campbell for serving on my committee. Since my under-graduate experience was also at USF, I was especially blessed to have Dr. Sunol, whose mentorship for my senior design project was invaluable. I would not have been able to complete my Bachelor's degree without his insight.

In my thanks to Dr. Campbell, I want to specifically point out his amazing ability to explain the most complex phenomena in simple terms. Any chemical engineering principle I had struggled with was brought to conscious understanding by Dr. Campbell's facilitating ability to teach.

I would be remiss not to acknowledge other instrumental faculty members in the Department of Chemical and Biomedical Engineering at USF. From my first engineering course, Dr. Vinay Gupta stressed the importance of hard work, the correlation between success and will, and being fearless in self-expression. His teaching left an indelible impression on me.

I'd also like to thank the late Dr. John Wolan for his contribution to my education. His simple, light demeanor made learning complex reaction phenomena a joy. It was noticeable that he took great pleasure in relaying his pedagogic gift via illustrations, stories, and unforgettable examples.

I'd also like to thank Dr. Babu Joseph for his disciplined and thoughtful approach to learning. I learned a lot from his teaching, and am forever indebted to his integration of culture and history into the lectures.

I'd also like to acknowledge Mrs. Sheryl Sippel at Hillsborough Community College. She was the catalyst for my engineering degree. In the summer of 2008, I had not taken any math beyond a high school level, and was ignorant of basic mathematical operations and

terms. Her simple, illuminating teaching style for pre-calculus and trigonometry allotted me the necessary confidence I needed to go forward. She alone installed the mathematical bases which have allowed me to proceed to this point.

I would also like to acknowledge my high school chemistry teacher, Mr. Morneault. His inspiring teaching style gave birth to my inquisitiveness in science.

A chemical engineering degree requires much hard work, and there are two fellow students I'd like to acknowledge in particular: Justin Thomas and Dustin Begosh-Mayne. In addition to a one-of-a-kind personality, Justin was also a gentleman who worked very efficiently. I always knew I could count on him for that which I had to grasp. Dustin was my best friend throughout my collegiate experience. His friendship was invaluable to me. Not only was he very knowledgeable, but extremely giving and very helpful. Any personal struggle I encountered, he always deflected with an ever affable demeanor. He worked hard, and challenged me to maintain the course with confidence. It's safe to say, I would not have graduated without his friendship or teamwork.

I'd also like to acknowledge the investment that members of my family have incorporated in me. My parents instilled the value of determination and hard work ever since I was a youngster. Without the values they tirelessly inculcated, I would have quit along the way. My grandfather, Thomas McFarland, was always very supportive of my education. His friendship, kind words, and example were important ingredients I needed to persevere. I'd also like to acknowledge Patricia Roberge, whose generosity toward my family was very supportive and reassuring.

Finally, I could not have arrived at this point without the love and sacrifices of my lovely wife, Karen Roberge. She stood by me through thick and thin, giving meaning to the phrase 'for better or for worse'. Her faith in me was the most profound motivation I could ask for. Her resolve is laudable and beyond inspirational.

Lastly, I am indebted to He who makes all things possible. Thank You for opening doors and for keeping me on the right path.

TABLE OF CONTENTS

LIST OF TABLES

LIST OF FIGURES

ABSTRACT

As traditional sources of energy become depleted, significant research interest has gone into conversion of biomass into renewable fuels. Biomass-derived synthesis gas typically contains concentrations of approximately 30 to 600 ppm H_2S in stream. H_2S is a catalyst poison which adversely affects downstream processing of hydrogen for gas to liquid plants. The water-gas shift reaction is an integral part of converting CO and steam to H_2 and CO_2. Currently, all known water-gas shift catalysts deactivate in sulfur concentrations typical of biomass-derived synthesis gas. Novel catalysts are needed to remain active in the presence of sulfur concentrations in order to boost efficiency and mitigate costs. Previous studies have shown molybdenum to be active in concentrations of sulfur greater than 300 ppm. Cobalt has been shown to be active as a spinel in concentrations of sulfur less than 240 ppm. Ceria has received attention as a WGS catalyst due to its oxygen donating properties. These elements were synthesized via Pechini's method into various blends of spinel metal oxide solutions. Initial activity testing at lower steam to gas ratios produced near equilibrium conversions for a Ce-Co spinel which

remained active in 500 ppm H_2S over a temperature range of 350 °C to 400 °C. The catalysts became poisoned and deactivated in higher concentrations of sulfur. Addition of molybdenum to the Ce-Co base had little effect on sulfur tolerance, but it did lead to a reduction in selectivity for methanation. Surface area increased due to adsorbed H_2S, and X-Ray Diffraction confirmed that bulk sulfiding did not occur. Incorporation of Ce and Co into a Fe spinel hindered conversion at lower temperatures and deactivated in higher levels of sulfur.

CHAPTER I: INTRODUCTION

Background for Research

Petroleum Economy

Traditionally, petroleum has been the basis for the world's energy needs. Global production of oil is 86,790,349 million barrels per day. Global consumption of oil is 85,295,571 million barrels per day [1]. However, petroleum reserves are of finite value. A U.S. government report in 2011 estimates the world's total proven reserves at 1471.2 billion barrels [2]. Unless more reserves are discovered, at the current rate of production, the world's proven reserves would be depleted in 46.44 years. Table 1, adapted from the International Energy Outlook Report [2], provides a geographical portrayal of the world's petroleum reserves. Per Central Intelligence Agency estimates [3], the U.S. consumes 19,150,000 barrels/day. The U.S. has a 1.41 % share of the world's total petroleum reserves. At the current rate of consumption, U.S. reserves would be exhausted in less than 3 years. Therefore, there is a need to import energy from other parts of the world. Efforts for energy independence have long been in the public square as a key U.S. interest. Dependency on foreign import is harmful for America's economy and interests.

Table 1: Proven oil reserves by country.

Country	Proven Oil Reserves (billion barrels)	% of World Total
Saudi Arabia	211.2	14.35
Venezuela	211.2	14.35
Canada	175.2	11.91
Iran	137.0	9.31
Iraq	115.0	7.82
Kuwait	101.5	6.90
UAE	97.8	6.65
Russia	60.0	4.08
Libya	46.4	3.16
Nigeria	37.2	2.53
Kazakhstan	30.0	2.04
Qatar	25.4	1.73
US	20.7	1.41
China	20.4	1.38
Brazil	12.9	0.87
Algeria	12.2	0.83
Mexico	10.4	0.71
Angola	9.5	0.65
Azerbaijan	7.0	0.48
Ecuador	6.5	0.44
Rest of World	74.9	5.09
Total	**1471.2**	**100**

In addition to the limited supply and political considerations, environmental concerns also exist about traditional petroleum-derived energy sources. Petroleum derived fuels are known to produce higher levels of greenhouse gases. The vast majority of greenhouse gas emissions are caused by combustion cycles of hydrocarbons [4]. In

2008, nearly 6000 metric tons of CO_2 were emitted into the atmosphere from the U.S. alone. Almost half of these emissions were from petroleum-derived fuels alone.

Due to these issues, the importance to seek out alternative energy sources is a necessity. Much of the recent focus is on converting renewable feedstock into usable fuel. Table 2, adapted from the U.S. Energy Information Administration [5], provides an overview of energy use in the United States over the past several years.

Table 2: U.S. energy consumption by energy source, 2005 – 2009. Figures are in quadrillion BTU.

Energy Source	2005	2006	2007	2008	2009
Fossil Fuels	85.815	84.687	86.223	83.532	78.631
Coal	22.797	22.447	22.749	22.398	19.996
Coal Coke Net Imports	0.045	0.061	0.025	0.040	-0.023
Natural Gas	22.583	22.224	23.679	23.814	23.416
Petroleum	40.391	39.955	39.769	37.279	35.242
Electricity Net Imports	0.084	0.063	0.106	0.113	0.116
Nuclear Electric Power	8.161	8.215	8.455	8.427	8.328
Renewable Energy	6.407	6.825	6.719	7.367	7.745
Biomass	3.117	3.277	3.503	3.852	3.884
Biofuels	0.577	0.771	0.991	1.372	1.546
Waste	0.403	0.397	0.413	0.436	0.447
Wood and Derived Fuels	2.136	2.109	2.098	2.044	1.891
Geothermal Energy	0.343	0.343	0.349	0.360	0.373
Hydroelectric Conventional	2.703	2.869	2.446	2.512	2.682
Solar Thermal/PV Energy	0.066	0.072	0.081	0.097	0.109
Total	**100.468**	**99.790**	**101.502**	**99.438**	**94.820**

Table 2 shows a slight trend of diminishing dependence of fossil fuels, while maintaining an uptick in use of renewable fuels. As of 2009, 8% of all energy consumption is from renewable sources. Figure 1 depicts the sources of total U.S. energy consumption in percentages.

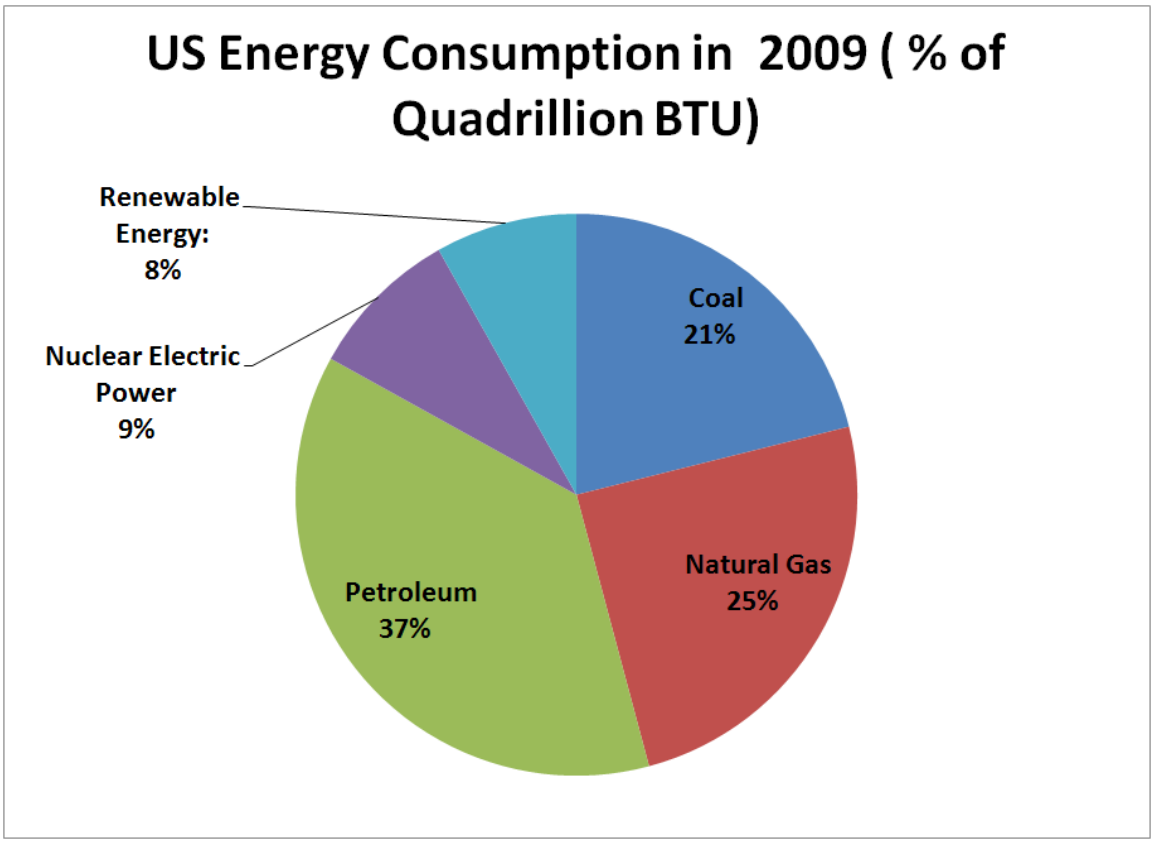

Figure 1: U.S. consumption of energy. (Total 94,820 quadrillion BTU.)

Biomass

As indicated in Table 2, biomass is expected to become a major source for renewable fuels. The sector which consumes the most biomass-derived energy is the industrial sector [5]. Coupled by policy changes and best practices, the U.S. Air-Force (USAF) has committed to supply 50% of energy for its continental fleet from domestic synthetic sources [6]. Huber et al. [7] provide an excellent review of biomass and current processes of transitioning raw feedstock into usable fuel. Biomass feedstock includes wood, logging residues, agricultural wastes, grass, corn, sugar cane, and hyacinth. Other feedstock can come from landfills and agricultural waste. Historically, in the interwar period, approximately 1 million European vehicles were fueled from a biomass source [8]. In 2002, 10-14% of the world's energy was estimated to be supplied from biomass [9]. Per the Department of Energy, 3% of total U.S. energy is derived from biomass [10]. This number is growing. In 2009, other government agencies reported an increase to 4% [5]. In 2010, almost half of the biomass-produced energy was derived from wood feed [11]. One major factor contributing to the attractiveness of biomass is the reduction of CO_2 emissions [6], as well as the ability to utilize carbon sequestration technology for hydrogen plants.

Gasification

Partial oxidation is an environmentally attractive way of turning carbonaceous feed into usable fuel. Due to high temperatures and pressures and spontaneous combustion with O_2, a self-sustaining pyrolysis reaction produces syngas, a mixture of CO, H_2, CO_2, CH_4, H_2S, COS, and a variety of other impurities. This reaction does not require the aid of a catalyst. The ratio of H_2/CO varies based on the feedstock. After pyrolysis, gasifier effluent is then processed downstream for a variety of applications (sulfuric acid plants, Fischer-Tropsch synthesis). A major factor impeding widespread use of gasification is high capital investment costs. In a previous work, the upfront capital cost for a gasifier island for a standard biomass to liquid (BTL) plant was found to be $1.5 billion dollars [12-13] (biomass and coal feed= 4000 tons/day). This high cost was the major factor adversely affecting the feasibility of converting biomass into a No. 2 crude distillate analog. The current price of diesel ($3.783/gallon) [14], coupled with oil prices currently in excess of $100/barrel [15], decries the economical attractiveness of biomass feedstock. Estimations of cost range from $16 to $70 per dry ton [16]. Florida is the leading producer of biomass in the U.S. [17]. In order to effectively use this resource, reduction in cost for large scale

gasification technology is a must, or the price of petroleum-derived fuel must spike.

Hydrogen

Traditional industrial processes requiring hydrogen are hydrotreating, ammonia synthesis, Fischer-Tropsch synthesis, and fuel cells. The latter two industries for hydrogen have received a lot of attention recently [18-20]. Hydrogen's ability to oxidize to water makes it an environmentally benign fuel. It also holds the highest energy content per unit weight: 143 GJ/ton [21]. As traditional energy resources deplete, hydrogen boasts to be the energy source of the future, due to its adaptability to service both electricity power generation and transportation. The development of hydrogen technology is sought by many industries.

Hydrogen Production

Though many hurdles of production, storage, transport, and cost effectiveness [18] remain, transitioning from a petroleum-based economy to a hydrogen economy is a necessity. Some estimate the transition could come as early as 2050 [22], due to the depletion of proven petroleum reserves. By 2030, the DOE intends to replace at least one-tenth of its current annual energy consumption with

hydrogen power [23]. There are many methods of hydrogen production. T-Raissi et al. [24] provide an excellent review of current production methods in comparison to steam reforming. Table 3, adapted from T-Raissi et al. [24], compares the different methods of hydrogen production. Nuclear power also is another method of hydrogen production currently being researched [25]. Various nuclear reactors have been proposed as a future avenue of hydrogen generation [26].

Table 3: Development and costs of various forms of hydrogen production.

Hydrogen Production Process	Status of Technology	Costs Relative to Methane Reforming	Percentage of Total Production
Steam Methane Reforming	Mature	1	48
Methane Pyrolysis	R&D to Mature	0.9	
H_2S Methane Reforming	R&D	<1	
Partial Oxidation of Heavy Oils	Mature	1.8	30
Naphtha Reforming	Mature		
Steam Reforming of Waste Oils	R&D	<1	
Coal Gasification	Mature	1.4-2.6	
Partial Oxidation of Coal	Mature		18
Steam-Iron Process	R&D	1.9	
Chloralkali Electrolysis	Mature	By-product	4

Table 3 (Continued)

Grid Electrolysis of Water	R&D	3-10	
Solar Electrolysis of Water	R&D to mature	>3	
High-Temperature Electrolysis of Water	R&D	2.2	
Thermochemical Water Splitting Cycles	Early R&D	6	
Biomass Gasification	R&D	2.0-2.4	
Photobiological	Early R&D		
Photolysis of Water	Early R&D		
Hydrogen Production Process	Status of Technology	Costs Relative to Methane Reforming	Percentage of Total Production
Photoelectrical Decomposition of Water	Early R&D		
Photocatalytic Decomposition of Water	Early R&D		

Steam reforming of methane is the most common form of obtaining hydrogen. 95% of the hydrogen in the U.S. market today is produced from natural gas [27]. Though steam reforming is energy intensive, it generates hydrogen for other chemical processes, chiefly ammonia synthesis and hydrotreating. It is noteworthy to point out that hydrogen generated from natural gas costs three times more in $/BTU than the natural gas itself [24]. Catalysts and new processes are to

play a major role in making a hydrogen economy more economically viable [28]. Steam reforming reaction is as follows:

$$CH_4 + H_2O \rightleftharpoons CO + 3H_2: \qquad \Delta H^\circ = 206.3\ \frac{kJ}{mol} \qquad (1)$$

Effluent CO can be further converted to hydrogen via the water-gas shift reaction (WGS):

$$CO + H_2O \rightleftharpoons CO_2 + H_2: \qquad \Delta H^\circ = -41.1\ \frac{kJ}{mol} \qquad (2)$$

Water-Gas Shift Reaction

The water-gas shift (WGS) is an important industrial reaction used in many processes to produce and purify hydrogen. The discovery of the WGS reaction is attributed to Felice Fontana in 1780 [29]. The reaction was first reported in 1888 [30], but its industrial importance came into prominence with the installation of Haber process in NH_3 plants. Ammonia processes require a CO free feed to complete the NH_3 synthesis loop in 1913 [31]. Unconverted CO poisons NH_3 catalysts downstream. Though the reaction is equilibrium limited, it converts most of the inlet CO. Less than 0.5 % of the CO feed remains in stream [32], and a methanation step is required to convert any residual CO (block diagram shown in Figure 5) [33]. The WGS is a

secondary means of producing hydrogen by converting any remaining CO to H_2 in synthesis gas streams. The WGS is also an important way to set a proper H_2/CO ratio for gas to liquid (GTL) processes. The Fischer-Tropsch reaction's activity is highly dependent on the inlet ratio. A stoichiometric feed (approximately 2:1 H_2/CO) yields higher conversions of liquid hydrocarbon fuel analogous to crude distillates [34] over cobalt-based catalysts.

WGS Thermodynamics

The standard heat of reaction for the mildly exothermic WGS reaction is -41.1 kJ/mol. The empirical value for K_p is given by the following expression [35]:

$$K_p = e^{\frac{4577.8}{T} - 4.33} \tag{3}$$

This expression is valid over a temperature range of 315 °C – 415 °C. Recall that for the WGS:

$$K_p = \frac{P_{H_2} P_{CO_2}}{P_{CO} P_{H_2O}} \tag{4}$$

Assuming Ideal Gas, $K_p = K_c = K$. Also recall Gibbs thermodynamic relationship relating the equilibrium constant with the change in free energy:

$$-\Delta G = RTln(K) \tag{5}$$

A detailed derivation can be found in Appendix I of the equilibrium constant with ideal gas conditions. This graph was calculated with values compiled by Smith, Van Ness, and Abbott [36]. Figure 2 shows K_p as a function of temperature. Values are computed from an ideal gas assumption. Equation 3 was not used.

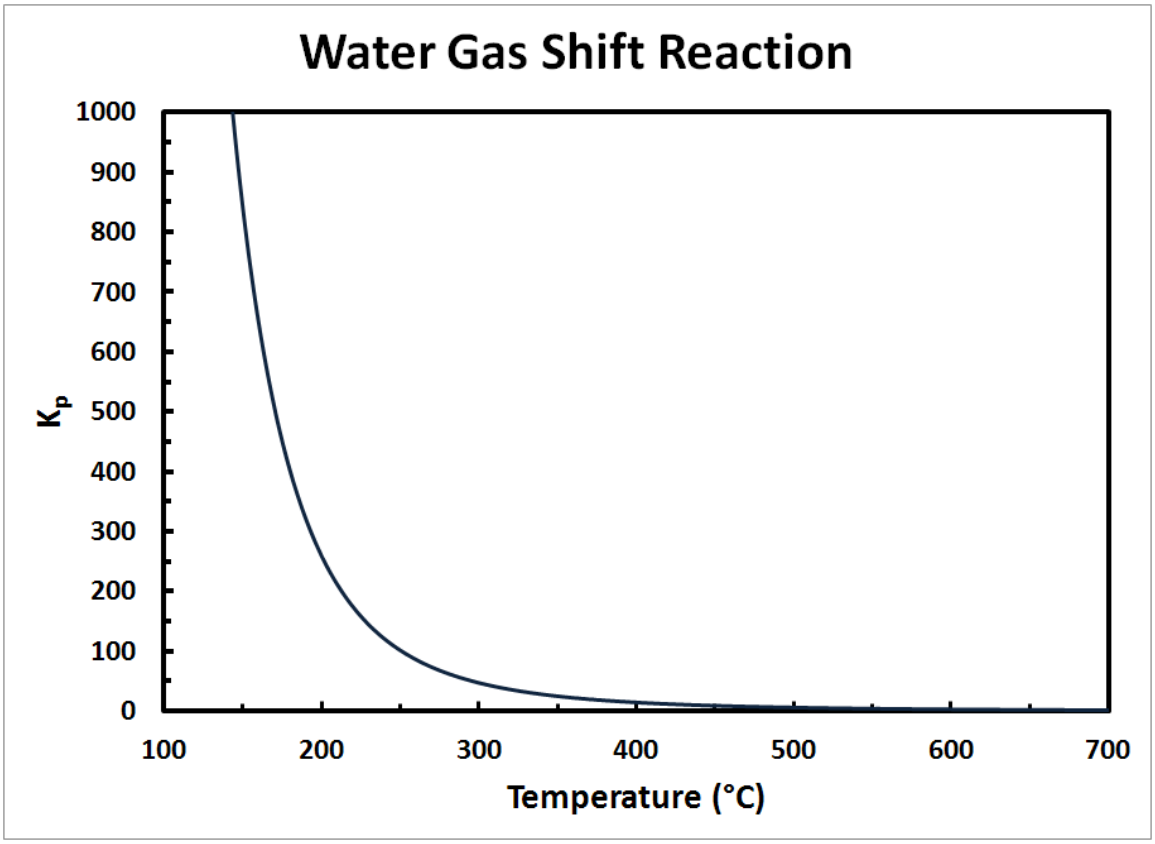

Figure 2: WGS K_p vs. temperature. Ideal gas assumed.

The amount of reactants has an effect on the equilibrium concentration. The equilibrium conversion also varies with the amount of reactants. Higher S/G ratios (excess steam) lead to greater

flexibility in conversion. Lower S/G ratios lessen the amount of CO conversion available at a certain temperature. Figure 3 shows equilibrium conversion for an S/G ratio of 1, as it is the ratio being reported in this work. For processes requiring complete CO conversion, higher S/G ratios are required by thermodynamics. Ratnasamy and Wagner [33] have an excellent overview of the WGS thermodynamics for the interested reader.

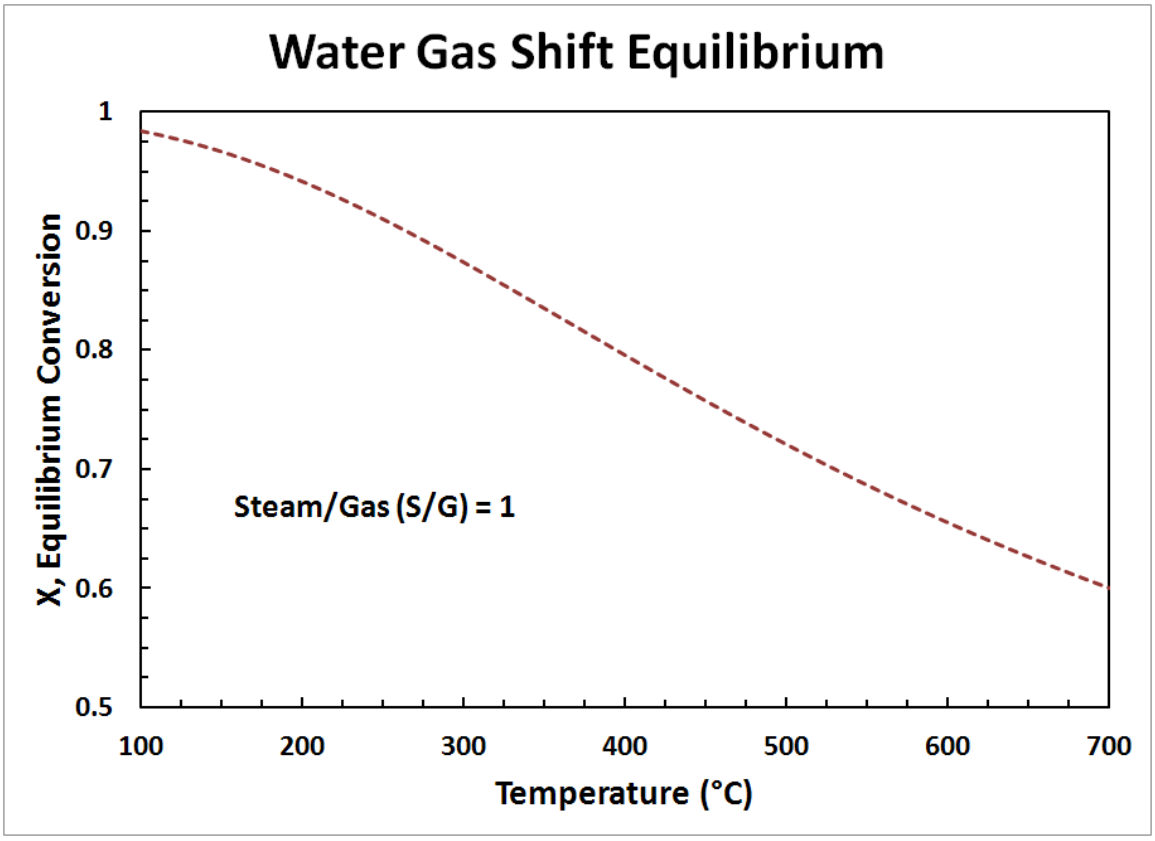

Figure 3: WGS equilibrium conversion as a function of temperature. S/G = 1.

For comparison, the ideal gas assumption is not far away from observed values reported in literature. Figure 4 shows a comparison of the two. The ideal gas assumption with the values and derivation found in Smith, Van Ness, and Abbott's Introduction to Chemical Engineering Thermodynamics have slightly better conversion than literature values. There is approximately a 2 – 2.5 percent variation between the two models.

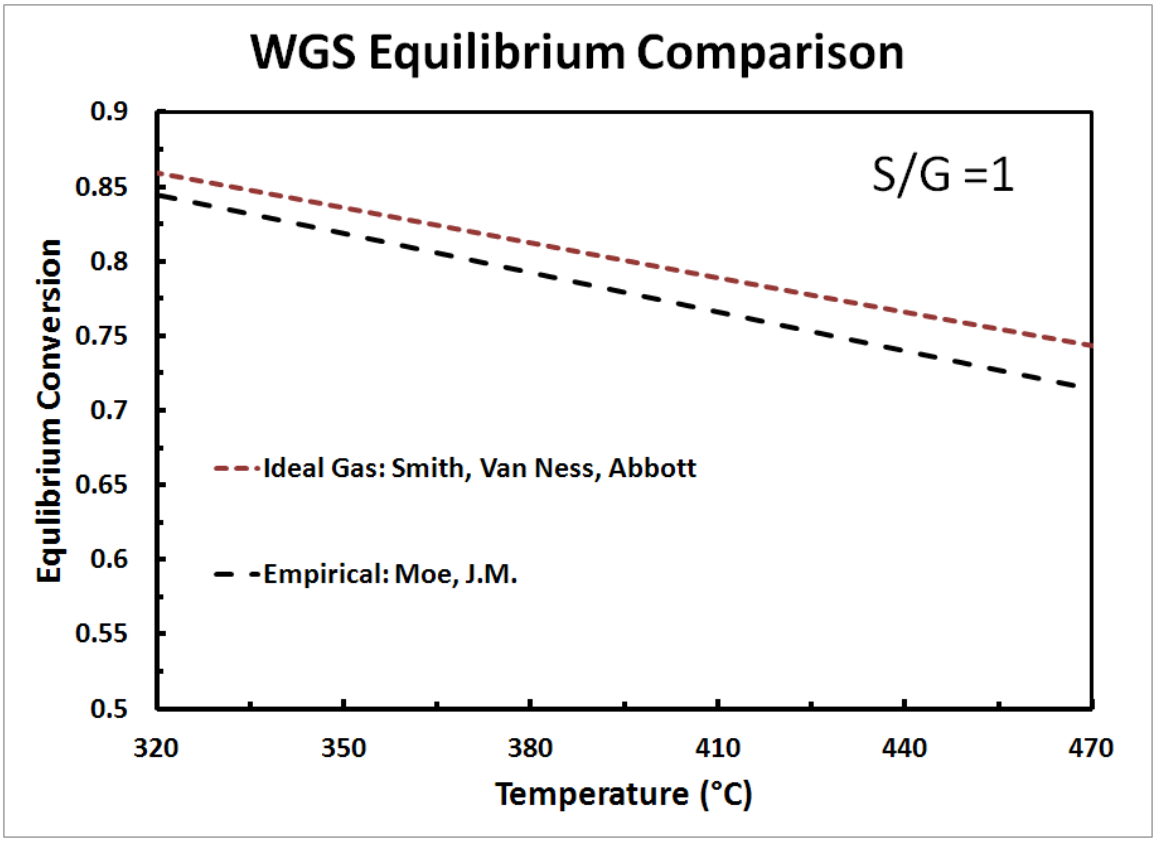

Figure 4: Comparison of equilibrium conversion. The blue line was calculated with equation 3 via Moe's widely used empirical correlation. The red line was calculated with ideal gas assumptions and directly from Gibbs free energy of formation, and enthalpy of formation.

Water-Gas Shift Reaction in Industry

Due to its industrial importance, the WGS reaction has been studied extensively in literature. The WGS process is typically the next stage after reforming or syngas generation step. A series of adiabatic reactors are used for CO shift processes. There are three types of WGS catalysts currently used in industry. Chromium supported magnetite catalysts promote the reaction at a temperature range of 350 °C - 450 °C [33, 37]. These are called High Temperature Shift (HTS) catalysts. These catalysts are not active below 350 °C. Because thermodynamics requires temperatures less than 300 °C for near complete conversion, a second reactor is needed to convert residual CO exiting the HTS reactor at lower temperatures. Copper Cu-ZnO-Al_2O_3 catalysts are used at a temperature range of 190 °C - 250 °C. These are dubbed Low Temperature Shift (LTS) catalysts. A third type of catalyst is the sulfur dependent Co-Mo based oxides. Once sulfided, they operate at a temperature of 250 °C - 350 °C. These are called Sour Gas Shift (SGS) catalysts.

Ratnasamy and Wagner [33] elucidate the syngas generation, CO shift, and NH_3 synthesis. Figure 5 shows a block diagram of hydrogen production for downstream use in a standard ammonia plant. Because the WGS is thermodynamically favored at lower temperatures, but

kinetically favored at higher temperatures, the WGS transpires over a series of 2 reactors. Because complete conversion is unattainable, any residual CO must be eliminated before entering the NH_3 reactors. Methanation of residual CO ensures that NH_3 catalysts will remain uncontaminated from CO deactivation.

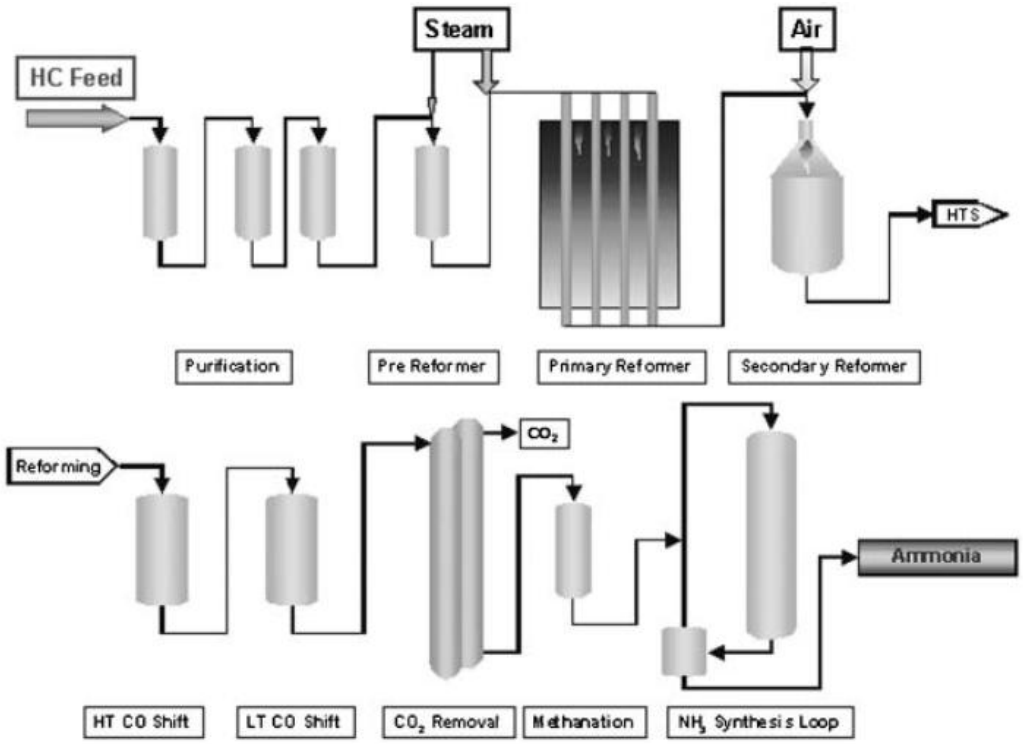

Figure 5: Steam reforming of natural gas for syngas generation for ammonia synthesis. [33] (Reprinted with permission from Taylor & Francis)

HTS Catalysts

Fe_2O_3-Cr_2O_3 catalysts have been used for many years in WGS catalysis. They were first introduced in 1914 by Bausch and Wild [38]. Because they achieved near equilibrium conversions at temperatures

greater than 500 °C, they have remained essentially unchanged for over 50 years. The Cr_2O_3 supports the hematite and prevents thermal sintering [33, 37]. In order to be effective, the Fe_2O_3-Cr_2O_3 must be reduced to Fe_3O_4-CrO_3 phase [39]. The magnetite phase is responsible for catalyzing the WGS via a redox mechanism [40-41]. In typical industrial conditions, inlet CO weight percentage from the reformer is 9% accompanying other inerts such as N_2 in the syngas feed. Exit concentrations are 3% weight CO. Since molar volume is unchanged during the reaction, pressure has negligible effect on the thermodynamics. Higher pressure does help the kinetics over the ferrochrome catalysts [33]. Typical HTS reactor pressures range from 10 – 60 bar [33].

LTS Catalysts

Cu-ZnO-Al_2O_3 catalysts are used to further convert HTS effluent CO to H_2. Prior to entering the reactor, the stream is cooled to about 190 °C – 230 °C. LTS effluent CO can be 0.3% weight. Since even trace amounts of CO are harmful to the catalysts used in NH_3 synthesis, the residual CO is converted to methane [33]. Cu-ZnO-Al_2O_3 catalysts are extremely susceptible to trace amounts of sulfur. When poisoned, activity declines irreversibly. Thus, typical LTS reactors are three times the size required by kinetic modeling [33].

Effect of Sulfur

One of the drawbacks of gasifying biomass, apart from high capital start up expenses, is the sulfur content in stream. Sulfur is a catalyst poison which can adversely affect downstream processing of hydrogen. It poisons catalysts by sulfiding the catalytic surface via the following general reaction [42]:

$$M_xO_y + y\ H_2S \rightleftharpoons M_xS_y + y\ H_2O \tag{6}$$

where M denotes any transition metal.

Though some report that most metal catalysts can be fully regenerated by removing the sulfur from the stream and flowing steam over them [43], LTS Cu based catalysts are irreversibly deactivated even in trace amounts of sulfur [37]. Under process conditions, this may be difficult to accomplish without losing productivity. Cheah et al. [42] also did a comprehensive literature review of existing levels of sulfur in synthesis gas depending on biomass source. Their findings are shown in Table 4.

Table 4: Levels of H_2S from various biomass sources. [42]

Biomass source	Concentration (ppm H_2S) (dry basis)
Wood	50-230
Wood chips	<50
Wood	20-50
Herbaceous feedstock	300-600
Wood	40-120
Dried sewage sludge	300

Sulfur Removal in Industry

Desulfurization takes place with reaction of ZnO at 370 °C. Copper-loaded charcoal also absorbs H_2S at ambient temperatures. Naphtha desulfurization or natural gas hydrodesulfurization techniques are efficient enough to not warrant sulfur-tolerant catalysts. The HTS ferrochrome catalysts are still active in the presence of sulfur, yet their activity is diminished when in a sulfide state [37]. The electronic structure of H_2S causes it to bond strongly to transitional metals, though they are fairly stable in concentrations of sulfur less than 50 ppm [44]. For coal and biomass derived syngas, CO and H_2S levels are much higher. When traditional WGS catalysts were tested in just 200 ppm H_2S, there was an over 50% decline in activity [45]. Sulfur-tolerant catalysts are needed for these streams. In lieu of operating at higher H_2O/CO (S/G) ratios, sulfur is removed before entering the HTS

reactor by a Co-Mo catalyst. These catalysts are supported on aluminum.

Removing sulfur from the stream, these catalysts convert CO into H_2 via the WGS reaction. Therefore, Co-Mo sulfides are sour-gas shift catalysts. Hakkarainen et al. [46] reviewed the kinetics of the WGS reaction over these catalysts with a spinning basket reactor. They noted that the activity diminished substantially at temperatures greater than 350 °C. They also determined that after a surface reaction took place, desorption of CO_2 was the rate determining step. They are not active in an oxide state, and need to be sulfided in order to remain active. The threshold sulfided concentration in literature is ambiguous. Ratnasamy and Wagner report a minimal level of H_2S of 300 ppm [33]. Liu et al. [47] report 1000 ppm of sulfur is needed to remain totally sulfided. Other sources corroborate Ratnasamy and Wagner's value [48-49].

Overview of WGS Technologies

Table 5 is adapted from the Department of Energy's Hydrogen from Coal Multi-Year RD@D Plan [50]. This table provides an overview of existing WGS processes. COS is another sulfur compound found in synthesis gas streams which can adversely affect downstream

processing. COS conversion in this table refers to conversion to less harmful sulfur compounds, such as CS_2 or H_2S.

Table 5: Overview of current WGS processes.

Performance Criteria	Units	LTS	HTS	SGS
Catalyst form		Pellets	Pellets	Pellets
Active Metals		Cu/Zn & Cu/Zn/Al	Fe/Cr	Co/Mo
Reactor Type		Multiple fixed beds	Multiple fixed beds	Multiple fixed beds
Temperature	°C	200-300	300-500	250-550
Pressure	psia	~450	450-750	~1100
CO in Feed		Low	Moderate to high	High
Residual CO	%	0.1-0.3	3.2-8.0	0.8-1.6
Min S/G	Molar	2.6	2.8	2.8
Sulfur Tolerance	ppmv	Less than 0.1	Less than 100	Greater than 300
COS conversion		No	No	Yes
Chloride tolerance		Low	Moderate	Moderate
Stability/Durability	Years	3-5	5-7	2-7

It is interesting to note that all the industrial reactors use an S/G ratio greater than 2. Providing the market a catalyst which can operate in smaller ratios will reduce the amount of material needed. Typical Gas Hourly Space Velocities (GHSV) used in industrial practices are 1.2 x 10^6 hr^{-1} [33]. As will be discussed in greater detail in Chapter IV, this table clearly shows an existing gap in the sulfur tolerance of WGS shift catalysts.

CHAPTER II: REVIEW OF SULFUR IN WGS CATALYSIS

Sulfur-Tolerant WGS Catalysts in Literature

Since alumina supported Co-Mo oxides were used in Texaco's desulfurization of a heavy oil [51], some research has gone into creating novel sulfur-tolerant catalysts. Newsome, in his review of WGS catalysts, predicted their use for coal derived syngas and processes [37]. De la Osa et al. did an excellent review of these Co-Mo catalysts [52]. After sulfidation, they were able to determine that approximately 100 ppm H_2S was necessary to maintain activity. It was also viable even at higher temperatures of 500 °C, with 450 °C giving the best conversion. Conversion decreased with increasing GHSV. There was a trend of adding alkali metals such as K and Ni to the Co-Mo support [53-56]. Greater activity levels were observed by doing this, with the highest being a K-promoted Ni-Mo alloy. At a S/G ratio of 3, CO conversion increased substantially to near equilibrium conversions at 400 °C [53] (Equilibrium conversion was not provided in this publication). Time on stream studies show a decline in activity for 5 hours with acceptable conversion levels (80%) stabilizing after 6 hours on stream.

In light of needing sulfur levels above 300 ppm in sour gas streams, other materials have been investigated for sulfur-tolerant properties. In 1990, Copperthwaite et al. [48] published a review on $CoCr_2O_4$, which was tested at 300 °C. The catalyst deactivated at 240 ppm H_2S. The incorporation of cobalt into the Cr-spinel exhibits sulfur tolerance up until the ~ 250 ppm levels. Molybdenum, on the other hand, requires levels above 300 ppm to remain active. Copper-thwaite's objective was to find a catalyst that would maintain activity higher than the existing ferrochrome catalysts in streams with or without sulfur. In other words, he sought a true sulfur-tolerant catalyst, not as Mo catalysts, which were dependent on the sulfides. Mellor et al. [49], seeking to find a sulfur-tolerant catalyst (in lieu of sulfur-dependent molybdenum [57]), expanded on Copperthwaite's review. In addition to the cobalt chromate spinel, Co-MnO catalysts were also tested. They were found to be sulfur tolerant up to 220 ppm H_2S. The catalyst deactivated in higher levels of sulfur because Co sulfided to Co_9S_8. Conversion was very good at 400 °C (X~0.93), and near equilibrium conversions were reached at 550 °C. Some CH_4 formation was prevalent as well. The S/G ratio was 4.5 for their experiment. Hutchings et al. [58] evaluated the ratio of Co:Cr for the most effective activity. They concluded that 3:1 ratio was the best suited for greatest activity. Reaction was tested at 400 °C. Once again, at

concentration levels of 240 ppm H_2S, the catalyst deactivated. Laniecki and Zmierczack [59] worked with ratios of Mo and Co. They concluded that higher levels of cobalt led to greater selectivity to methanation. This is not surprising, because cobalt has been the subject of research for the propagation of liquid hydrocarbons from syngas [34, 60-62].

Recent research has not been able to fill the gap of providing adequate sulfur-tolerant catalysts capable of catalyzing the WGS over a range of sulfur concentrations typical of biomass streams. Though some catalysts have proven to be sulfur tolerant in lower concentrations of H_2S, they have been demonstrated at higher temperatures. A sulfur-tolerant catalyst at lower temperatures will make the process more viable in terms of energy requirements and in thermodynamics.

Schaidle et al. [63] added Mo to a carbide. These Mo_2C catalysts deactivated in less than 10 ppm H_2S. Pt loading did not perform much better; however, it did allow some regeneration of the catalysts. Sulfur concentrations had to be reduced to sub ppb levels to regain normal activity. Laniecki and Ignacik [64] reviewed the support with a fluorite structured titania and zirconia support. High sulfur concentration (2% volume) was needed to maintain activity. The

support increased the dispersion of the catalyst. Valsamakis and Stephanopoulous [65] reported a novel sulfur-tolerant catalyst for high temperature applications. They used lanthanide-oxysulfide catalysts, and tested up to concentration levels of 700 ppm H_2S. About 70% CO conversion was maintained throughout a broad temperature range. S/G ratio was 5 for experiments. Ladebeck and Wagner [32] showed that greater CO conversions are required by thermodynamics with increasing S/G ratios. The high temperatures used do not favor the WGS, but rather the reverse WGS.

Other sulfur-tolerant materials being researched are noble metal and metal assisted ceria based catalysts. Xue et al. [66] researched Pt/ZrO_2 catalyst in 50 ppm H_2S. They observed that Pt could remain active, but still lost activity. Regeneration of the catalyst was possible by eliminating sulfur from the feed.

Due to its ability to conduct oxygen in any environment [67-70], ceria came to prominence for the 3-way catalyst for the catalytic converter currently found in every automobile. Various metal-doped ceria has been extensively reviewed in literature. Tabakova et al. [71] studied the WGS over Au/CeO_2 catalysts. The ceria was able to catalyze the reaction of lower temperatures, which favors the thermodynamics.

The catalyst was highly stable due to the oxygen vacancies on the ceria support near the gold clusters. Li et al. [72] also reported increased activity with the addition of Ni and Cu to the support of ceria at lower temperatures. Bunleusin et al. [67] reported that ceria is an excellent support, regardless of the other catalytic metal it is supporting. The CO that adsorbs from the bulk flow to the supported metal is oxidized by ceria. The ceria is then re-oxidized by steam from the bulk flow. The calcination temperature and crystallinity of the ceria affect how its oxygen conducting properties are utilized. These results were confirmed by Jacobs et al. [73]. In the presence of sulfur, ceria has a mixed record in literature. Reddy, Boolchand, and Smirniotis report [74] that Fe/Ce based mixed metal spinels ($Fe_{1.6}Ce_{0.2}M_{0.2}O_4$: M = Cr, Co, Zr, Hf, and Mo) were sulfur tolerant in 400 ppm H_2S. Testing in a sulfur-free feed and 400 ppm, H_2S feed produced similar results at temperatures above 400 °C. S/G ratios used in this experiment were 3.5 and 1.5. The Fe/Ce base spinel fared best over the temperature range of 500 °C to 560 °C. At 560 °C, all the metals yielded similar conversions (89%). Reddy et al. also noted the stabilizing effect ceria had on Fe. X-Ray Diffraction and XPS studies confirmed no bulk sulfidation of catalyst surface. Liu et al. [47] tested a Pt/CeO_2 catalyst in a low concentration of sulfur (20 ppm). They observed 73% conversion in long term testing at 500 °C.

The Pt loading had an effect on the methanation of the reaction; the lower the loading (optimum 0.38 wt %), the lower the selectivity to methane. However, in sulfided streams, hydrogen was the favored product, selectivity to methane diminished.

CHAPTER III: MOTIVATION

Need for Sulfur-Tolerant Catalyst

The principal motivation for this work is to present a novel sulfur-tolerant WGS catalyst with robust capabilities to operate in the temperature range of 350 °C to 450 °C. Given the recent interest in biomass as a feedstock for gasification, sulfur levels for biomass derived synthesis gas range from 50-600 ppm [42]. Currently, no one catalyst has facilitated activity over that range, and Mo based catalysts are sulfur dependent, and need concentrations greater than 300 ppm to remain active [33]. Co-Cr spinels were able to maintain activity in lower concentrations of sulfur, but they deactivated in concentrations higher than 240 ppm. Higher ratios of cobalt also had selectivity to methane [48-49]. Reddy's recent success with ceria and iron offers insight into using mixed spinels to achieve sulfur tolerance [74]. These spinels are limited to HTS testing though, and an active catalyst which can function at lower temperatures may make the catalyst more economically viable. In order to fill the gap, concentrations of sulfur beyond 400 ppm H_2S are necessary to enhance the data on these catalysts.

Importance of Spinel

The mixed spinel with ceria is an attractive option for catalysts because one can exploit ceria oxygen storage/ conduction properties while maintaining magnetic and redox capabilities of a spinel. The literature on spinels shows that their structure can enhance WGS activity with the same metals in the LTS [75]. Typical HTS catalysts already use a spinel structure. In the support phase in WGS, the spinel structure was shown to enhance CO conversion for Co-Mo oxides [55, 76]. Jacobs et al. [77] reported that the structure of spinels exhibits oxidative transfer where the metallic cations can migrate. They used a spinel for successful reduction of nitrobenzene, when other structures were incapable of catalyzing the reaction. Some attention has also been given to the ability of Cu-Co and Mn-Co spinels for CO oxidation [78]. Traditional Mn-Al spinels have also been tested as supports for various metals in the catalytic process [76]. Given findings in industry and literature, pH Matter LLC, a small business based in Columbus, Ohio, is seeking to introduce sulfur-tolerant WGS catalysts to the biofuels market. Materials for this project will include Mo, due to its high activity in sulfided streams [33].

Importance of Cobalt

Cobalt will also be used, since it is an ingredient in desulfurization processes [33]. In addition to sulfided streams, cobalt has also been investigated for the WGS [79]; it has also been reported to have greater activity than HTS ferrochrome catalysts [80]. It has also been proven that cobalt increases the number of active sites for the Co-Mo hydrodesulfurization/SGS catalysts [81]. Grenoble et al. [82] showed via a volcano plot of ΔH_{ads} of CO that second to Cu, Co featured prominently as a catalyst which would work well for the adsorption of CO.

Importance of Ceria

Cerium will also be used due to its widely known oxygen storage capacities [69-70, 83] when coupled with O_2. Given its recent rise in WGS literature, ceria (CeO_2) has been labeled a great WGS catalyst [84]. As previously discussed, metal loading of ceria increased WGS at both high and low temperatures [72, 84-86]. It also facilitates CO oxidation on the catalyst surface, thereby reducing selectivity to the undesired methanation reaction [87]. This is important, considering cobalt will also be used as a sulfur-tolerant material. Cobalt is well known to have selectivity to methanation [88]. This versatility makes cerium an ideal material to incorporate inside a spinel catalyst.

Importance of Iron

Iron will also be used in the construction of the catalyst. The rationale behind this is its long held history in HTS catalysis. Reddy's recent success [74] of incorporating it into a spinel with ceria was interesting to note as well.

Other structure forms like fluorites and direct ratios are being tested by research partners, but will not be reported in this work. Some perovskites have been shown to have a strong promoting effect of converting H_2S to CH_4 in syngas streams [89]. However, the initial WGS activity for perovskite samples tested by research partners has been too low to warrant further testing.

Given some disagreement in the field of sulfur tolerance, there remains a need for novel catalysts to be tailored for a range of sulfur contents [54].

Legislative Considerations

Because sulfur is an impediment to hydrogen conversion, novel, robust catalysts are needed to remain active in various levels of sulfur. To meet the DOE's alternative energy goals, impurity-tolerant WGS catalysts figure to be an integral part [90]. To comply with the USAF's

goal to provide synthetic fuel for half its domestic fleet [6], the need to run efficient processes from biomass sources is a must. The WGS is an integral part to tweaking the H_2/CO ratio for GTL processes. If the sulfur-tolerant WGS catalysts are not proven, gasifier effluent streams must be cooled down to remove sulfur [91], or methane must be reformed to increase hydrogen content for this process. Both processes add extra steps and increase the energy demand on the process.

CHAPTER IV: OBJECTIVE

Group Project Description

The intent of this project is to identify promising sulfur-tolerant WGS catalysts composed primarily of Fe, Co, Ce, and Mo. Other materials used in synthesis include Cr, Sr, Ti, and Mn for baseline testing. The targeted market for this project is GTL plants with biomass-derived synthesis gas. The spinel structure will feature prominently in catalyst synthesis, but other structures will also be tested. This project is in collaboration with pH Matter LLC. This project was also partially funded by NSF Solicitation # 09-609, *Mixed Oxide Sulfur-Tolerant Water Gas Shift Catalysts*. Catalyst synthesis and reaction testing take place in pH Matter laboratories. Catalyst characterization, reaction, and sulfidation studies take place in University of South Florida laboratories. pH Matter has synthesized many samples for testing. Table 6 is a fraction of the total sample matrix synthesized by pH Matter for catalytic testing (29 of 76 total catalysts are shown. Catalyst synthesis and testing are currently under proprietary restrictions).

Table 6: pH Matter sample matrix.

Catalyst	Prep method	Calcination T (°C)
Co_3O_4	Chemical/peroxo	700
CeO_2	Chemical/peroxo	700
$CeCo_2O_4$	Pechini	400
$CeCo_2O_4$	Pechini	700
$MnCo_2O_4$	Pechini	700
$Ce_{0.5}Ti_{0.5}Co_2O_4$	Pechini	700
$Ce_{0.3}Ti_{0.3}Mo_{0.4}Co_2O_4$	Pechini	400
$CeFe_2O_4$	Pechini	700
$Ce_{0.9}Mo_{0.1}Co_2O_4$	Pechini	700
$CeCoFeO_x$	Pechini	700
$Ce_{0.75}Co_{0.25}O_2$	Pechini	700
$Ce_{0.5}Co_{0.5}O_2$	Pechini	700
$Ce_{0.75}Co_{0.22}Fe_{0.03}O_2$	Pechini	700
$CeCoFeO_x$	Pechini	450
$CeCo_2O_4$ 10 wt% MoO_3	Pechini /Mo ICW	450
$Ce_{0.75}Co_{0.25}O_2$/0.06 Fe	Pechini/Fe ICW	450
$Ce_{0.75}Co_{0.25}O_2$/0.125 Fe/5% MoO_3	Pechini/Fe Icw/Mo ICW	450
$Ce_{0.75}Co_{0.25}O_2$/0.125 Fe/1% MoO_3	Pechini/Fe Icw/Mo ICW	450
$Ce_{0.75}Co_{0.25}O_2$/0.125Fe	Biomorphic	450
Co:Cr 3:1	Pechini	500
Co:Cr 1:2	Pechini	500
Fe 90/Cr 10 Commerical composition	Fe 90/Cr 10 Pechini	500
$Co_{2.5}Ce_{0.25}Cr_{0.25}O_4$	Pechini	500
$Fe_{2.5}Ce_{0.25}Co_{0.25}O_4$	Pechini	500
$Fe_{2.5}Ce_{0.25}Co_{0.25}O_4$	Pechini	500-N2
$Fe_{2.5}Ce_{0.25}Cr_{0.25}O_4$	Chemical Precipitation	500-N2
$Co_{2.5}Ce_{0.25}Cr_{0.25}O_4$	Pechini	500-N2
$Co_{1.25}Fe_{1.25}Ce_{0.5}O_4$	Pechini	500-N2

Samples discussed in detail in this thesis are highlighted in yellow. SSR = solid state reaction. ICW = incipient wetness method.

Description of Thesis

The intent of this thesis is to report on the reaction behavior of sulfided and unsulfided Ce-Co based catalysts with varying amounts of Mo and Fe for WGS catalysis. These catalysts were characterized via Temperature Programmed Reduction, N_2 physisorption, and X-Ray Diffraction. The WGS reaction was performed over the catalysts. Of the catalysts listed, only four will be reported in this work. The motivation for choosing these four was to compare the differences in:

- a base spinel $CeCo_2O_4$,
- the same base spinel with Mo added to surface, $CeCo_2O_4$, supported by 10% Mo,
- a spinel with the same ingredients, but with Mo incorporated into the spinel matrix, $Ce_{0.9}Mo_{0.1}Co_2O_4$, and
- a mixed spinel with iron, $Fe_{2.5}Ce_{0.25}Co_{0.25}O_4$.

This sample was chosen to investigate the incorporation of Ce, a metal with higher WGS activity than Fe, and Co, a sulfur-tolerant material, into a traditional magnetite HTS catalyst. It is desired to see the effect Mo has on the $CeCo_2O_4$ under sulfided and unsulfided WGS conditions. It is also desired to measure the activity and sulfur tolerance of a Fe based catalyst containing Co and Ce. Only initial activity was tested. Long term activity testing will not be reported in this thesis.

CHAPTER V: EXPERIMENTAL

Synthesis Method

The four selected catalysts were synthesized via Pechini's method at pH Matter in Columbus, Ohio. The Pechini method [92] was patented in 1967 as a means of using acids to chelate metal ions into stable complexes. This acid solution was subsequently used as a solvent for metallic salts. The solution then becomes gel-like, enhancing the surface area of the material. Finally a powder can be recovered. The method allows metallic ingredients to be mixed in at a molecular level. This gives flexibility into building a desired structure, and adding a desired amount of components into that structure. For the interested reader, Chapter 3 in The Handbook of Sol-Gel Science and Technology: Processing Characterization and Applications, provides a detailed description of the process [93].

Reactor Procedures

Reactor

A PerkinElmer model # 0993-8559 Gas Chromatograph (GC) was used in this experiment. The apparatus is shown in Figure 6.

Figure 6: PerkinElmer gas chromatograph. Apparatus includes water bubbler, thiophene bubbler, flow meters, temperature controlled furnace, and DELL computer.

All samples were carefully weighed prior to loading them into a glass U-tube reactor. All catalyst samples were carefully weighed to 1.00 x 10^{-1} g, and were held in-between two slugs of quartz wool. They were loaded into a temperature controlled furnace. Heat tape at 100 °C lined all pipelines between instrumentation. Flow meters with varying maximum capacities (i.e. 50 -100 cm^3/min) were set up to control reactor inlet conditions.

Pretreatment

After sample loading, He flow was increased to 45 cm^3/min; H_2 was introduced at 5 cm^3/min to efficiently activate (reduce) the sample prior to introducing reactants. Reduction of spinels as pretreatment increased their catalytic activity [62]. Under these conditions, the

temperature was then ramped up to 400 °C, at 10 °C/min. The temperature was maintained at 400 °C for an hour. After one hour, the He carrier flow was set to 50 cm^3/min (in two cases returned to 5 cm^3/min), and the H_2 flow was shut off. The He stream was allowed to flow for a few minutes in order to purge any residual H_2 from the system.

Flow Rates of Reactants

Though higher steam/gas (S/G) ratios are typically used in WGS reactions, the apparatus for this project was set up for an S/G ratio of 1. A bubbler, shown in Figure 7, was used to provide steam for the WGS reaction.

Figure 7: Water bubbler from which helium gas becomes saturated.

From thermodynamic relations taken from literature values [94], A T vs. vapor pressure plot (see Figure 8) was calculated.

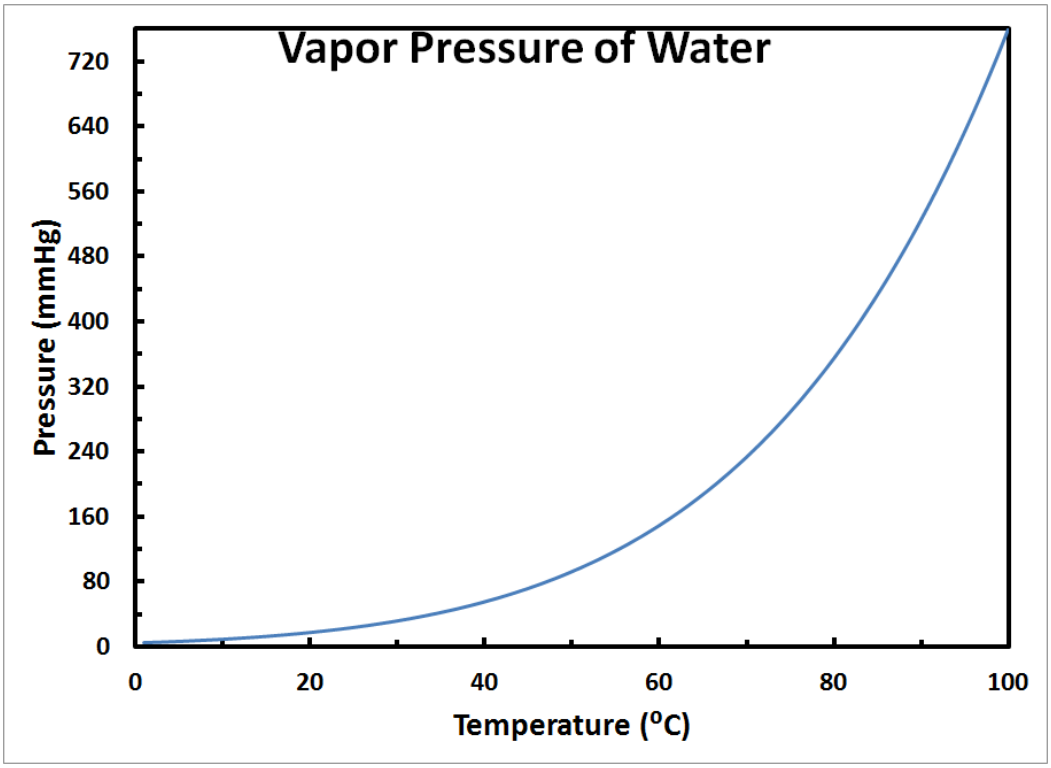

Figure 8: VLE data for water. Constants provided from Perry's Chemical Engineering Handbook [94].

From this plot, using ambient temperature (25 °C) and atmospheric pressure (1 atm), a vapor pressure of 23.68 mmHg was obtained. It was assumed that temperature was constant; therefore the composition of water vapor was constant. Since atmospheric pressure was the only pressure exerted on the water bubbler, it can be assumed that the vapor pressure of water divided by total pressure yields a fraction (χ_w) indicative of the amount of water vapor in the system.

$$\chi_w = \frac{P_{H2O}^{sat}}{P_{total}} = \frac{23.68}{760} = 0.03116 \quad (7)$$

Since helium gas bubbled through water, it was assumed that the flow of H_2O (F_{H2O}) vapor is equal to $\chi_w F_{He}$, where F_{He} is the flow of helium in cm^3/min. A table correlating the flow of helium to the flow of water is shown in Table 7. Since $F_{He, max}$= 50 cm^3/min, the max flow rate of water (F_{H2O}) is 1.56.

Table 7: Values of F_{H2O} as a function of F_{He}.

F_{He}	F_{H2O}
5	0.156
10	0.312
15	0.467
20	0.623
25	0.779
30	0.935
35	1.091
40	1.246
45	1.402
50	1.558

The flow rate of CO (F_{CO}) was set at 1.6 cm^3/min to obtain a steam to gas ratio (S/G) of approximately 1. It should also be noted that molar flow rates were based under the assumption of ideal gases and calculated at STP.

Gas Hourly Space Velocity

The Gas Hourly Space Velocity (GHSV) is a ratio of volume of the feed gas at STP/hr per volume of the catalyst. The volumes cancel each other out and the units of the GHSV are per hour. The volume of the catalyst for this experiment was calculated by measuring the diameter of the U-tube (0.25 cm) ^{2} x the approximate length of the catalyst powder in the tube (0.5 cm) x $\pi/4$. The rough answer for this is 0.098125 cm^3. Two inlet flows were used for this experiment: 58.2 cm^3/min and the rest 103.2 cm^3/min. Converting the minutes into hours, the resulting approximate GHSVs used in this experiment were 35587 hr^{-1} and 63103 hr^{-1}, respectively. It should be noted that these GHSV are approximate. It was originally intended to maintain a GHSV in the vicinity of 30,000 hr^{-1}, per pH Matter specifications. However, all the results tabulated in this thesis save two were calculated at a GHSV of approximately 63103.

Addition of Sulfur

In order to study the effect of H_2S adsorbed on the catalyst surface, liquid thiophene (C_4H_4S) at 99.6% purity was used. Thiophene is a sulfur-containing species prevalent in crude and it is commonly desulfurized catalytically [95-96]. Pure helium was flown through a bubbler (see Figure 3) to introduce C_4H_4S to the system. Excess

hydrogen (F_{H2}) was flown into the reactor at 50 cm^3/min. The following reaction is assumed to produce H_2S [97]:

$$C_4H_4S + 3H_2 \rightarrow H_2S + C_4H_8 \qquad \Delta H = -1.37 \times 10^{-12} \frac{kJ}{mol} \qquad (8)$$

Though there are various isomers of C_4H_8, reaction data was calculated from 1-Butene [94]. The disassociation reaction was assumed to proceed over the catalyst via Brønsted–Evans–Polanyi kinetics over the catalyst [98]. Due to the low heat of reaction, the equilibrium constant K has little dependence on temperature, therefore, equilibrium conversion is simply a function of the volumetric flow rate. For the flow rates used in this experiment, equilibrium conversions > 0.98 were calculated. A complete overview of the thermodynamic calculations is offered in Appendix II.

Similar to the calculations of F_{H2O}, VLE relationships were used to derive a vapor pressure vs. temperature plot for C_4H_4S. Equation parameters were taken from Perry's Chemical Engineering Handbook [94], and are graphed in Figure 9.

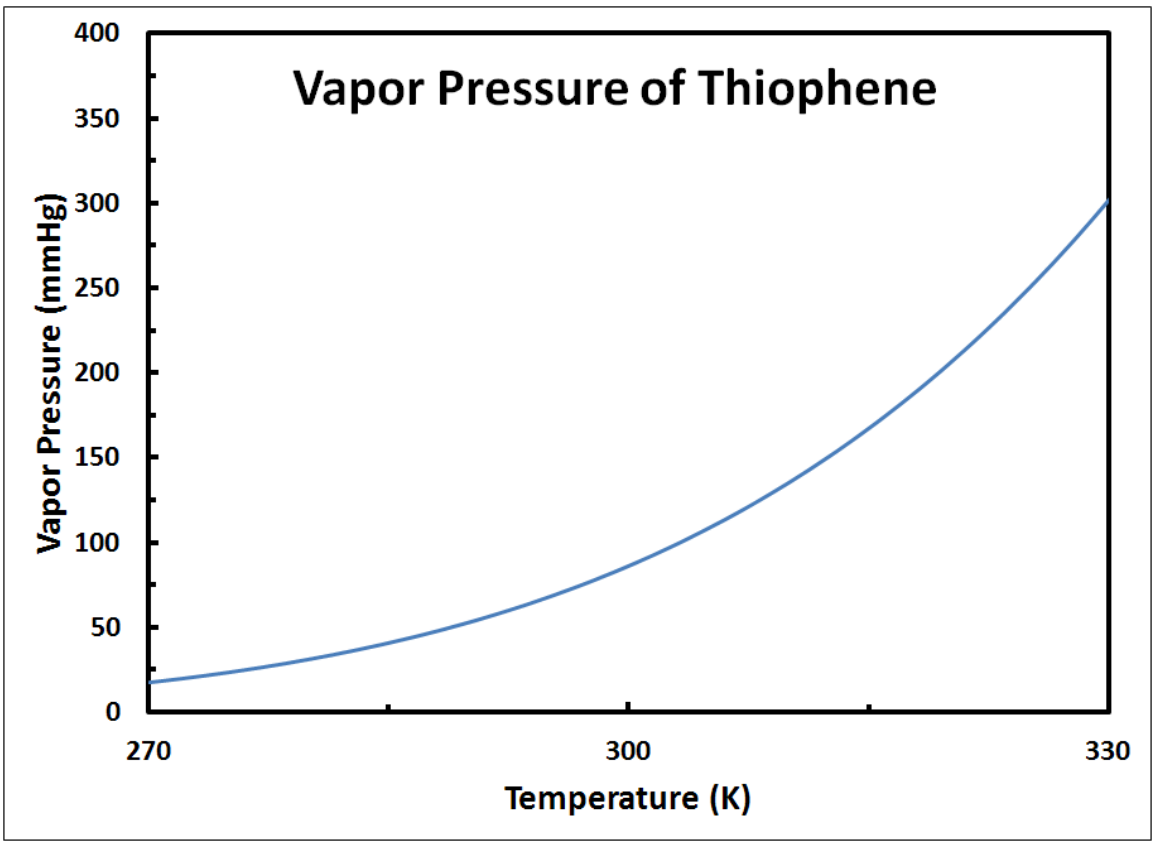

Figure 9: VLE data for thiophene. Antoine constants taken from Perry's Chemical Engineering Handbook [94].

A problem arose with using ambient temperature for thiophene. The vapor pressure was 80 mmHg, which was too high to produce the desired lower concentrations as a function of helium flow. Therefore an ice bath was used to cool the liquid thiophene down to temperatures ranging from 1 - 2 °C. This lower temperature lessened the vapor pressure to approximately 25 mmHg. Figure 10 shows the cooled thiophene in an ice bath.

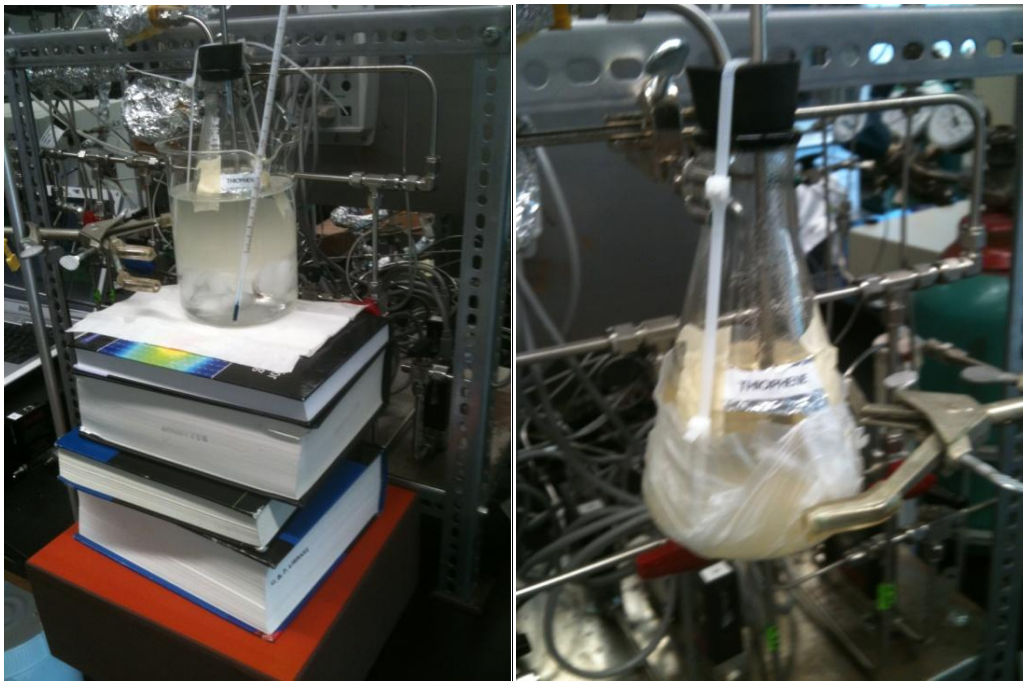

Figure 10: Thiophene bubbler, with and without ice bath. Pure helium inlet bubbles through liquid thiophene.

After cooling the stream down, viscosity issues with the liquid thiophene arose. The flow rate of He was insufficient to bubble through the viscous thiophene. Due to these issues, the ice bath was abandoned, and ambient temperatures and pressures were used.

Utilizing the same assumptions for the water calculations, the fraction (χ_{Th}) can be computed as follows:

$$\chi_{Th} = \frac{P_{C4H4S}^{sat}}{P_{total}} = \frac{80}{760} = 0.10526 \quad (9)$$

The flow of C_4H_4S (F_{Th}), is a function of the flow of the inert, F_{He}, as helium was bubbled through. The values are listed below in Table 8. These flow rates correspond with a concentration of reacted H_2S from thiophene.

Table 8: Flow rate of thiophene.

F_{He} (ccm)	F_{Th} (ccm)	ppm H_2S
1	4.70E-06	523
1.1	5.17E-06	575
1.2	5.64E-06	627
1.3	6.11E-06	679
1.4	6.57E-06	731
1.5	7.04E-06	783
1.6	7.51E-06	835
1.7	7.98E-06	887
1.8	8.45E-06	938
1.9	8.92E-06	990
2	9.39E-06	1040
2.1	9.86E-06	1090
2.2	1.03E-05	1140
2.3	1.08E-05	1200
2.4	1.13E-05	1250
2.5	1.17E-05	1300
2.6	1.22E-05	1350
2.7	1.27E-05	1400
2.8	1.31E-05	1450
2.9	1.36E-05	1500

Thiophene in WGS feed as a function of helium bubbled through liquid thiophene. P*=80 mmHg and F_{inert}=200 cm^3/min

Concentration of H_2S

In research, it is common to represent trace amounts of a substance in units of ppm. Sulfur concentrations for these experiments were based

on ppmv, or parts per million based on the volumetric flow rate. Since ppm is a part/whole, or a ratio, a table has been crafted as a function of F_{He} to indicate the appropriate range of flow. A linear relationship was developed to acquire the desired flow rate for a certain ratio of contaminant to total flow. A sample calculation for ratio is shown here.

$$ratio = \frac{F_{Th}}{F_{Th}+F_{H2}+F_{He.carrier}+F_{He,inert}} \quad (10)$$

where $F_{He,\ carrier}$ is the flow rate of helium through the bubbler, and $F_{He,\ inert}$ is the constant flow rate of helium.

For this experiment $F_{He,\ inert}$ has a constant value of 150 cm^3/min. As previously indicated, F_{H2} also has a constant value of 50 cm^3/min. This flow rate was run in excess than what is stoichiometrically required for this reaction in order to assure conversion to H_2S. To further solve for ppm, the ratio is simply multiplied by 1,000,000. This plot is shown in Figure 12.

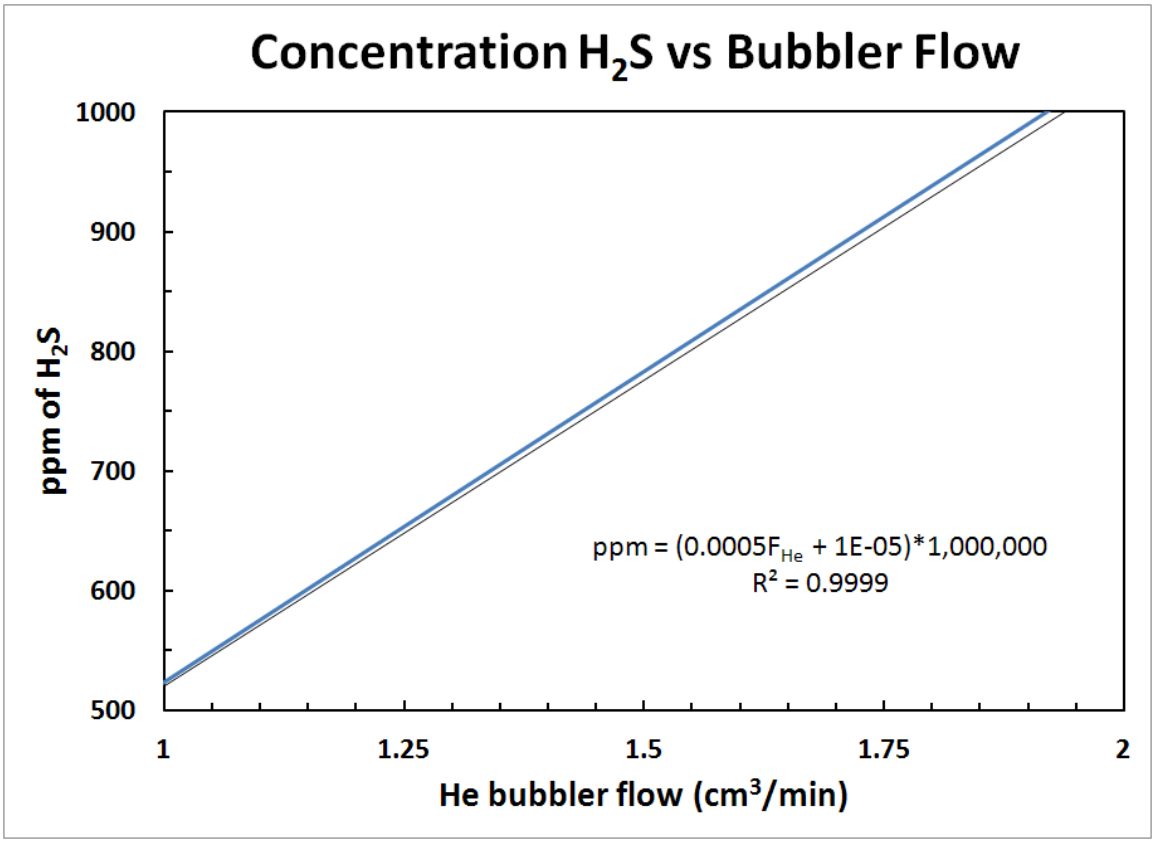

Figure 11: Concentration of H_2S. This plot shows the linear relationship between concentration of H_2S and helium bubbler flow without ice bath. Vapor pressure equals 80 mmHg. Flow of inert equals 150 cm^3/min.

Desired ratios, such as 500 ppm and 800 ppm, can be easily plugged into the algebraic equation to solve the corresponding flow of inert (see Figure 12). It should be noted that 1 cm^3/min is the minimum flow allowed by the flow controller, and that inert flow rates were already set at maximum mass flow controller capacity. Future modifications to the apparatus are necessary to further reduce the concentration.

Options for Sulfur Flow

Due to certain issues in studying desired concentrations of sulfur, greater flows of inert are needed to reduce sulfur concentration. By manipulating the current apparatus, both 50 cm^3/min and 100 cm^3/min are available. The following charts indicate the amount concentration with 150 cm^3/min and 200 cm^3/min of inert in the initial feed. Four charts will be presented and shown in Figure 13, showing possible improvements to process. Even with these higher flow rates, to study sub 300 ppm levels of H_2S, inert flow rates will need to exceed 300 cm^3/min.

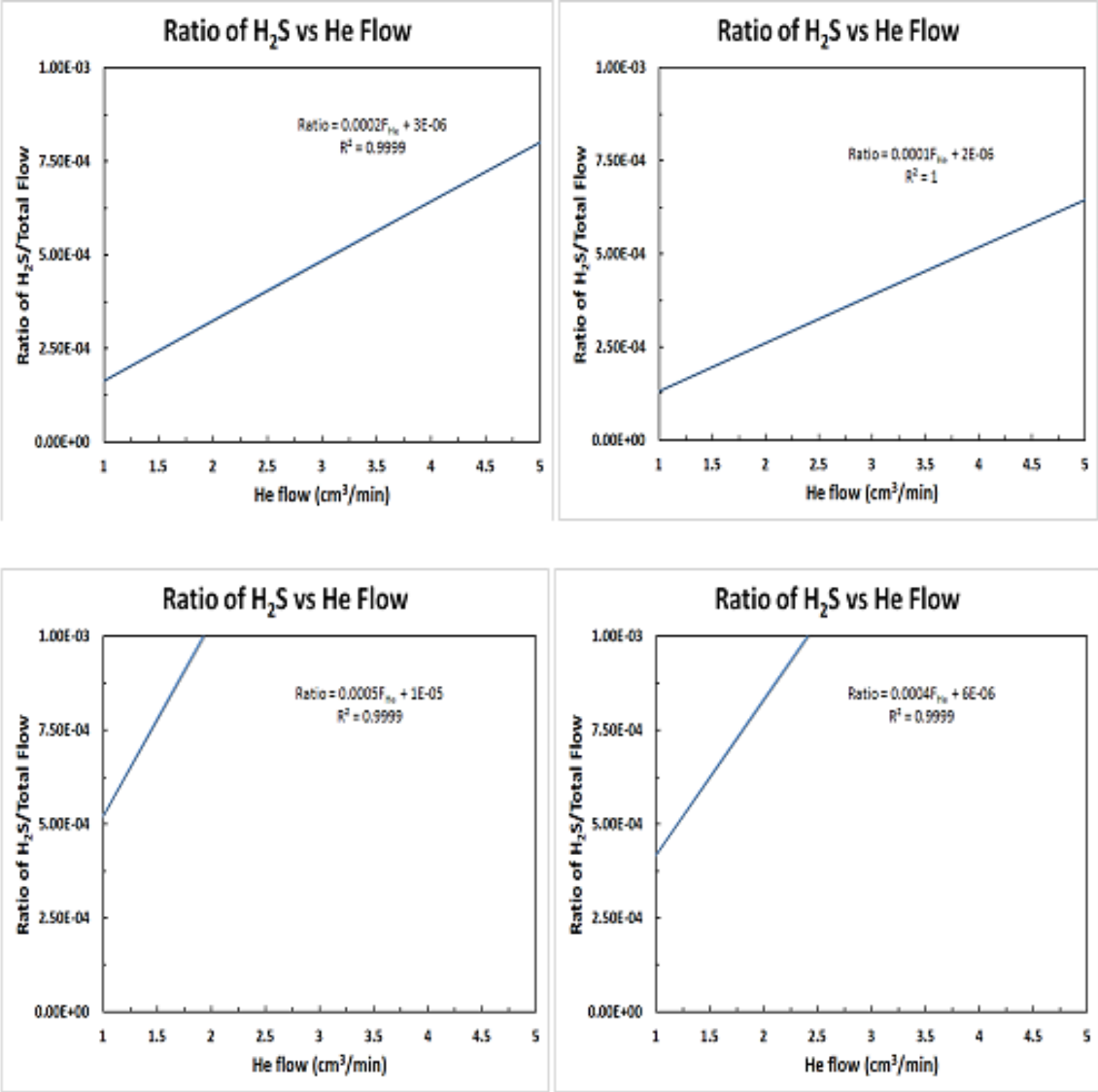

Figure 12: Possible apparatus improvements with current optimum settings. Left column indicates 150 cm^3/min and 200 cm^3/min in the right column. The top row includes flow of inert through thiophene in an ice bath (P*=25 mmHg), while the bottom row is flow of inert through thiophene at ambient conditions (P*=80 mmHg). Ratio multiplied by 1,000,000 yields concentrations in ppm.

Careful observation of these charts leads to the conclusion that studying concentrations of sulfur lower than 300 ppm is not possible.

The best case scenario allows for studying 390 ppm as a base case. If lower concentrations are desired for future testing, larger flow rates of inerts are needed. This work will include two sulfur concentrations: 500 ppm and 800 ppm.

Measurement of Catalytic Activity for Sulfur-Free Feeds

After pretreatment, reactant flow was set to bypass the reactor to obtain proper baseline readings. At least 4 to 5 injections were done with a baseline sample as to decrease error. After stability was identified, the reactants were then fed through the reactor at an initial temperature of 400 °C. An injection was performed almost immediately to measure the reaction rate of the fresh catalyst. Subsequent injections followed to assess the stability of the catalyst. After stability was assured, the effect of temperature on the activity was measured between 300 and 400 °C.

Measurement of Catalytic Activity after Sulfidation

Prior to sulfiding catalyst samples, WGS activity was tested on the selected catalysts. After activity was measured with unsulfided catalysts, the catalysts were sulfided for 30 minutes. After sulfidation, a He purge stream flowed at 100 cm^3/min flow for at least 30 minutes to mitigate exposure to the GC. The procedure commenced as

previously described. Baseline injections were performed by bypassing the reactants from the reactor, then the WGS reaction was tested over the sulfided catalyst at 3 different temperatures, activity permitting.

Performing Injections

An injection was performed by feeding reactor effluent into the column for exactly 0.2 minutes. Each injection was subsequently separated by a GC column. The duration of a GC injection was 3 minutes. The amount of gas separated by the column was then plotted as a peak with an intensity as a function of time. Area under the peak was given by a TCD signal coming from the separation column.

Peak Position

Prior to performing the WGS, the GC column was tested independently with solely one of the relevant gases accompanying the carrier He feed. The following peak positions were observed and assigned to the gaseous species as a function of time (see Table 9).

Table 9: Gas chromatogram peak position.

Position (time)	**1.04**	**1.1**	**1.25**	**1.5**	**1.95**
Specie	H_2	CO	CO_2	CH_4	H_2O

Sample chromatograms are included in Appendix III.

GC Calibration

A PerkinElmer model # 0993-8559 Gas Chromatograph (GC) was used to analyze reactor effluent. Under reaction conditions previously described, the GC peak area was calibrated to flow rates of CO and CO_2. Average peak area was calculated and attributed to a known flow rate. Two flow rates were used for the calibration 1.0 and 1.6 cm^3/min, respectively. The calibration was forced through 0 to provide an additional data point. 100 cm^3/min of inert He was the carrier for the calibration. Plots are shown in Figure 13.

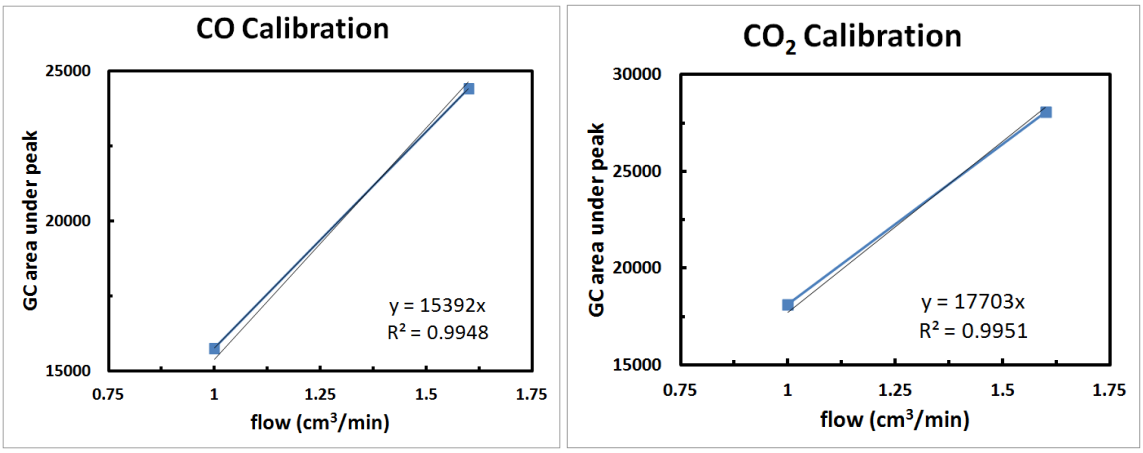

Figure 13: GC calibration curves for CO and CO_2 flows.

From these plots, volumetric flow rate were tabulated by plugging peak area into the equations shown on Figure 13 and solving for x algebraically. Once the volumetric flow rate was obtained, a molar flow rate could also be formulated with ease. The Ideal Gas Law was used to calculate molar flow. Atmospheric pressure was used; a pressure gauge was used during the experiment. The temperature value assigned to all flow was 100 °C, which is believed to be the temperature of the detector. Though the reactor itself varied temperature, the temperature of the detector remained constant. Molar steam flow, however, was calculated at standard temperature and pressure (STP). CH_4 and H_2 calibration curves were also calculated and their constants were used for molar flow calculations as well (note: only CO and CO_2 graphs are shown in Figure 13).

Measurement of CO Conversion

The inlet feed of CO was a fixed value at 1.6 cm^3/min. This flow was always calibrated via the observed calibration constants. Upon conversion to mol/min (a typical value is 6.75 x 10^{-5} mol/min) the inlet molar flow for CO was calculated. Because He was the carrier gas, the housekeeping for the reaction was done in terms of carbon. CO conversion was calculated via the following equation:

$$X = \frac{F_{CO,0} - F_{CO}}{F_{CO,0}} \quad (11)$$

where $F_{CO,0}$ is the inlet CO flow in mol/min, and

F_{CO} is the amount of unconsumed CO detected by the GC TCD.

Generation of CO_2 was also calculated via the following equation.

$$X_{CO2} = \frac{F_{CO2}}{F_{CO,0}} \quad (12)$$

Unfortunately, the CO_2 generated did not equal CO consumed. One explanation the mass balance could not be closed is that some coking was expected due to slightly more CO in the feed than steam. Another explanation is the validity of the ideal gas assumption at a higher GHSV, since pressure and temperature inside the reactor could not be directly measured. Selectivity calculations for methane were calculated by dividing the molar output of CH_4/CO_2. Sample spreadsheet calculations for samples are shown in Appendix IV.

Characterization

Surface Area

All samples underwent surface area calculations via the BET method [99] on a Quantachrome Autosorb iQ automated gas sorption analyzer. The instrument is pictured in Figure 14.

Figure 14: Quantachrome Autosorb iQ automated gas sorption analyzer. Analysis port is covered by blue screen. Outgassing ports are shown on right.

The BET equation is the most widely used method of surface area calculations:

$$\frac{1}{W\left(\frac{P_0}{P}-1\right)} = \frac{1}{W_m C} + \frac{C-1}{W_m C}\ \frac{P}{P_0} \tag{13}$$

where:

P= Pressure in mmHg,

P_0= Initial Pressure in mmHg,

P/P_0 = Relative Pressure,

W= weight of gas adsorbed at a relative pressure in grams,

W_m= weight of adsorbate monolayer in grams, and

C= BET constant.

The BET constant is related to the energy of adsorption of the monolayer. Surface area can be subsequently calculated from the plot of $\frac{1}{W\frac{P_0}{P}-1}$ vs. $\frac{P_0}{P}$. The slope of the plot is given as:

$$m = \frac{C-1}{W_m C} \tag{14}$$

and the y-intercept is given as:

$$b = \frac{1}{W_m C} \tag{15}$$

Combining equations 14 and 15, the weight of the adsorbate monolayer is given:

$$W_m = \frac{1}{m+b} \tag{16}$$

Since the properties of the adsorbate are known, molecular geometry is all that is needed to cap off the calculation.

$$SA = \frac{W_m A_{cs} N}{MW} \tag{17}$$

where:

SA= surface area of sample in m^2,

MW= Molecular weight of adsorbate,

A_{cs} = molecular cross sectional area of adsorbate, and

N = Avogadro's number (6.0221415×10^{23} molecules/mol).

The surface area can further be normalized by dividing it by the weight of the sample.

Nitrogen was used as the analyzing gas. In order to assure a clean sample surface, samples had to be outgassed prior to Multipoint BET analysis. Outgassing consists of removing the pressure from a sample tube while soaking it with heat. This treatment purified the sample, removing any gas from the sample, and ensuring the entire surface was available for physisorption from the adsorbate. The heaters on the automated gas sorption analyzer did not exceed temperatures of 400 °C. Best practice required soaking temperatures roughly half the boiling point of the sample. Because ceria has a high boiling point, every sample was soaked for 2 hours at a maximum temperature of 400 °C. Any atmospheric gases adsorbed to the sample were vacuumed off. Prior to analysis, all samples were carefully reweighed without contamination of atmospheric gases.

BET calculations were performed computationally by the instrument software. Though a full relevant pressure range was measured for

most samples (P/P_0 =0.01 … 0.99), the linear portion of the plot was used for surface area determinations. All BET surface areas were calculated from a relative pressure range of 0.1 to 0.4 from desorption isotherms (-196 °C). Sample holders of 6mm, 9mm diameters were used to hold samples.

Temperature-Programmed Reduction

Temperature Programmed Reduction (TPR) is a useful method in determining at what temperature range a sample will reduce (donate its electrons) a gaseous reducing agent flowing over at constant velocity. A mixture of 5% H_2 and an inert gas (N_2) flows over a sample placed in a temperature programmed furnace. A mass spectrometer or a thermal conductivity detector (TCD) measures the charge associated with the respect to H_2. At a certain temperature, the energy level is sufficient to break the metal-oxide bond. The disassembly of oxide samples produces H_2O. Reduction temperatures consistent with reaction temperatures of interest are usually desired. The TPR for this project was carried out on a Cirrus mass spectrometer and the Quantachrome iQ gas sorption meter. The Cirrus mass spectrometer is pictured below in Figure 15. The Quantachrome instrument is pictured in Figure 16.

Figure 15: Mass spectrometer. (1) Entire apparatus in Kuhn Lab at USF. This includes a furnace with sample holder, gas flow meters, and mass spectrometer. (2) Cirrus mass spectrometer. (3) USF project collaborator with apparatus. (4) A sample tube in preparation for loading to furnace.

Figure 16: Quantachrome iQ TPR set up.

Approximately 0.3 grams of powder sample were loaded into the quartz reactor. The sample was held in between two slugs of quartz wool. Inert helium was flown over the sample while the sample was heated to 110 °C at 10 degrees/minute. This was to 'degas' the powder from any contaminates that may be adsorbed to surface. After being held for 30 minutes, the sample was then cooled to 50 °C. The gas was changed to 10% H_2 and balance inert (He or N_2). Flow rates were 5 sccm H_2, and 45 sccm inert. After a short purging period, the

temperature was ramped up to 800 °C at degrees/minute and held there for 30 minutes. The Quantachrome iQ software macro is shown in Table 10. Reactor effluent was then analyzed via a mass spectrometer or a Thermal conductivity detector (TCD). A signal relating the amount of H_2 consumed or a mass/charge ratio (water formed by m/z = 18) was recorded. From this signal, optimum reduction and operating temperatures can be inferred. The catalyst's reduction tendencies and amount of H_2O formed can also be calculated and normalized by the catalyst weight. These calculations were not performed for this work.

Table 10: Quantachrome iQ TPR macro.

Step	Action
1	Change gas to helium
2	Outgas/Leak Test
3	MFC: set flow rate to 50 sccm (gas type He)
4	Ramp temp to 110 at 10 deg/min
5	Flow until set point
6	Flow for 30 min
7	Force cool furnace for 50
8	Change gas to 10% H_2 90%N_2
9	MFC set flow rate to 50 Sccm
10	TCD device on
11	Flow for 30 min
12	Start TPR acquisition
13	Ramp T to 800 at 10 deg/min
14	Flow for 30 min
15	Flow until set point
16	End acquisition
17	TCD device off
18	Change gas to #1 nitrogen
19	Force cool furnace to 50
20	MFC turn off
21	Lower bath

X-Ray Diffraction

X-Ray Diffraction (XRD) provides a method of 'fingerprinting' a sample. On an atomic level, most materials contain distinct lattice structures, such as body centered cubic (BCC) or face centered cubic (FCC). X-rays are fired at the sample and diffracted by the lattice structure of the sample. A detector picks up the scattered signals, and the results are plotted as a function of the position of the detector as it varies from the position of the incident x-rays. Each species has its own

unique spectra. XRD was performed on a multiple number of samples using a Phillips X-Ray Diffractometer X'Pert PANalytical (see Figure 17).

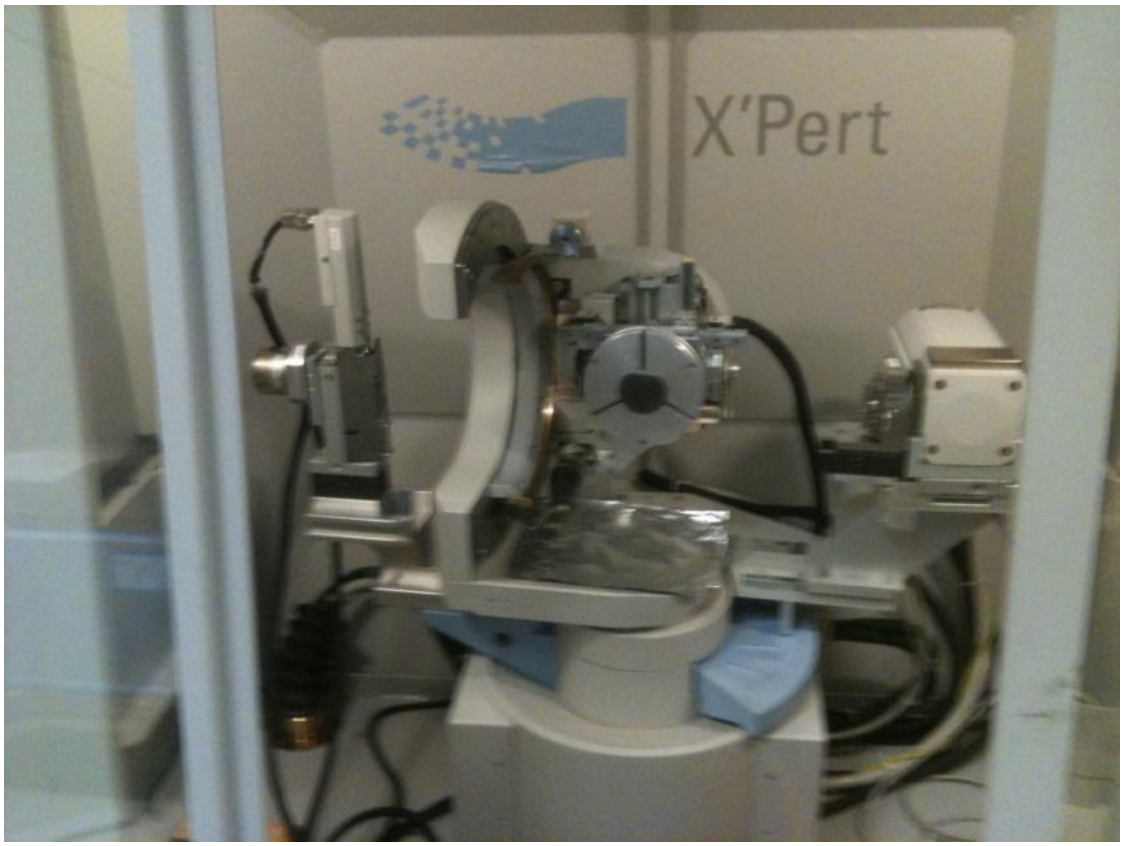

Figure 17: Philips X-Ray Diffractometer in NREC at USF. This instrument was used to generate all spectra related to this project. Sample is mounted on a zero diffraction plate.

In order to mount the powder sample on the zero-diffraction plate (see Figure 18), the samples had to be ball milled and passed through a 100 micron sieve. The powder was statically held onto the zero-

diffraction plate, and placed on the sample holder section of the diffractometer (see Figure 18).

Figure 18: Ball mill and 100 micron sieve.

All samples were run at a scan rate of 0.0200 deg/sec, λ = 1.541874 Å. All spectra were measured from 20° - 80° 2Θ. In literature the first spinel peak reported was at 18.92° 2Θ [78]. This angle was used in calculations in calculations, though it is not included in the spectra. Table 11 lists the instrument settings for XRD.

Table 11: Philips X-Ray Diffractometer settings.

SETTING	VALUE
Start Position [°2Th.]	20.0100
End Position [°2Th.]	79.9900
Step Size [°2Th.]	0.0200
Scan Step Time [s]	0.5000
Scan Type	Continuous
Offset [°2Th.]	0.0000
Divergence Slit Type	Fixed
Divergence Slit Size [°]	1.0000
Specimen Length [mm]	10.00
Receiving Slit Size [mm]	0.2000
Measurement Temperature [°C]	25.00
Anode Material	Cu
Generator Settings	45 kV, 40 mA
Goniometer Radius [mm]	320.00
Dist. Focus-Diverg. Slit [mm]	91.00
Incident Beam Monochromator	No
Spinning	No
Wavelength [nm]	0.1541874

X-Ray Diffraction's history started in the 1900s when Bragg and his son noticed that diffracted x-rays were able to give off patterns of spectra for solids [100]. They introduced Bragg's Law:

$$n\lambda = 2dsin(\theta) \tag{18}$$

where n= any integer,

λ = incident wavelength in nm,

d = line spacing in between atomic lattices in nm, and

Θ = angle in between the lattice planes and incident x-rays.

From Bragg's Law, Miller Indices can further be calculated. These are calculated as a function of position on the spectra via the following equation:

$$\frac{\lambda}{2a}^{2} = \frac{sin^2\theta}{h^2+k^2+l^2} \quad (19)$$

where,

a = lattice parameter in nm and

h,k,l, = Miller index values.

Since $sin^2\Theta$ is proportional to $h^2 + k^2 + l^2$, ratios can be utilized to solve for the Miller Indices. Multiplying these ratios by integers provides possible sums of the three values. Since the values are reciprocals of planar Cartesian coordinates, they must be equal to a whole number. Indexing rules for FCC unit cells were subsequently used in determining the proper indices. FCC unit cells must have their ratio multiplied by 3. The sum of the ratio must be a whole number which follows the following sequence: 3,4,8,11,12,16,19,20,24……40. For FCC structures, all three parts of the Miller Index (h,k,l), must either be odd or even. There cannot be a mixture of odd and even. Therefore, logic is thus employed to compute Miller Index values. For example, if $(h^2 + k^2 + l^2) = 3$, the index is (111); for $(h^2 + k^2 + l^2) = 8$ the index is (220).

Once the sum of the square has been calculated ($h^2 + k^2 + l^2$), equation 19 can be used to back calculate the lattice constant a. These calculations are shown in Appendix V.

A traditional Mg-Al spinel has a FCC unit cell and a lattice constant reported to be 0.8080 nm [101]. The lattice constant can change if the spinel is not stoichiometric, i.e. $n \neq 1$ [102]. Different algebraic correlations have been suggested based on testing to formulate a function to calculate the lattice parameter based on d spacing and different numbers for n. These values range from 0.7963 to 0.8086 nm [101].

Uncertainty in Measurements

The greatest uncertainty value (σ) pertains to temperature. Temperature measurements were taken with an observed variation of ± 5 °C. Table 12 lists the uncertainty values for each variable tested in this experiment. Calculations for uncertainty in CO conversion are shown in Appendix VI.

Table 12: Propagation of error.

Property	Units	Symbol	Value
Temperature	°C	σ_T	5
Flow	ccm	σ_f	0.1
TCD Signal	mV	σ_s	0.01
Surface Area	m^2/g	σ_{BET}	0.01
GC Peak Area (Observed)	µV*s	σ_A	10
GC Peak Area Calibration Constant (CO)	µV*s/ccm	σ_{CCO}	1577
Calculated Flow	ccm	σ_{fcalc}	0.105
Calculated Flow	mol/min	σ_n	$4.00 * 10^{-6}$
Conversion	%	σ_X	5.8

Though these values are not explicitly stated throughout the findings of this thesis, the reader is expected to interpret the data with the σ values tabulated in Table 12.

CHAPTER VI: RESULTS AND DISCUSSION

Schematic

To assist the reader in differentiating between catalyst samples, the following color scheme is presented in Table 13.

Table 13: Sample color-coded schematic.

Sample	Synthesis	Calcination Temp
$CeCo_2O_4$	Pechini	700 °C
$CeCo_2O_4$ w/ 10 wt% MoO_3	Pechini w/ ICW	450 °C
$Ce_{0.9}Mo_{0.1}Co_2O_4$	Pechini	700 °C
$Fe_{2.5}Ce_{0.25}Co_{0.25}O_4$	Pechini	500 °C

Results for Ce-Co spinel will be shown in orange. Results for Ce-Co with 10% Mo added by ICW will be shown in red. Results for $Ce_{0.9}Mo_{0.1}Co_2O_4$ will be shown in black. Results for $Fe_{2.5}Ce_{0.25}Co_{0.25}O_4$ will be shown in blue.

Temperature-Programmed Reduction Results

Prior to any reaction testing, temperature-programmed reduction (TPR) was performed on the experiments to provide a base point for reaction temperature testing specific to the catalyst itself. Though

WGS reaction temperature ranges are well known, TPR indicates whether the catalyst will be able to be active within the temperature range of interest. The temperature profiles show a reduction range of 253 °C - 800 °C (all samples). This range covers the industrial LTS and HTS range.

Though ceria is a great oxygen conductor, it is not an optimum material for reduction. $CeCo_2O_4$ by itself was the worst performing sample in TPR studies. $CeCo_2O_4$ was tested twice in two different instruments to gauge the accuracy of the measurements. The mass spectrometer provided a better reduction profile with one sole peak (see Figure 19). This sample had the lowest reduction temperature of the four tested. This test confirms the first peak shown by the Quantachrome TPR (shown in Figure 23). The spike after that appears to be an adaption to a new base point, and should not be considered as temperatures for reduction.

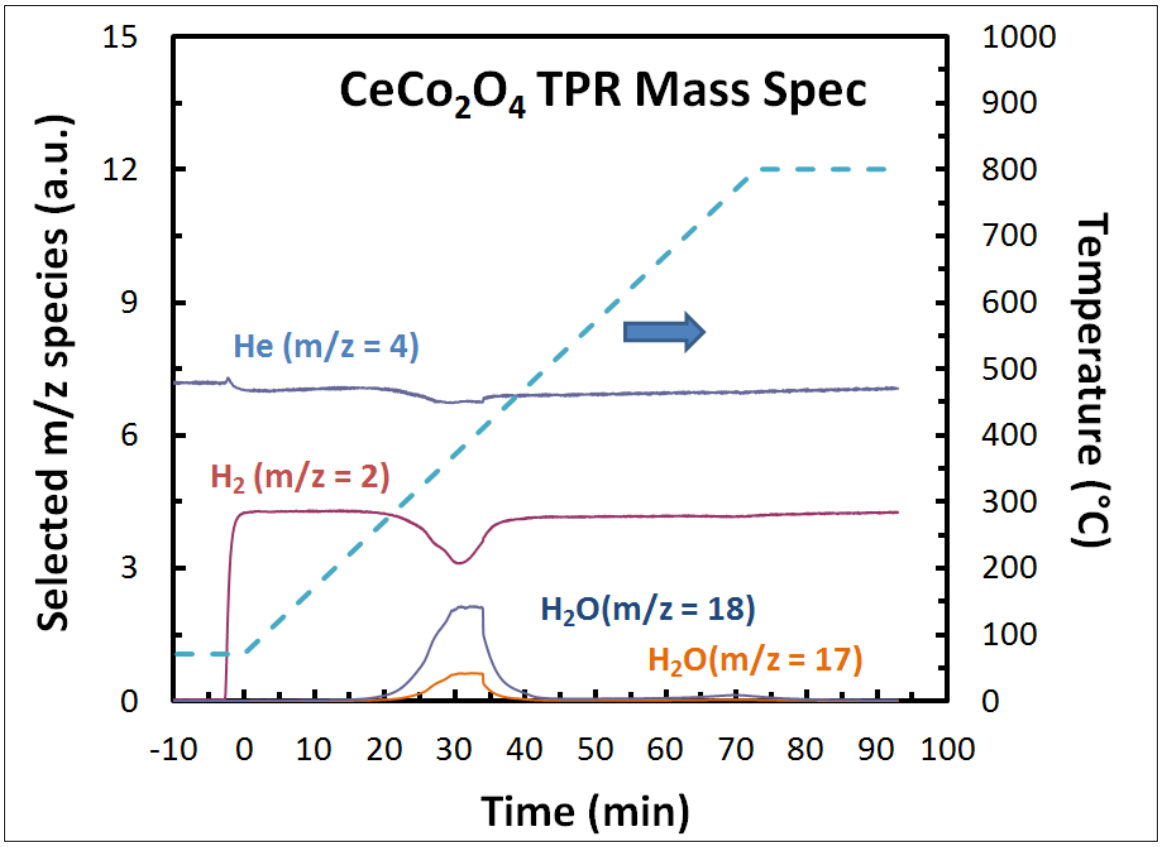

Figure 19: Mass spectrometer rendering of CCO TPR profile. H_2O was created and measured. This data was not normalized to fit the TCD signal.

The addition of molybdenum via incipient wetness to the $CeCo_2O_4$ matrix greatly enhanced the reducibility of the catalyst. However, the onset temperature shifted significantly from the $CeCo_2O_4$ onset, as reduction started at approximately 380 °C. It also was more robust in providing a greater temperature range for reduction. Figure 20 shows the results.

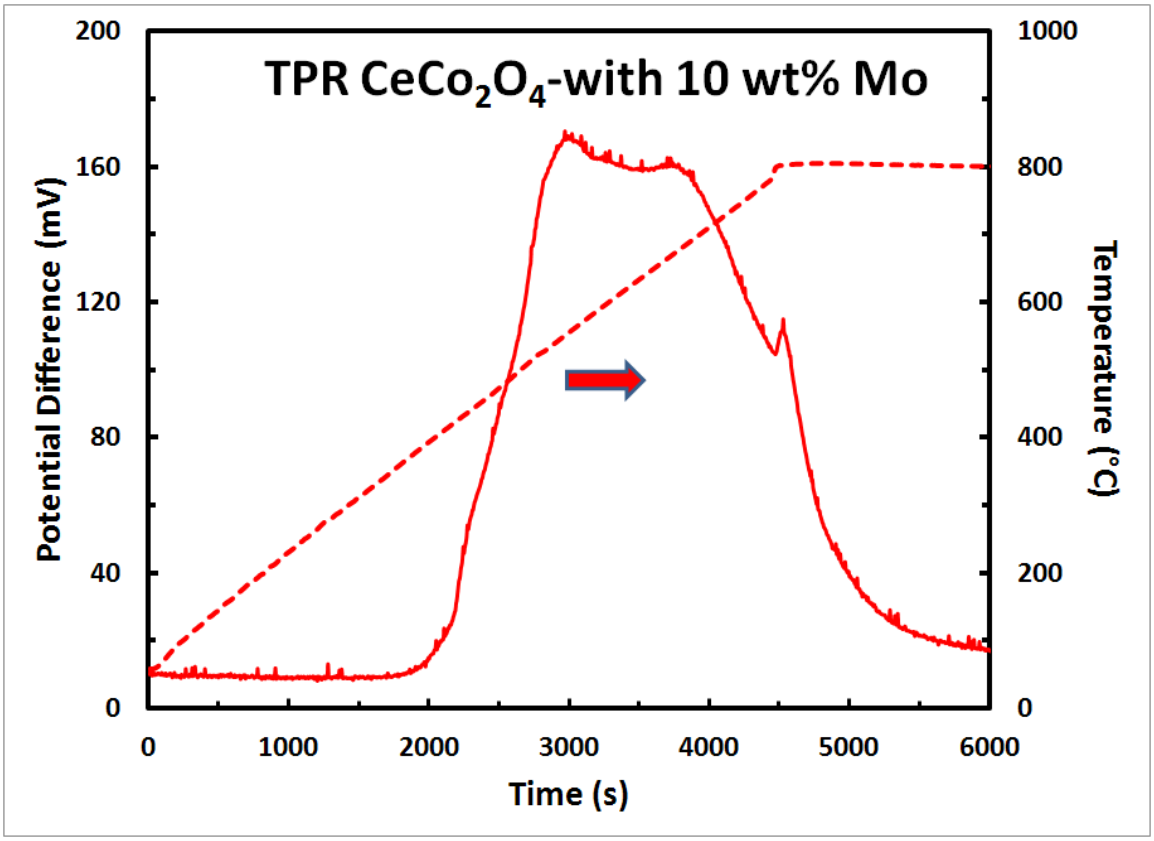

Figure 20: TPR profile of CCO with Mo. Molybdenum adds reduction to the regular CCO matrix.

Even small amounts of Mo incorporated inside the spinel matrix enhanced the reducibility of the Ce-Co spinel. Incorporation of a smaller amount of Mo lowered the reduction onset temperature to approximately 300 °C. The potential difference (TCD signal = mV measured – mV reference) was also considerably higher for $Ce_{0.9}Mo_{0.1}Co_2O_4$. Figure 21 shows the TPR profile. The TPR profiles characterize a difference between Mo incorporation to the lattice, and Mo added via an incipient wetness synthesis technique.

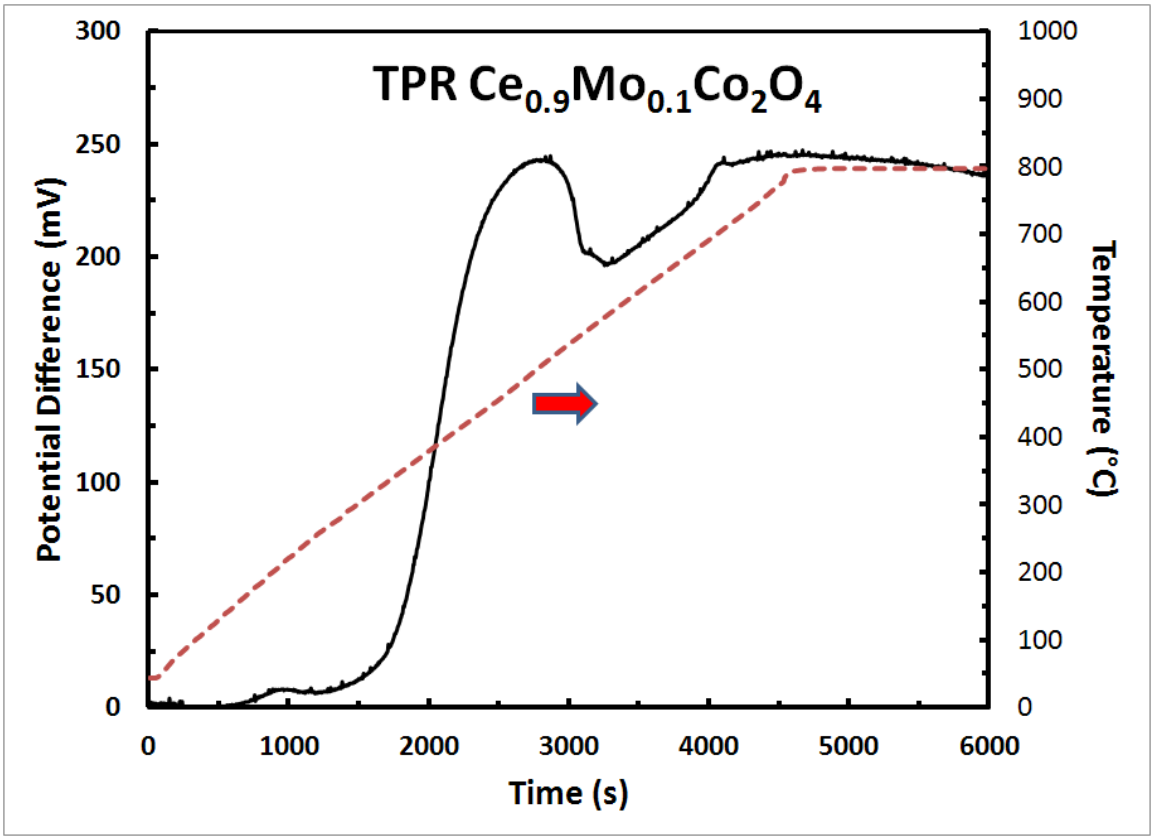

Figure 21: TPR profile of CMCO. Addition of Mo into spinel matrix adds reduction potential to catalyst.

The TPR profile of the predominantly Fe based spinel is the most unique. It displays four different peaks, and 3 of them contain their maxima right in the temperature range for HTS reactors (375 °C – 500 °C [37]). These peaks correlate to the reduction of hematite to magnetite, and further reduction to wustite at higher temperatures. The fourth peak is the largest reduction feature (Figure 22). The temperature for this peak (757 °C) is outside the temperatures of interest for this study.

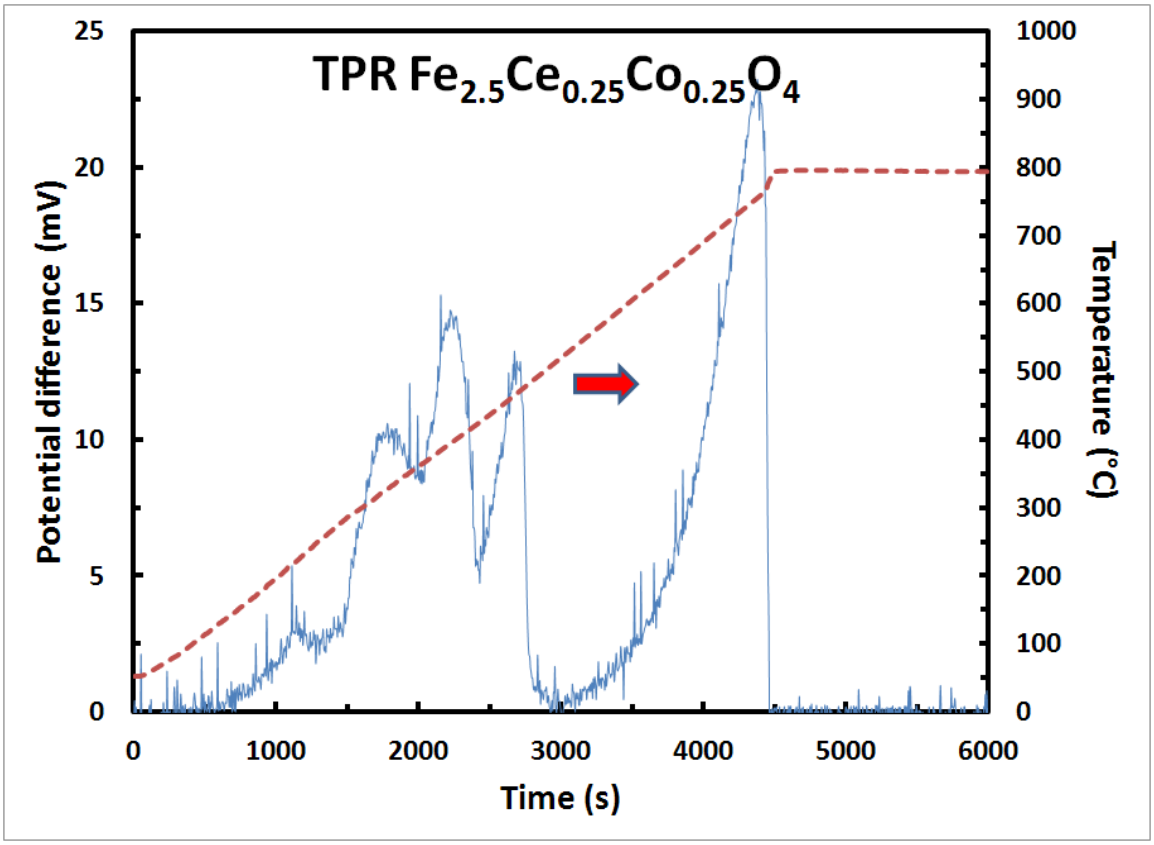

Figure 22: TPR profile for FCCO. Fe has 4 different peaks for reduction.

Table 14 comprises the important data points of interest from the TPR profiles. The onset temperature is a good indicator of what temperature the catalyst will be favored to be active under a given reaction. The peak temperature is a heuristic indication of when to expect maximum reducibility (activity) for a given catalyst.

Table 14: Important reduction temperatures.

Catalyst	Onset Temperature (°C)	Peak Temperature (°C)
$CeCo_2O_4$	253	363
$CeCo_2O_4$ with 10% Mo	383	544
$Ce_{0.9}Mo_{0.1}Co_2O_4$	300	495
$Fe_{2.5}Ce_{0.25}Co_{0.25}O_4$	278, 571	393,757

For comparison, the profiles are plotted as a function of temperature only in Figure 23. Using heuristics, the optimum catalyst should be $Ce_{0.9}Mo_{0.1}Co_2O_4$ with a reaction maximum activity at a temperature range 375 °C – 500 °C. The $CeCo_2O_4$ is best equipped to provide greater activity at lower temperatures. Addition of Mo to $CeCo_2O_4$ greatly increases the reduction onset temperature.

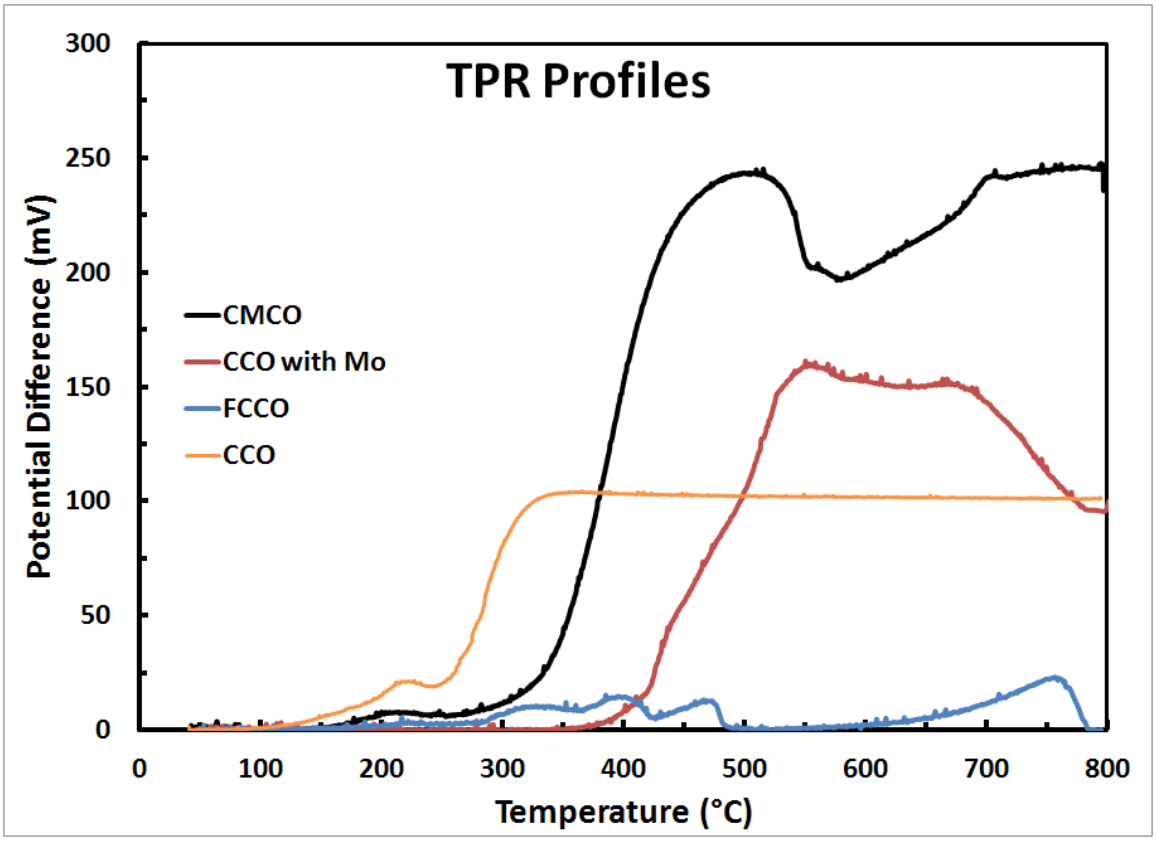

Figure 23: Comparison of TPR profiles.

Reaction Results

The reactions were tested at 3 temperatures 350 °C, 375 °C, and 400 °C. This was done to provide baseline testing at lower temperatures to fulfill the need for sulfur tolerance at lower temperatures. Some samples were tested at 300 °C, and are shown in the following figures. Since the reactions were not studied at lower conversions, kinetic data is unavailable for this experiment. For comparison, the observed rate of the reaction was normalized via catalyst weight and surface area. $CeCo_2O_4$ exhibited a strong performance in higher levels of sulfur.

Near equilibrium conversion was attained at 800 ppm H_2S at 79.52%. The greatest conversion was achieved at 375 °C. At 350 °C, unsulfided $CeCo_2O_4$ samples exhibited selectivity to methane (See Figure 25). This was expected since cobalt is a known Fischer-Tropsch catalyst [60]. It was interesting to note that the selectivity to methane only happened at 350 °C for the unsulfided catalyst. At 400 °C, a trace amount of methane was detected on one of ten GC injections (S_{CH4} < .01%). This was not enough to corroborate methanation at these temperatures. Near equilibrium conversions are shown at high concentrations of sulfur. This is because CO is converting to CO_2 and CH_4.

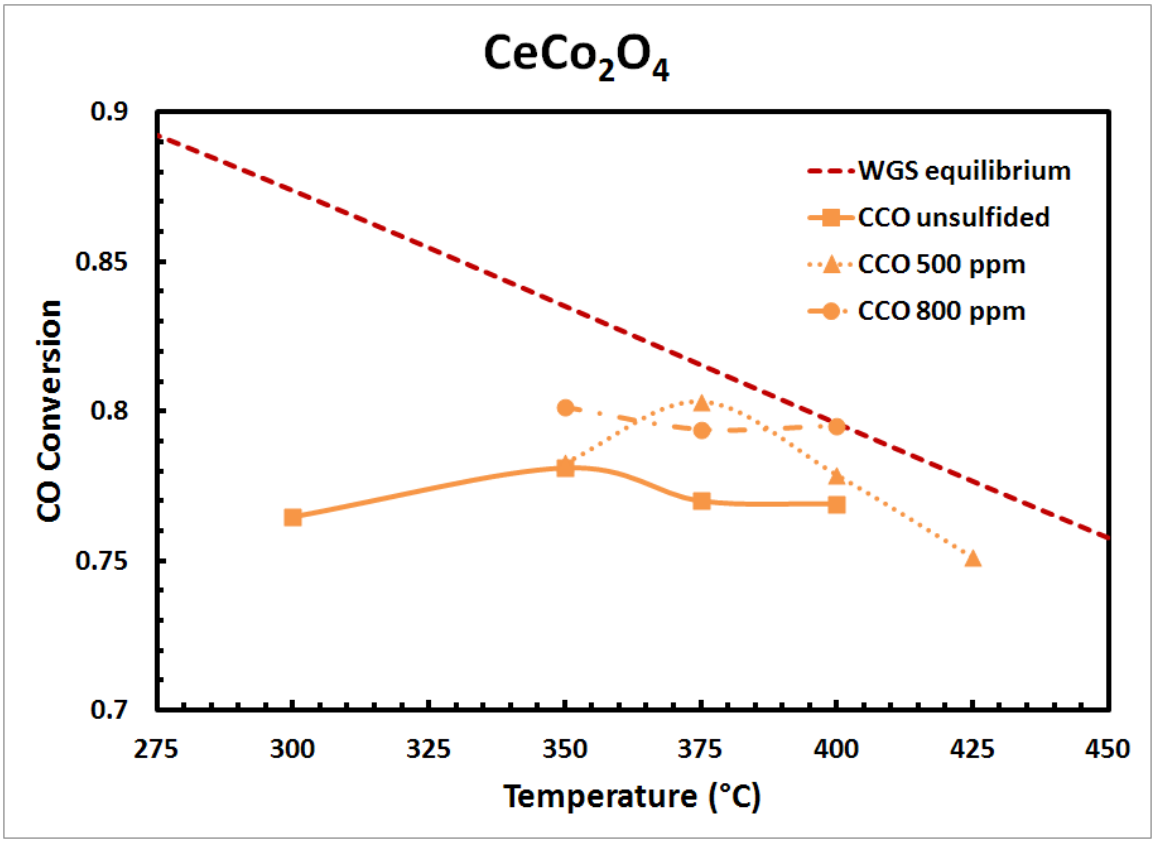

Figure 24: Reaction results for $CeCo_2O_4$. (Note: Conversion shown is CO to CO_2 conversion. Conversion to CH_4 was removed from results.)

Figure 24 shows the results for the unsulfided and sulfided reactions. Addition of sulfur increased CO conversion from the unsulfided sample. 5% of the inlet CO converted to methane in lieu of CO_2. This phenomena was also unaffected by the sulfur. The same amount of methane was still present in sulfided runs below 400 °C. This reaction was tested at 425 °C as well. No methanation was observed at this temperature. These results are not directly in line with some findings in literature. Liu et al. observed an interruption to methanation with

the addition of just 20 ppm H_2S to a Pt/Ceria catalyst [47]. Like Liu, Copperthwaite [48] observed similar results with a Co-Cr spinel in 220 ppm H_2S.

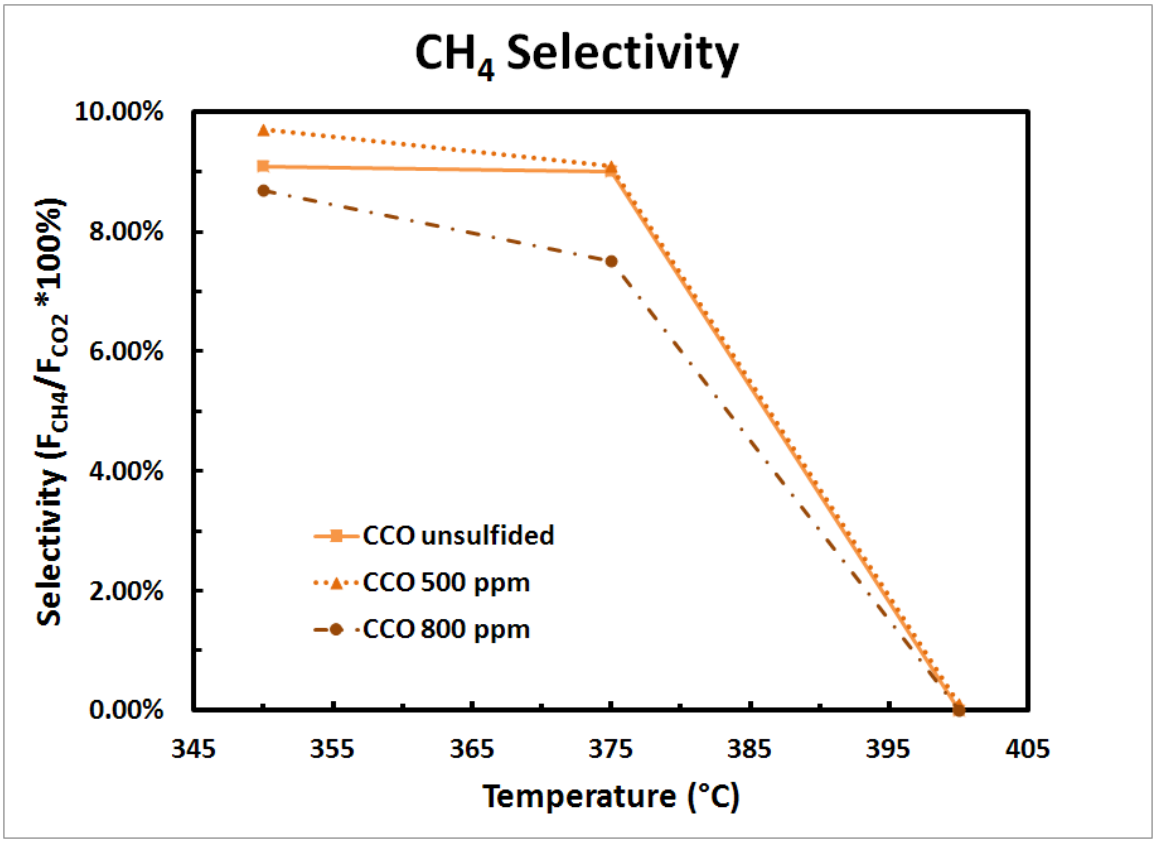

Figure 25: Selectivity of $CeCo_2O_4$ to methanation.

The addition of Mo via ICW to the Ce-Co spinel was thought to increase sulfur tolerance. The sample maintained modest conversion in the sulfur free feed, attaining its highest conversion (80%) at 350 °C. The sample deactivated much quicker in higher levels of H_2S. However, at 500 ppm, a level of sulfur typical in biomass streams

[42], conversions remained at approximately 75%. At 400 °C, the conversion of the unsulfided and the sulfided at 500 ppm catalyst is barely differentiable. However in higher levels of sulfur, the decrease in activity is clearly visible. The addition of Mo eradicated any selectivity to methanation. It is also noteworthy to point out that this catalyst was demonstrated at lower temperatures for unsulfided streams. It maintained modest conversion at 250 °C (71 %). It was the only catalyst to be tested at such a low temperature.

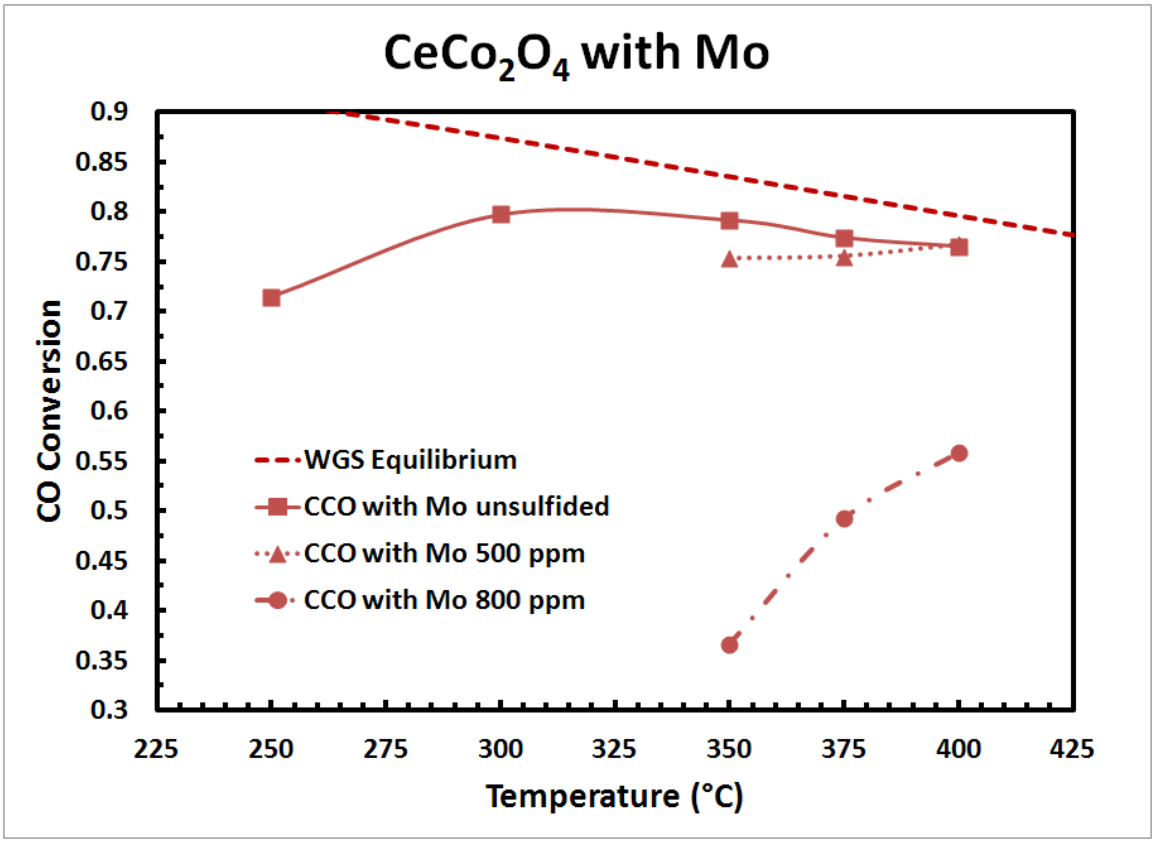

Figure 26: Reaction results for $CeCo_2O_4$ with Mo.

The incorporation of Mo into the Ce-Co spinel was tested for sulfur tolerance. Comparatively, there is not much difference in conversions of the unsulfided catalyst and sulfided at 500 ppm catalyst. The decrease in activity is approximately 1%. These results seem to suggest no correlation with the addition of molybdenum to the already fabricated Ce-Co spinel, and the incorporation of the sulfur-tolerant Mo into the spinel matrix. Both conversions at 500 ppm H_2S are in the 75% range. The deactivation of the catalyst in higher concentrations of sulfur is also similar. In fact, one $Ce_{0.9}Mo_{0.1}Co_2O_4$ sample completely deactivated while being tested at 375 °C. A fresh sample had to be used and retested to acquire conversion at 350 °C.

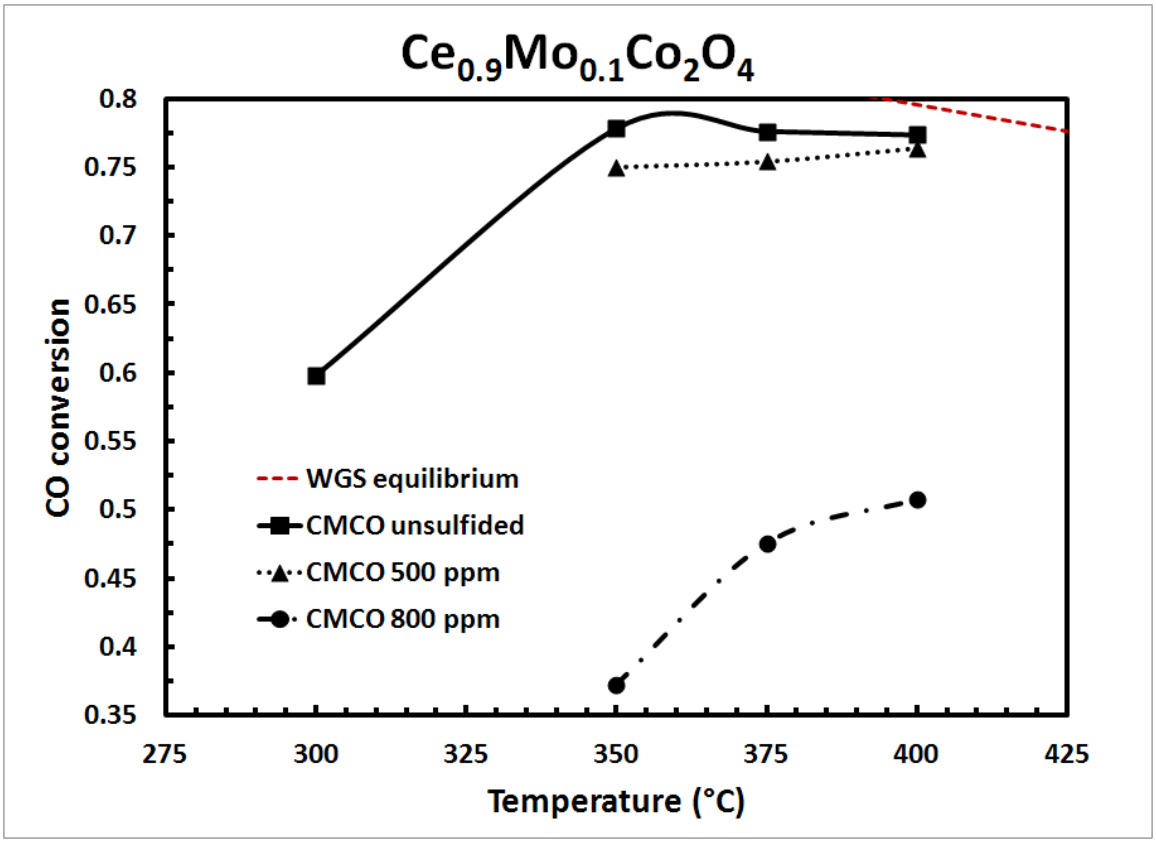

Figure 27: Reaction results for $Ce_{0.9}Mo_{0.1}Co_2O_4$.

Given iron's reign as the standard WGS catalyst, the results for the Fe-Ce-Co spinel are somewhat surprising. Higher conversions were expected for the increased iron content. In the unsulfided case, conversion did increase with temperature.

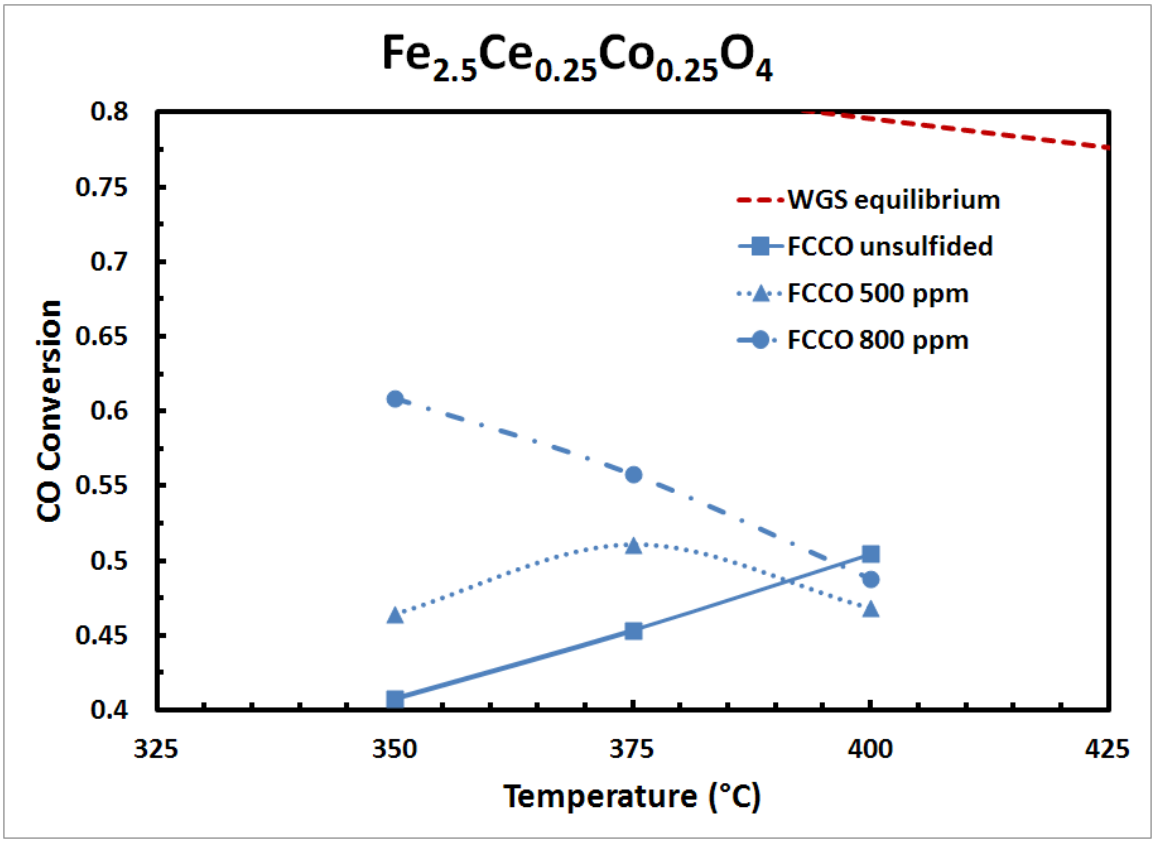

Figure 28: Reaction results for $Fe_{2.5}Ce_{0.25}Co_{0.25}O_4$.

Compared to Reddy, Boolchand, and Smirniotis' results, conversion in this temperature range was slightly better [74], though not as robust as traditional WGS Fe-Cr catalysts. Reddy et al. achieved near equilibrium conversion at 550 °C. Their results are shown in Figures 29-30. The opposite trend was observed for the sulfided catalysts. There was also a trend of decreasing conversion with temperature for the sulfided catalysts. It is known that industrial ferrochrome catalysts lose about half their activity in sulfur [33]. However, compared with

the data in Figure 30, the trend is different. It is also important to note the S/G ratio for this experiment is approximately 1.

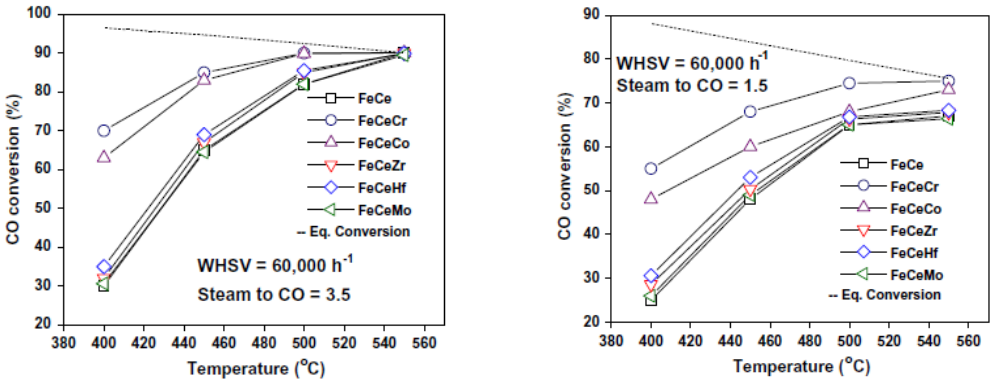

Figure 29: CO conversion of various FeCe based catalysts. Unsulfided and 3.5 S/G (left), 1.5 S/G (right) [74]. (Reprinted with permission from Elsevier.)

The results observed from Reddy's work were reviewed in Chapter IV of this thesis. In the temperatures (400 °C, mainly) tested in this work, the $Fe_{2.5}Ce_{0.25}Co_{0.25}O_4$ catalyst exhibited greater activity than the Fe/Ce catalyst. Results are slightly more comparable with the Fe/Ce/Co catalyst.

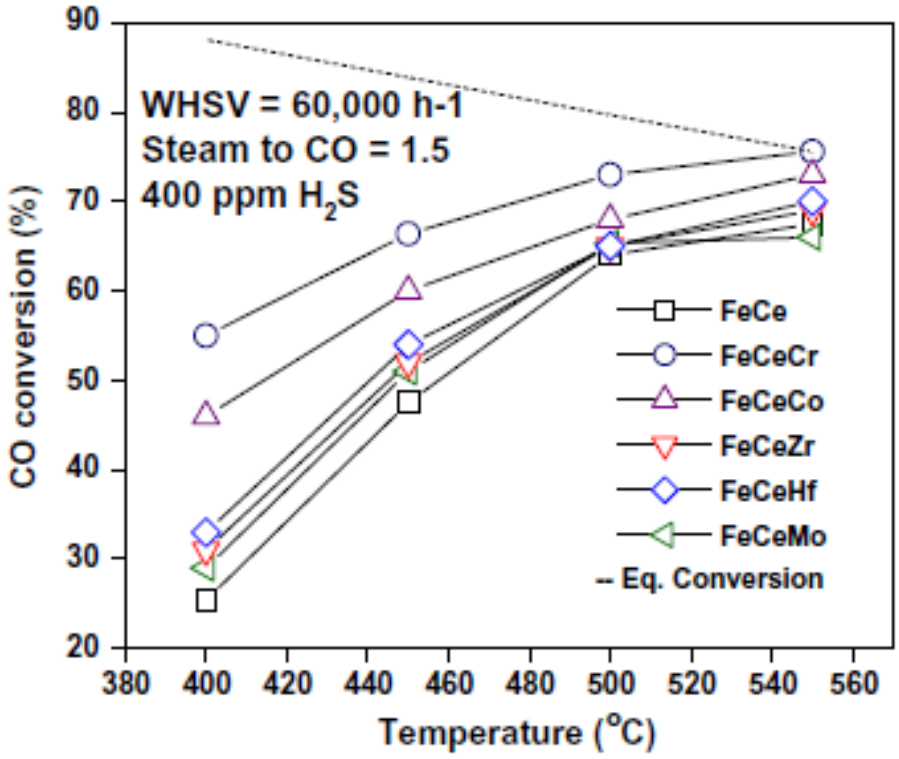

Figure 30: CO conversion of various FeCe based catalysts sulfided and low SG. [74] (Reprinted with permission from Elsevier.)

Due to industrial needs of pH Matter, and the desire to demonstrate a catalyst at lower temperatures, temperatures in excess of 425 °C were not reported in this work.

Figure 31 shows all catalyst samples tested in this thesis. It does not appear that Mo had any effect on conversion in sulfur. The best performing catalyst was the Ce-Co spinel. The worst performing catalyst was the Fe-Ce-Co spinel. It also is shown that in the case of

heavy sulfiding, a decline in activity was observed in all the catalysts except the Ce-Co spinel.

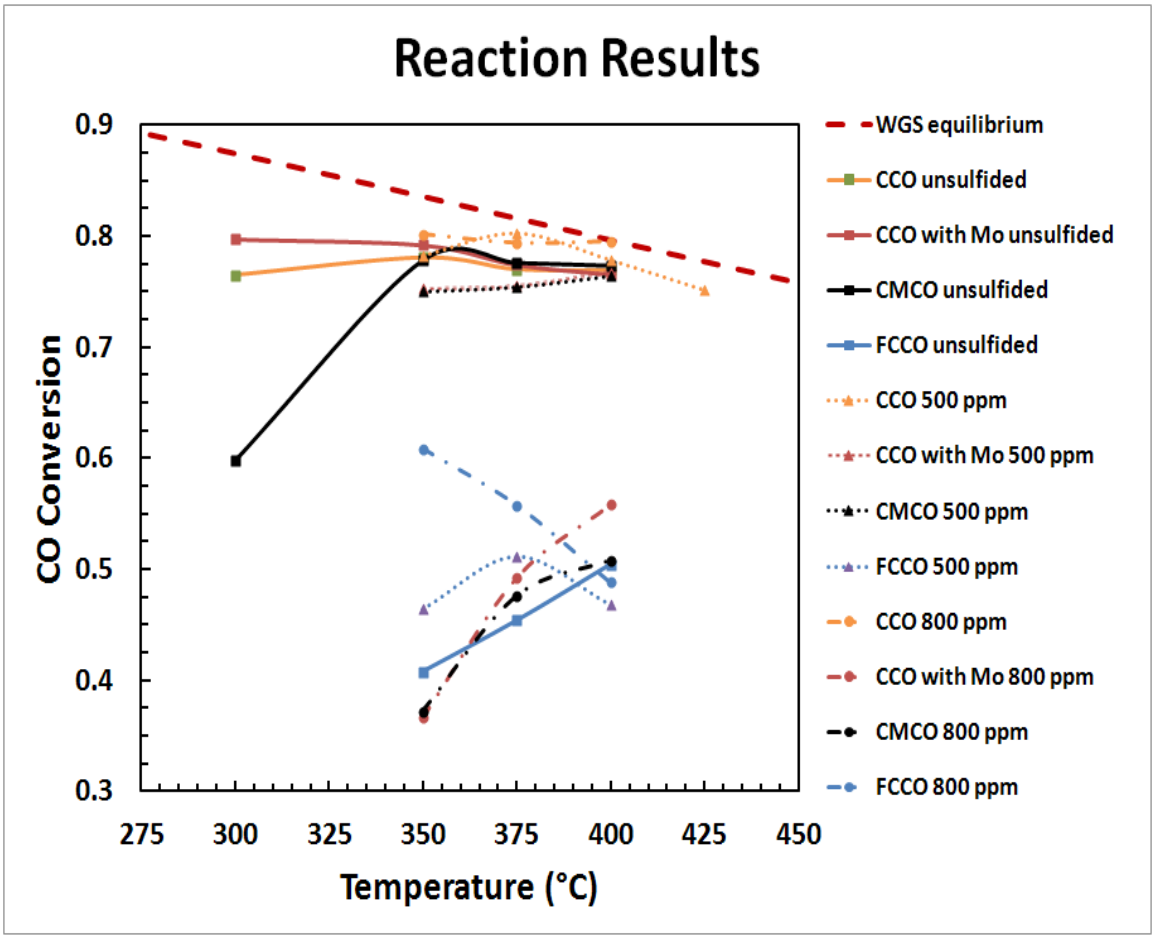

Figure 31: Complete reaction results. (■ =unsulfided, ▲= sulfided at 500 ppm, ● = sulfided at 800 ppm)

Table 15 is presented to assist the reader compare significant data points and extrema from initial activity testing.

Table 15: Reaction results extrema.

Condition	Criteria	Temperature (°C)	Sample	CO Conversion
Unsulfided	Greatest Conversion	350	$CeCo_2O_4$ with Mo	0.79
	Greatest Conversion	375	$Ce_{0.9}Mo_{0.1}Co_2O_4$	0.77
	Greatest Conversion	400	$Ce_{0.9}Mo_{0.1}Co_2O_4$	0.77
Unsulfided	Lowest Conversion	350	$Ce_{0.9}Mo_{0.1}Co_2O_4$	0.77
	Lowest Conversion	375	$CeCo_2O_4$	0.77
	Lowest Conversion	400	$CeCo_2O_4$ with Mo	0.76
Sulfided at 500 ppm H_2S	Greatest Conversion	350	$CeCo_2O_4$	0.78
	Greatest Conversion	375	$CeCo_2O_4$	0.80
	Greatest Conversion	400	$CeCo_2O_4$	0.77
Sulfided at 500 ppm H_2S	Lowest Conversion	350	$Ce_{0.9}Mo_{0.1}Co_2O_4$	0.75
	Lowest Conversion	375	$Ce_{0.9}Mo_{0.1}Co_2O_4$	0.75
	Lowest Conversion	400	$Ce_{0.9}Mo_{0.1}Co_2O_4$	0.76
Sulfided at 800 ppm H_2S	Greatest Conversion	350	$CeCo_2O_4$	0.79
	Greatest Conversion	375	$CeCo_2O_4$	0.79
	Greatest Conversion	400	$CeCo_2O_4$	0.79
Sulfided at 800 ppm H_2S	Lowest Conversion	350	$Ce_{0.9}Mo_{0.1}Co_2O_4$	0.41
	Lowest Conversion	375	$Ce_{0.9}Mo_{0.1}Co_2O_4$	0.47
	Lowest Conversion	400	$CeCo_2O_4$ with Mo	0.36

$Fe_{2.5}Ce_{0.25}Co_{0.25}O_4$ is not reported in this table. This was done for reader to differentiate between the Ce-Co samples.

Table 15 excludes $Fe_{2.5}Ce_{0.25}Co_{0.25}O_4$. Figure 31 clearly shows that the Fe-Ce-Co spinel was not as robust as the Ce-Co spinels and the Ce-Co spinels doped with Mo. The exclusion of the Fe-Ce-Co spinel was done to facilitate comparisons between the addition of Mo to the Ce-Co spinel and the incorporation of Mo into the spinel itself. Table 15 shows absolute extrema for all samples tested.

Table 16: Absolute reaction extrema.

Criteria	Sample	Temperature (°C)	Condition	CO Conversion
Greatest Conversion	$CeCo_2O_4$	375	Sulfided at 500 ppm	0.8032
Lowest Conversion	$CeCo_2O_4$ with 10 wt% MoO_3	400	Sulfided at 800 ppm	0.3658

The rate of CO consumed per catalyst weight is interesting to observe as well. Figure 32 shows the rate of CO consumed normalized per catalyst weight vs. the Temperature. For the most part, this should follow the trend seen in conversion in Figure 30. The $CeCo_2O_4$ remains the most robust catalyst in CO consumption as a function of catalyst weight. At steady state conditions with a GHSV at approximately 60,000 hr^{-1}, rates above 5.5×10^{-4} of moles consumed per gram per minute can be attained.

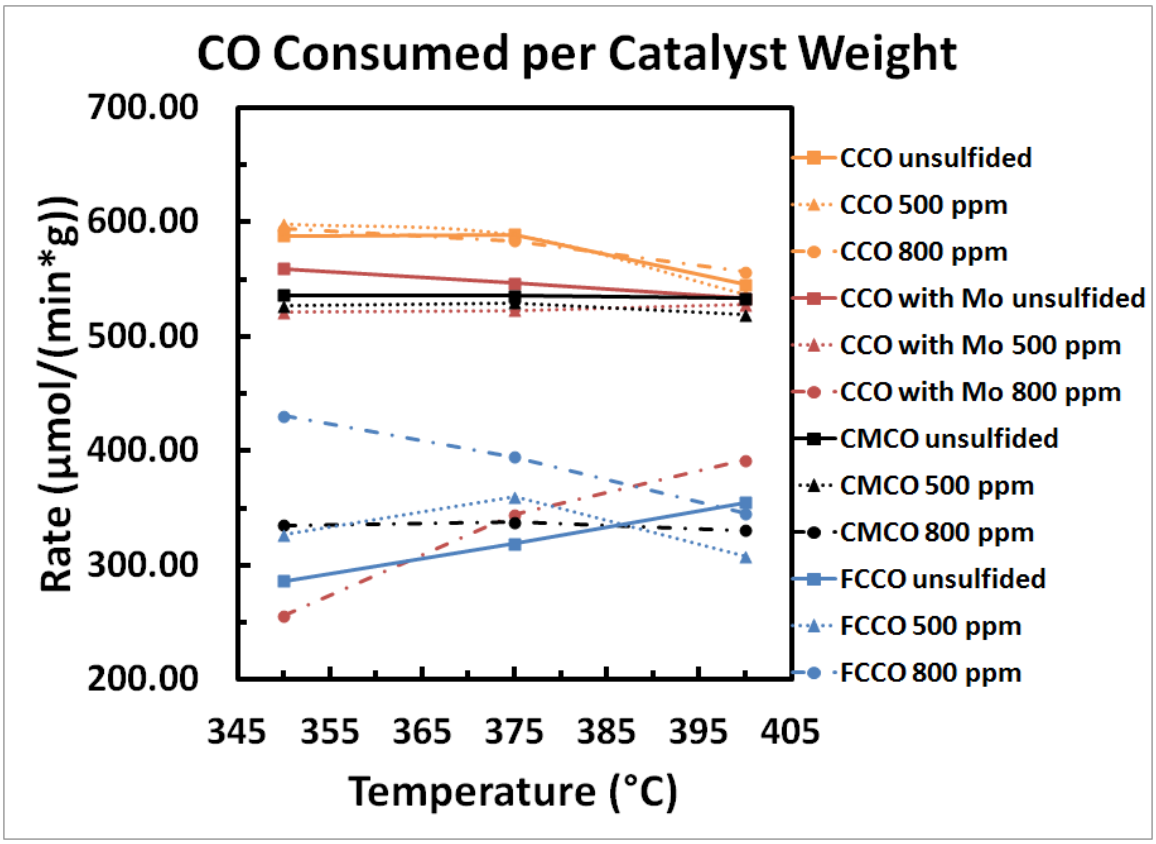

Figure 32: Rate of CO consumed per catalyst weight.

It is also noteworthy to mention the feed tested is ideal for WGS conditions (only CO and H_2O in the presence of an inert). Typical biomass-derived syngas streams, however, contain greater concentrations of competing reactants such as O_2, CO_2, CH_4, N_2, H_2 and sulfuric compounds [16]. A more industrial gauge of measuring the selectivity of our catalysts would be to leave other species in the reactor feed. This was performed once over sulfided $Ce_{0.9}Mo_{0.1}Co_2O_4$ in excess H_2 (F_{H2} = 5 ccm, $H_2/CO = H_2/H_2O = 3.125$). The results are shown in Figure 33.

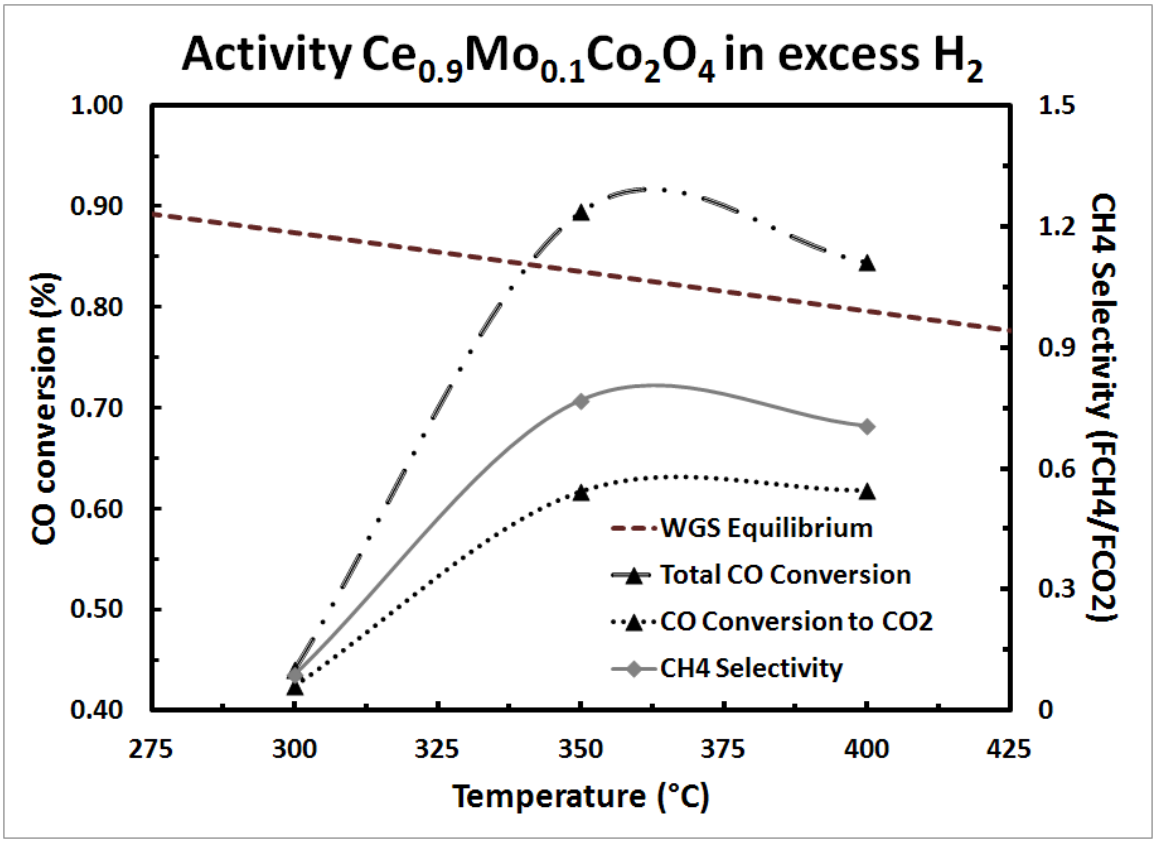

Figure 33: Results for a H_2 heavy feed. Catalyst was tested while sulfided in 500 ppm H_2S.

The results are not unexpected. With excess H_2 in the feed, the reaction preferentially selected methanation. It is interesting to point out though, that 60% conversion to CO_2 was also attained, with a sulfided catalyst. Total CO conversion exceeds the WGS equilibrium. Be not fooled by this, since more than the WGS reaction was transpiring. Since this was only performed (and performed accidentally) over one catalyst, future testing is needed to confirm catalyst selectivity preferences.

X-Ray Diffraction Results

The calculated lattice constants were similar to those found in literature for a common FCC spinel (0.80015 – 0.81243). At first pass, not all the ratios of the peaks were in line with a FCC spinel unit cell. Though originally different orientations were also considered since pressure can change certain spinel phases [103], careful inspection showed the spectra indicated an overlapping fluorite pattern as well. Since ceria is well known to have FCC fluorite structure [104], this was not unexpected. Therefore, two sets of parameters were needed to calculate Miller indices: the spinel structure, and the fluorite structure. Calculations are shown in Appendix V.

Figure 34 shows the spectra for all the samples unsulfided compared to a common spinel base and a common fluorite base. The data for the base structures were obtained from X'Pert Highscore, the accompanying software package for the Phillips X-Ray Diffractometer. Both the spinel and the fluorite have a peak at 59.31° 2Θ, with Miller Indices of (511) and (222) respectively.

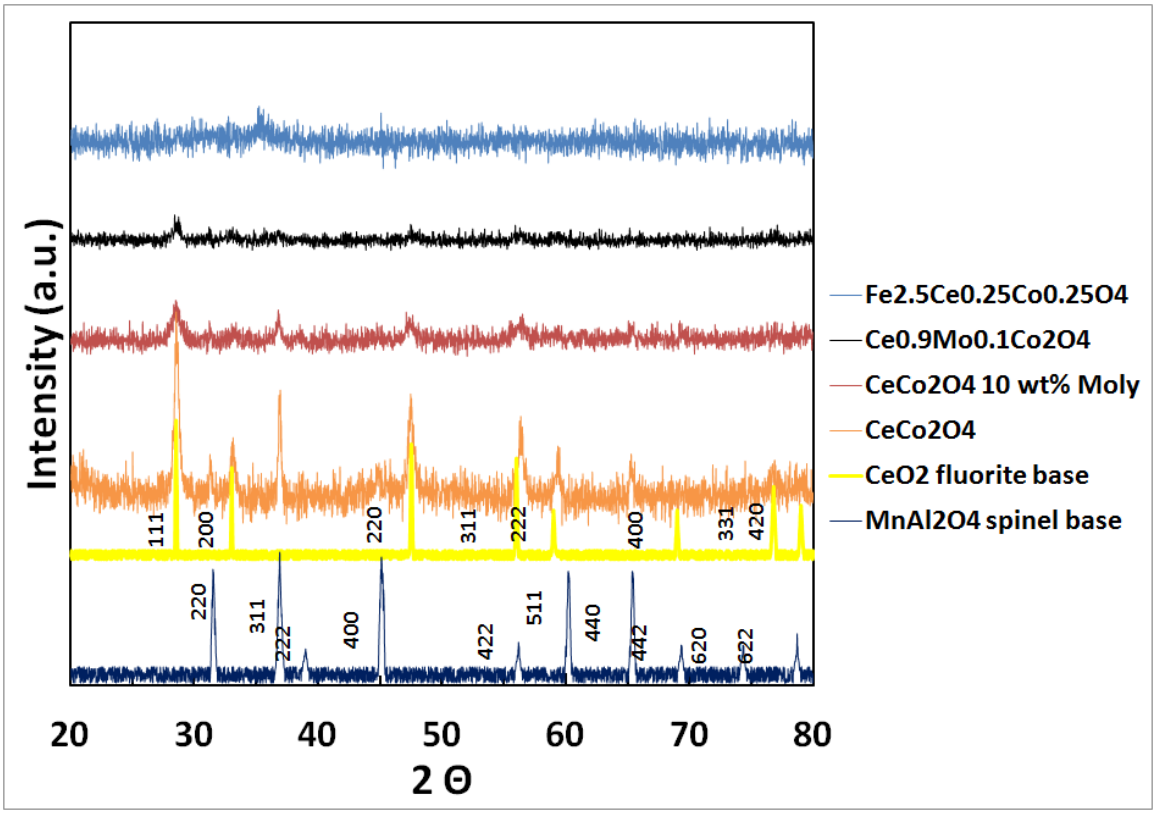

Figure 34: Base XRD spectra.

After sulfidation, the spent Ce-Co spinel appears to lose the spinel indicating peaks, and remains with only a ceria fingerprint. Only the (311) peak at 36.81° 2Θ is visible in the spinel structure. The rest of the peaks are indicative of a fluorite structure. The spectra results are plotted in Figure 35.

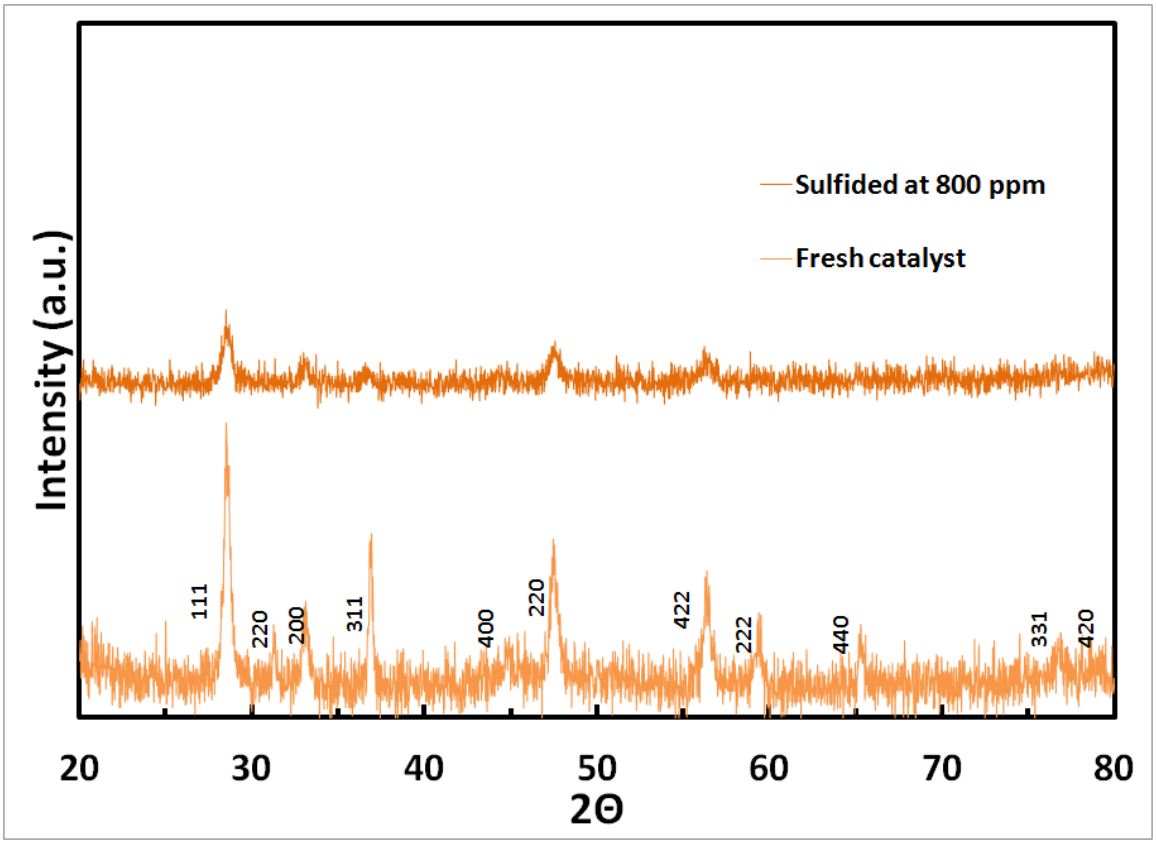

Figure 35: Diffraction pattern for $CeCo_2O_4$.

The (442) spinel peak at 69.37° 2Θ is shown in the sulfided $CeCo_2O_4$ with Mo sample. It appears it could be visible just under the noise on the unsulfided sample, but it is much clearer in the first. The XRD profiles show some the overlapping spinel and fluorite structures (See Figure 36).

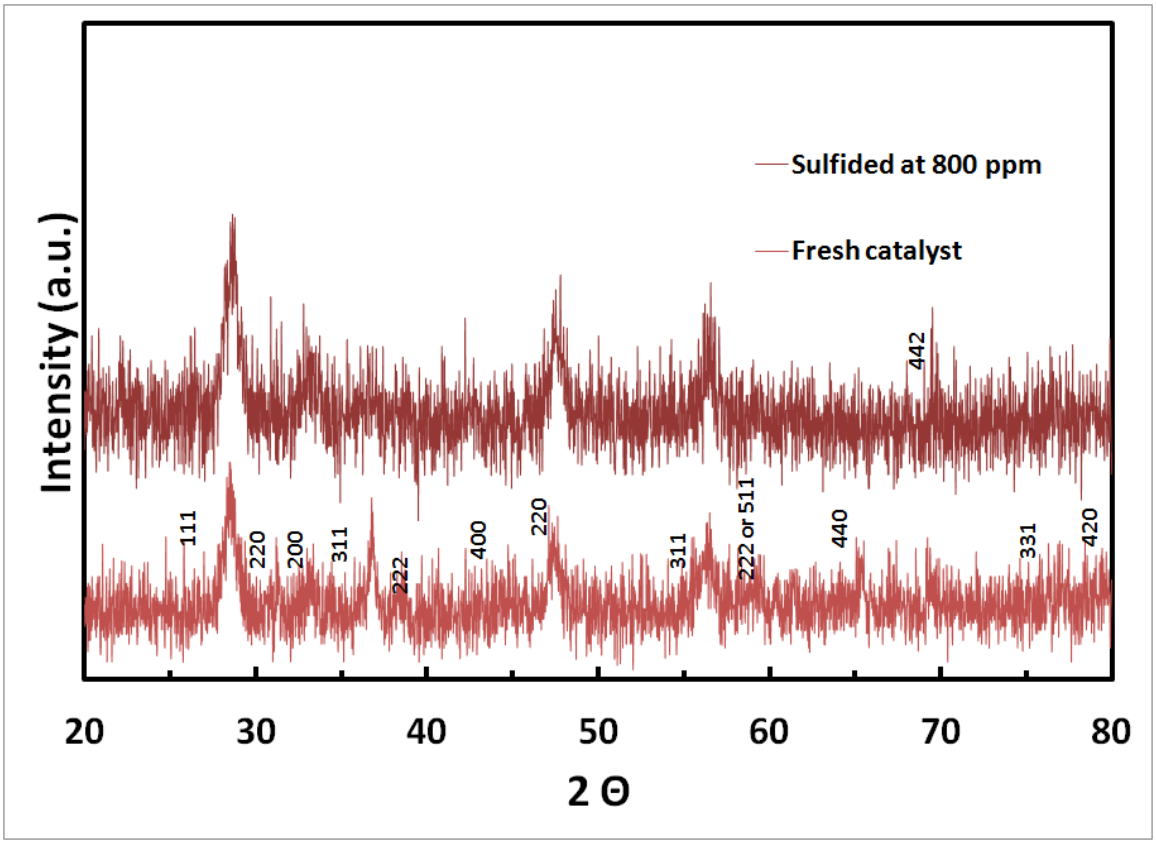

Figure 36: Diffraction pattern for $CeCo_2O_4$ with Mo.

Addition of sulfur eliminated the (220) spinel peak at 31.29° 2Θ in the sulfided $Ce_{0.9}Mo_{0.1}Co_2O_4$ catalyst. However, the (400) and (440) spinel peaks are much more pronounced in the sulfided sample. The reaction conditions did not change the overall physical structure of the catalyst (see Figure 37).

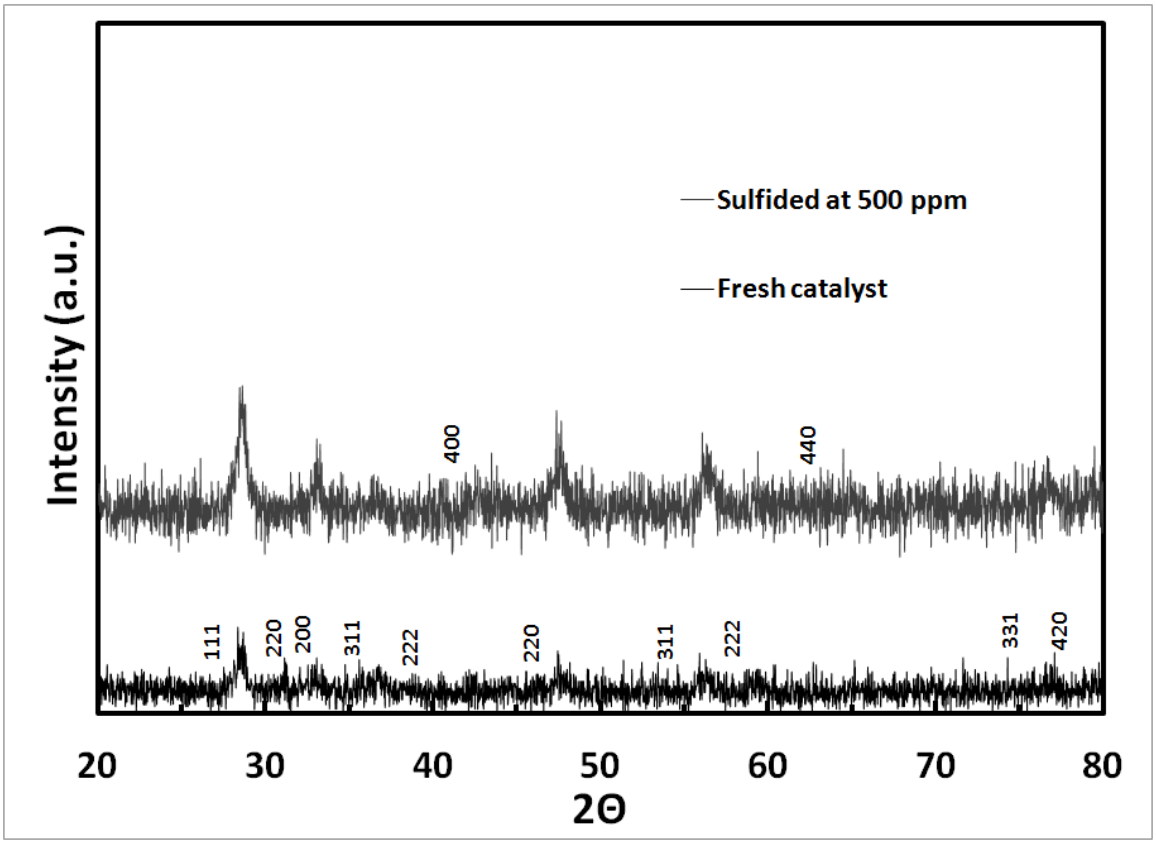

Figure 37: Diffraction pattern for $Ce_{0.9}Mo_{0.1}Co_2O_4$.

The Fe-Ce-Co catalyst is the sole catalyst to appear to undergo a significant change under reaction conditions. Not only was a 57% decline in surface area observed, the XRD spectra seems to depict a major shift. The (200) peak at 33.07° 2Θ on the fresh sample is attributed to Ce, while the (311) peak is attributed to a spinel peak. No other peaks are observed, and if they are there, they are not differentiable above the noise of the spectrum. The sulfided sample only yielded one peak at 44.75° 2Θ. This is attributed to the spinel structure at (400). This sample did not appear to have crystallized

enough during synthesis. It is unclear as to why the prominent peak changed after sulfidation. Without a careful eye, it would not be seen that ceria was indeed present (see Figure 38). The (311) peak was observed by Reddy et al. as well in their review of the Fe/Ce catalyst.

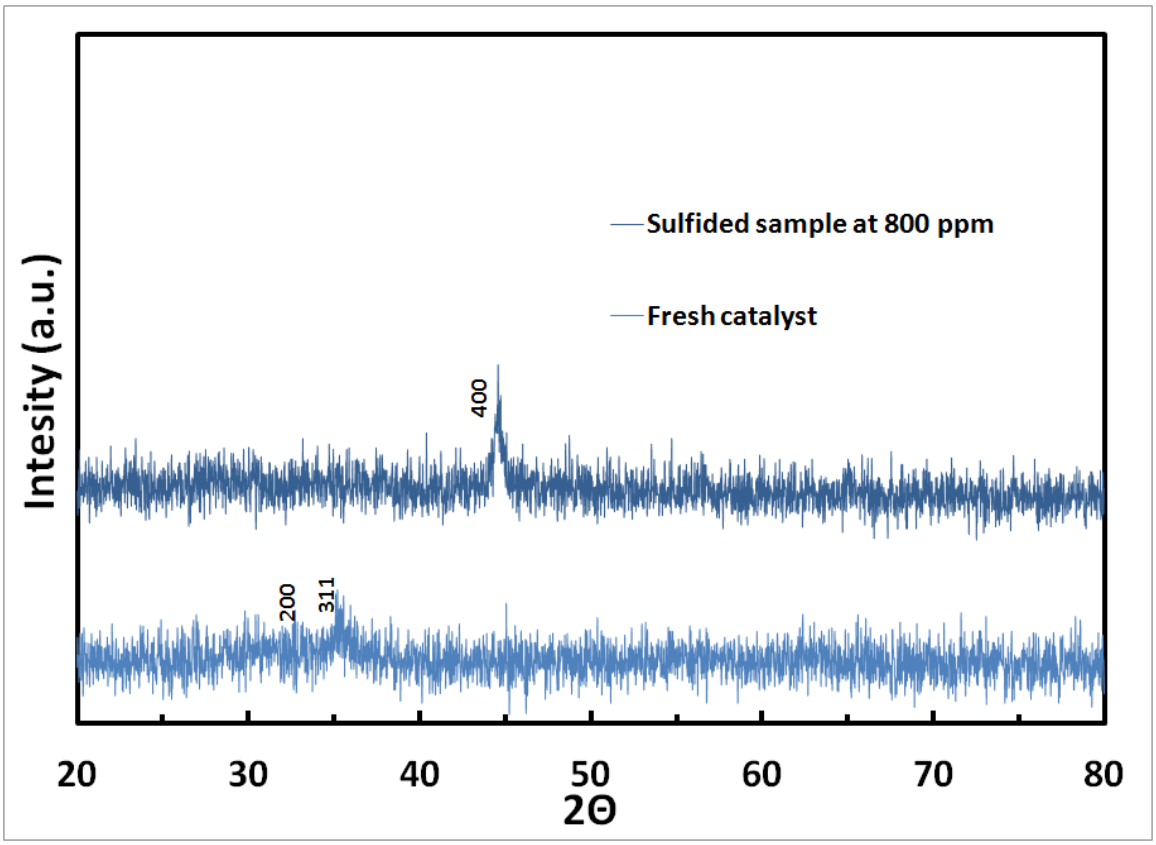

Figure 38: Diffraction pattern for $Fe_{2.5}Ce_{0.25}Co_{0.25}O_4$.

All the samples tested with ceria in the 'A' position in the spinel structure ($A^{2+}B_2^{3+}O_4^{2-}$) which seemed to have solid crystalline phases, which were relatively unaffected by sulfur adsorption to the surface. The spectral differences have been discussed, but it cannot be

unequivocally ascertained that all peaks were present in the spectra. Some peaks may have not been differentiable above the instrument noise level.

To answer the question: how is the observer certain that the addition of Mo to the surface of the Ce-Co spinel can be differentiated from the incorporation of Mo inside the spinel lattice? The following XRD spectra are presented in Figure 39.

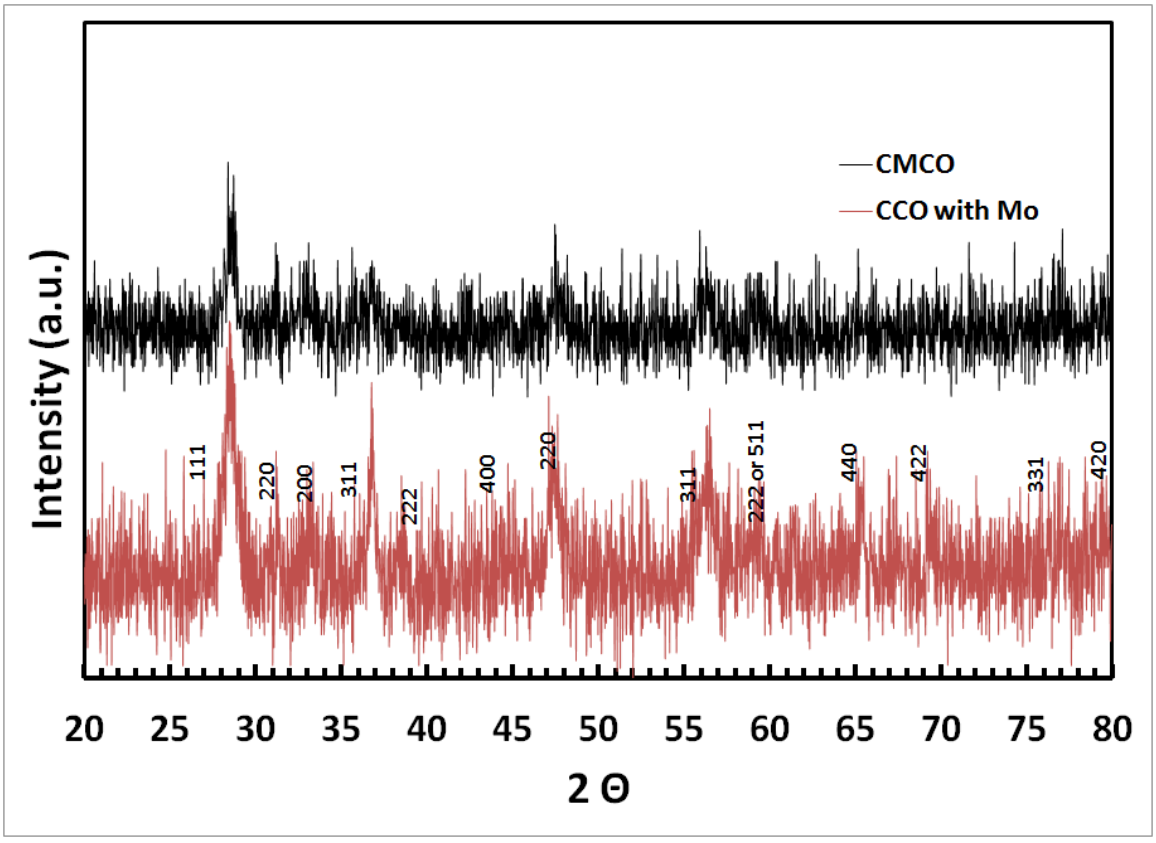

Figure 39: Comparison of diffraction patterns between $CeCo_2O_4$ with MoO_3 added via incipient wetness, and the Pechini synthesized $Ce_{0.9}Mo_{0.1}Co_2O_4$.

Inspection indicates similarities between the spectra. Both a spinel phase and fluorite phase are present as shown in Figure 32. The XRD spectra alone are not enough to distinguish a difference as peak shifts vary from ± 0.1 2Θ. However, the $CeCo_2O_4$ with Mo appears to have the (442) peak at 70° 2Θ, while the other sample does not. If the reader remains unconvinced that there exists uniqueness amongst the two samples, there are differences in the temperature programmed profiles (see Figure 22) and BET surface areas (see Table 16). This characterization should satisfy the reader with any doubts as to the difference between the samples.

Surface Area Results

Surface area by N_2 physisorption was performed on each fresh unsulfided sample, as well as spent catalysts after sulfidation. The surface area was calculated by the instrument software package. Figures 40-43 show the BET equation plotted as a function of relative pressure for each catalyst sample.

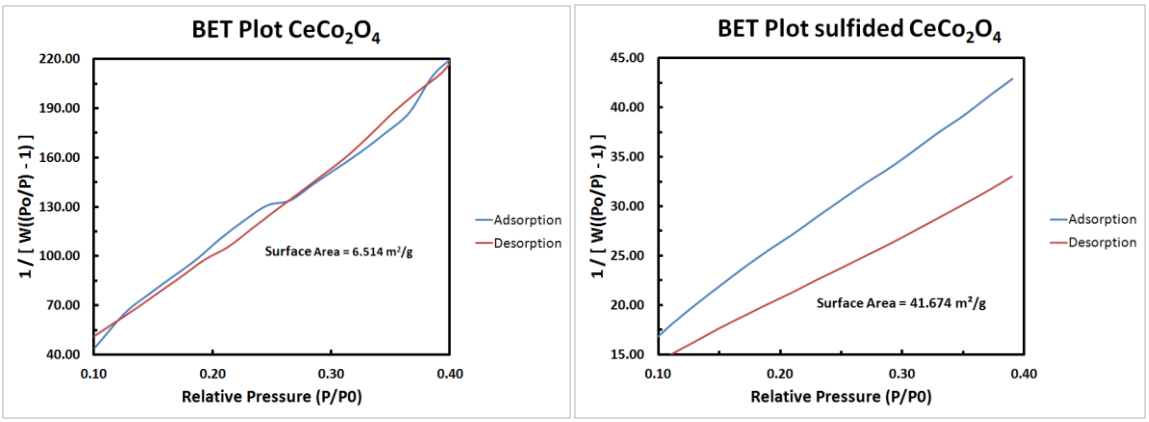

Figure 40: BET plot for $CeCo_2O_4$. Sulfided sample tested at 800 ppm.

Addition of sulfur increased the surface area significantly for the Ce-Co spinel. This is an approximately a 500 percent increase in surface area from the fresh catalyst. When sulfided, this catalyst also saw a slight increase in activity.

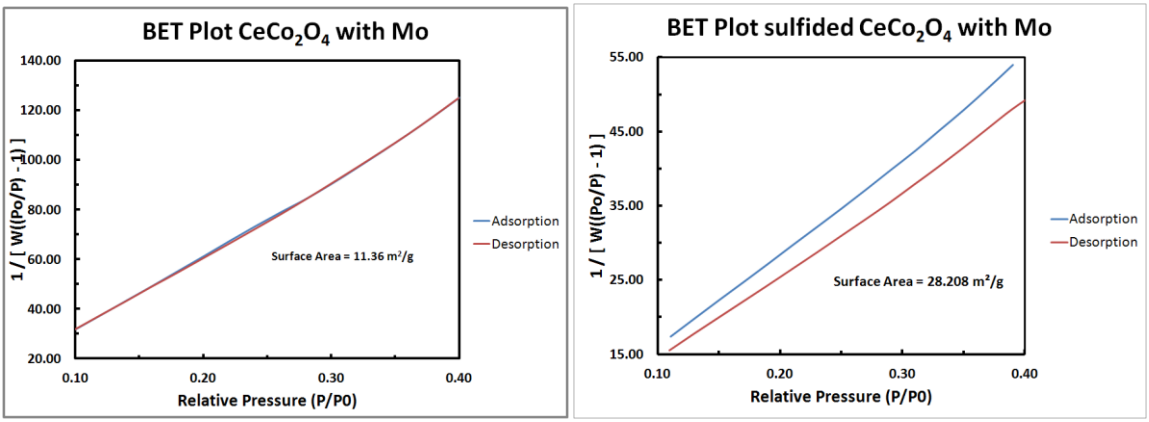

Figure 41: BET plot for $CeCo_2O_4$ with Mo. Sulfided sample tested at 800 ppm.

Sulfur also increased the surface area of the Ce-Co spinel with Mo by approximately 148%. The activity of this catalyst was adversely affected in higher levels of sulfur adsorption to the catalyst surface. At 500 ppm H_2S, the catalyst maintained nearly as active as the unsulfided catalyst. Surface area is not a definitive benchmark of catalytic measurement for this sample.

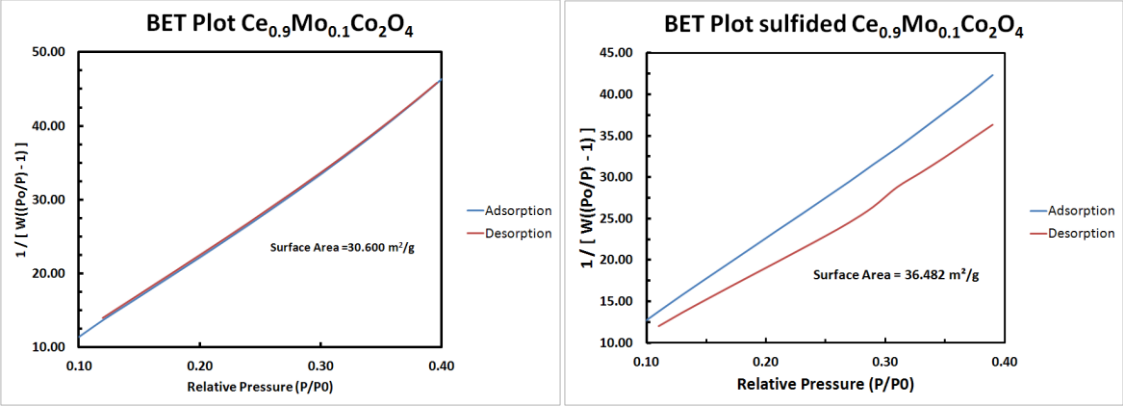

Figure 42: BET plot for $Ce_{0.9}Mo_{0.1}Co_2O_4$. Sulfided sample tested at 500 ppm.

Incorporating Mo into the spinel increased the surface area for the unsulfided sample. The addition of sulfur had little effect, but there was an increase of approximately 20% in surface area from H_2S adsorption.

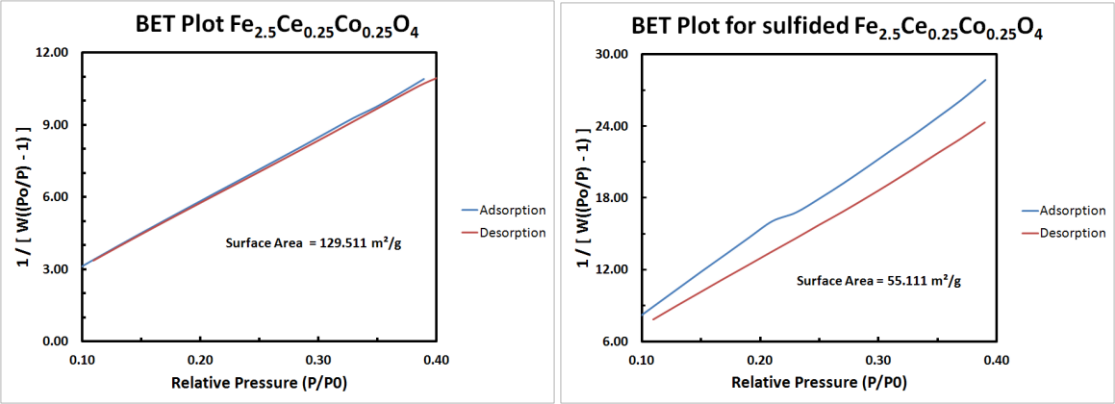

Figure 43: BET plot for $Fe_{2.5}Ce_{0.25}Co_{0.25}O_4$. Sulfided sample tested at 800 ppm.

The Fe-Ce-Co spinel had similar surface area to Reddy et al.'s (135 m^2/g) [74]. This is the lone catalyst which bucks the trend of increasing surface area with after sulfidation. Significant surface area is lost in high concentrations of sulfur: 57%. Reddy did not test post-reaction surface area; therefore, a literature comparison cannot be drawn. The loss in surface area would lead to the assumption of catalytic sintering. However, the unsulfided pore diameter (calculated via the BJH method on instrument software) Dv (d) = 3.533 nm, while the sulfided pore diameter was Dv (d) = 9.719 nm. This increase in pore size is not consistent with the loss of surface area. Another possible explanation of surface loss is the adsorption of H_2S to the catalyst surface.

Table 17 provides a comparative overview of all the mixed metal oxide samples.

Table 17: BET surface area results.

Sample	Fresh Catalyst Surface Area (m^2/g)	Unsulfided Surface Area (m^2/g)	Sulfided Surface Area (m^2/g)
$CeCo_2O_4$	24.8	6.5	41.7
$CeCo_2O_4$ w/ 10 wt% MoO_3	17.6	11.4	28.2
$Ce_{0.9}Mo_{0.1}Co_2O_4$	34.2	30.6	36.5
$Fe_{2.5}Ce_{0.25}Co_{0.25}O_4$		129.5	55.1

Table 18 provides an overview of the extrema exhibited in surface area calculations. Comparisons shown are drawn from the fresh catalyst surface area to the sulfided surface area.

Table 18: Surface area extrema.

	Criteria	Sample	Value
Unsulfided	Greatest Surface Area	$Fe_{2.5}Ce_{0.25}Co_{0.25}O_4$	129.511 (m^2/g)
	Lowest Surface Area	$CeCo_2O_4$	6.514 (m^2/g)
Sulfided	Greatest Surface Area	$Fe_{2.5}Ce_{0.25}Co_{0.25}O_4$	55.111 (m^2/g)
	Lowest Surface Area	$CeCo_2O_4$ w/ 10 wt% MoO_3	28.208 (m^2/g)
From unsulfided to sulfided	Greatest Percent Increase	$CeCo_2O_4$	+539.8%
	Lowest Percent Increase	$Ce_{0.9}Mo_{0.1}Co_2O_4$	+19.22%
	Greatest Percent Decrease	$Fe_{2.5}Ce_{0.25}Co_{0.25}O_4$	-57.45%
	Lowest Percent Decrease	$Fe_{2.5}Ce_{0.25}Co_{0.25}O_4$	-57.45%

In order to further view the effect of sulfur in enhancing the surface area of the catalyst, rate of CO consumption vs. surface area of catalyst is a useful tool. Figure 36 expresses the rate of CO consumed over the surface area of the unsulfided and sulfided catalyst. Fresh pre-reaction, catalyst was used for the normalization of the rate. The rate was multiplied by the catalyst weight in order to express it

in $\frac{mol}{min*m^2}$. The results are somewhat surprising. The unsulfided $CeCo_2O_4$ with Mo exhibits the greatest performance. Though sulfur increased surface area, the conversion decreased. $Ce_{0.9}Mo_{0.1}Co_2O_4$ was tested at 500 ppm, not 800 ppm as the others were (The 800 ppm sample was spoiled after reaction, making post reaction characterization impossible). Though a 20% increase in surface area was observed, the rate of CO consumption diminished greatly. Similar results are witnessed for the $CeCo_2O_4$ and $CeCo_2O_4$ with Mo samples as well. Though the sulfided Ce-Co spinel remained active in the presence of sulfur, the rate decreased when normalized for surface area. It was able to maintain similar activity 7 times more surface area than the fresh catalyst. Though sulfur had clearly adsorbed to the catalyst surface, similar activity was maintained. The only drawback to this catalyst was 10% selectivity to methanation.

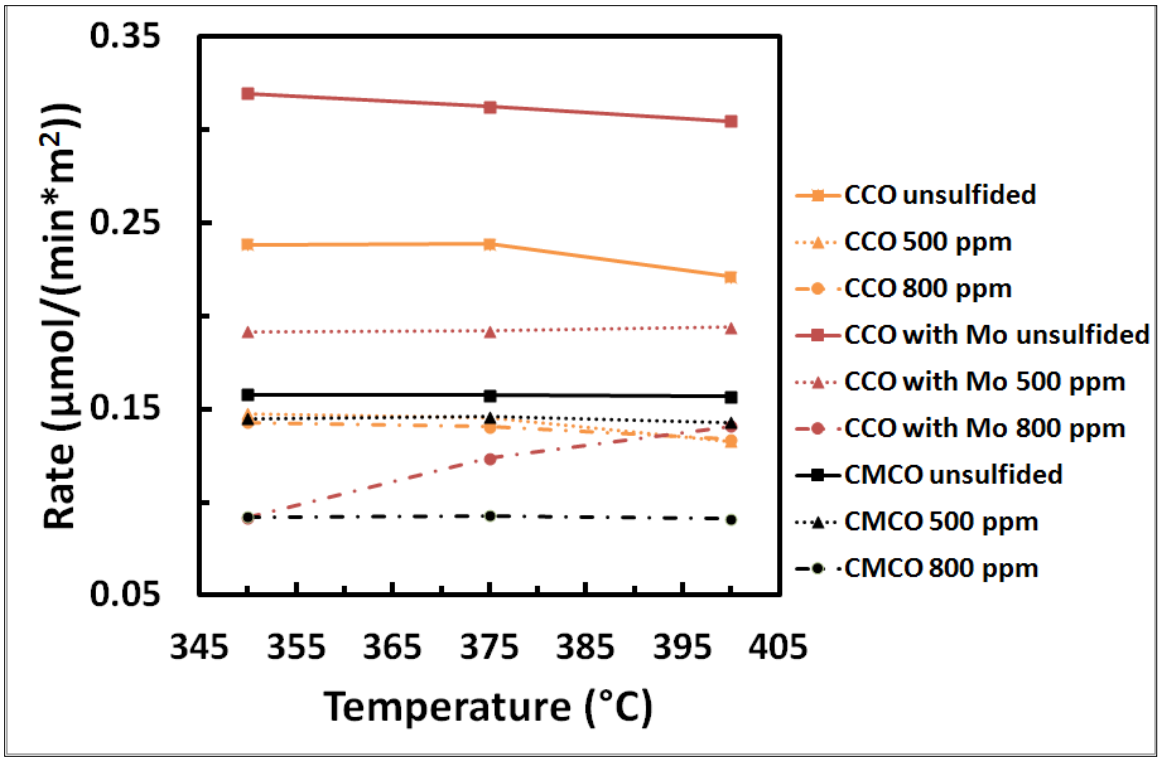

Figure 44: Rate of CO consumed as a function of surface area of catalyst.

It is interesting to note that all samples rate decreased upon sulfidation in the Ce-Co spinels. This is attributed to the increase in surface area upon sulfidation. While not shown in Figure 44, the reverse happened to the Fe-based spinel. Its surface area decreased, while there was not a large difference in activity. Therefore, the rate normalized per surface area increased slightly upon sulfidation.

CHAPTER VII: CONCLUSIONS

The Ce/Co spinel ($CeCo_2O_4$) was the catalyst which exhibited the greatest activity, though all the Ce/Co and Mo based spinels exhibited activity near the thermodynamic equilibrium in the WGS reaction in low concentrations of H_2S. However, $CeCo_2O_4$ also exhibited approximately 10% selectivity to the undesired Fischer-Tropsch reaction. The addition of Mo to the Ce-Co spinel eradicated any selectivity to methane over the temperature range tested, whether by incipient wetness or by direct incorporation to the spinel structure. Furthermore, $CeCo_2O_4$, $CeCo_2O_4$ with MoO_3, and $Ce_{0.9}Mo_{0.1}Co_2O_4$ demonstrated stability in initial activity tests at lower temperatures. Compared to Mellor et al.'s work [49], similar conversions were reached at 350-400 °C (80%) with a lower S:G ratio, and in higher concentrations of sulfur (500 ppm).

The addition of sulfur had no effect on the crystallinity of the Ce/Co based spinels. Bulk sulfides were not formed, and the relative mixed fluorite/spinel structure remained intact. The adsorption of sulfur enhanced the surface area of the Ce-Co oxides. Though the surface

area was increased, Mo had little to do in playing a role in sulfur tolerance in higher concentrations of sulfur. Incorporated into the spinel structure, it deactivated in higher levels of sulfur and needed to be regenerated. Sulfur adsorption opposite effect on the Fe-Ce-Co spinel. The crystallinity was unchanged, but sulfur adsorption did play a part into which peaks appeared prominently in characterization via XRD. Though the unsulfided $Fe_{2.5}Ce_{0.25}Co_{0.25}O_4$ spinel fared well to similar samples in literature, the loss of surface area was damaging to the activity of the Fe-Ce-Co spinel. TPR experiments confirmed the desired temperature range of typical HTS reactor conditions.

Future Work

Future work needed to support the findings of this thesis includes long term testing in sulfur-free feeds as well as sulfided streams. Should long-term testing prove stable, the catalysts should be retested with streams more closely resembling synthesis gas streams. H_2, CH_4, CO_2, COS, H_2S, N_2, O_2 and NO_x need to be incorporated into the feed. This will provide a more accurate litmus test to the catalysts' ability to preferentially select the WGS reaction. Testing in sub 50 ppm H_2S is also necessary to see how the catalysts perform in lower sulfur concentrations found in BTL plants. Higher temperatures should be tested for comparison with current HTS catalysts available in the

market (350 °C – 550 °C). Different ratios of Mo can be tested over the Ce-Co spinel to identify the ideal ratios for inhibiting CH_4 selectivity.

WORKS CITED

1. *Oil Crude and Petroleum Products Explained*. Oil Crude and Petroleum Products Explained 2010 [cited 2012 1/6/12]; Available from: http://www.eia.gov/energyexplained/index.cfm?page=oil_home#tab2.

2. *INTERNATIONAL ENERGY OUTLOOK 2011*. 2011. p. 37-39.

3. *The WORLD FACTBOOK*, CIA, Editor. 2012.

4. *Emissions of Greenhouse Gases in the United States 2008*, EIA, Editor. 2009.

5. *Renewable & Alternative Fuels*. 2009 August, 2010 [cited 2011; Available from: http://www.eia.gov/cneaf/alternate/page/renew_energy_consump/rea_prereport.html.

6. Gray, D.W., C., Tomlinson, G., Ackiewicz, M., , *Increasing Security and Reducing Carbon Emissions of the U.S. Transportation Sector: A Transformational Role for Coal with Biomass*, NREL, Editor. 2007.

7. Huber, G.W., S. Iborra, and A. Corma, *Synthesis of Transportation Fuels from Biomass: Chemistry, Catalysts, and Engineering.* Chemical Reviews, 2006. **106**(9): p. 4044-4098.

8. Milne, T.A., Evans R.J., *Biomass Gasifier "Tars": Their Nature, Formation, and Conversion*, N.R.E. Laboratory, Editor. 1998: Golden Colorado.

9. Abu El-Rub, Z., E.A. Bramer, and G. Brem, *Review of Catalysts for Tar Elimination in Biomass Gasification Processes.* Industrial & Engineering Chemistry Research, 2004. **43**(22): p. 6911-6919.

10. *Biomass Basics*. 2011 12/29/2011]; Available from: http://www1.eere.energy.gov/biomass/biobasics.html.

11. *Biomass Explained*. 2010; Available from: http://www.eia.gov/energyexplained/index.cfm?page=biomass_home.

12. Morehead, H., *Price of Siemens 2 SFG-500 Gasifiers*, T. Roberge, Editor. 2011: Tampa.

13. Roberge, T., Thomas, J., Macpherson, M., Payl, R., Hagedorn, T., Indargiri, K., *Integrated Clean Coal Solutions: Combination Gasification and Fischer-Tropsch Plant Preliminary Case-Study*. 2011, University of South Florida.

14. EIA. *Petroleum & Other Liquids*. 2012 01/02/2012 [cited 2012 01/07/2012]; Available from: http://205.254.135.7/dnav/pet/pet_pri_gnd_dcus_nus_w.htm.

15. *OIL-PRICE.NET*. 2012 01/12/2012; Available from: http://www.oil-price.net/.

16. Ciferno, J., Marano, J., *Benchmarking Biomass Gasification Technologies for Fuels, Chemicals, and Hydrogen Production*, DOE/NREL, Editor. 2002.

17. NREL. *Biomass Maps*. 2011; Available from: http://www.nrel.gov/gis/images/map_biomass_total_us.jpg.

18. Farrauto, R., et al., *NEW MATERIAL NEEDS FOR HYDROCARBON FUEL PROCESSING: Generating Hydrogen for the PEM Fuel Cell.* Annual Review of Materials Research, 2003. **33**(1): p. 1-27.

19. Jensen, S.H., P.H. Larsen, and M. Mogensen, *Hydrogen and synthetic fuel production from renewable energy sources.* International Journal of Hydrogen Energy, 2007. **32**(15): p. 3253-3257.

20. Meher Kotay, S. and D. Das, *Biohydrogen as a renewable energy resource—Prospects and potentials.* International Journal of Hydrogen Energy, 2008. **33**(1): p. 258-263.

21. Boyles, D.T., *Bio-energy : technology, thermodynamics, and costs / David T. Boyles*. Ellis Horwood series in energy and fuel science. 1984, Chichester, West Sussex : New York: E. Horwood; Halsted Press.

22. Tseng, P., J. Lee, and P. Friley, *A hydrogen economy: opportunities and challenges.* Energy, 2005. **30**(14): p. 2703-2720.

23. Chapman, T., *The hydrogen economy blasts off.* Physics World, 2003. **July**: p. 152.

24. T-Raissi, A. and D.L. Block, *Hydrogen: automotive fuel of the future.* Power and Energy Magazine, IEEE, 2004. **2**(6): p. 40-45.

25. I, K., *An overview of the IAEA HEEP software and international programmes on hydrogen production using nuclear energy.* International Journal of Hydrogen Energy, 2011. **36**(6): p. 4125-4129.

26. Yildiz, B. and M.S. Kazimi, *Efficiency of hydrogen production systems using alternative nuclear energy technologies.* International Journal of Hydrogen Energy, 2006. **31**(1): p. 77-92.

27. *NATIONAL HYDROGEN ENERGY ROADMAP NATIONAL HYDROGEN ENERGY ROADMAP*, D.o. Energy, Editor. 2002, Department of Energy. p. 7.

28. Armor, J.N., *Catalysis and the hydrogen economy.* Catalysis Letters, 2005. **101**(3): p. 131-135.

29. Mendes, D., et al., *The water-gas shift reaction: from conventional catalytic systems to Pd-based membrane reactors—a review.* Asia-Pacific Journal of Chemical Engineering, 2010. **5**(1): p. 111-137.

30. Mond, L., Langer,C., *Improvements in Obtaining Hydrogen*. 1888: United Kingdom.

31. Modak, J., *Haber process for ammonia synthesis.* Resonance, 2002. **7**(9): p. 69-77.

32. Ladebeck, J.R. and J.P. Wagner, *Catalyst development for water–gas shift*, in *Handbook of Fuel Cells*. 2010, John Wiley & Sons, Ltd.

33. Ratnasamy, C. and J.P. Wagner, *Water Gas Shift Catalysis.* Catalysis Reviews, 2009. **51**(3): p. 325-440.

34. Van Der Laan, G.P. and A.A.C.M. Beenackers, *Kinetics and Selectivity of the Fischer–Tropsch Synthesis: A Literature Review.* Catalysis Reviews, 1999. **41**(3-4): p. 255-318.

35. Moe, J.M., *Design of water-gas shift reactors.* Chem. Eng. Prog.; (United States); 58:3, 1962: p. Medium: X; Size: Pages: 33-6.

36. Smith, J.M., H.C. Van Hess, and H.C. Van Ness, *Introduction to chemical engineering thermodynamics / J.M. Smith, H.C. Van Ness*. 4th ed. McGraw-Hill chemical engineering series. 1987, New York: McGraw-Hill.

37. Newsome, D.S., *The Water-Gas Shift Reaction.* Catalysis Reviews, 1980. **21**(2): p. 275-318.

38. Bosch, C., Wild, Wilhelm, *Production d'Hydrogene*. 1914: Canada.

39. Venugopal, A., et al., *The gold–ruthenium–iron oxide catalytic system for the low temperature water–gas-shift reaction: The examination of gold–ruthenium interactions.* Applied Catalysis A: General, 2003. **245**(1): p. 149-158.

40. Bohlbro, H., *The kinetics of the water-gas conversion IV. Influence of alkali on the rate equation.* Journal of Catalysis, 1964. **3**(3): p. 207-215.

41. Lloyd, L., D.E. Ridler, and M.V. Twigg, *The water gas shift reaction, Catalyst Handbook*. 1996. 283.

42. Cheah, S., D.L. Carpenter, and K.A. Magrini-Bair, *Review of Mid- to High-Temperature Sulfur Sorbents for Desulfurization of Biomass- and Coal-derived Syngas.* Energy & Fuels, 2009. **23**(11): p. 5291-5307.

43. Flytzani-Stephanopoulos, M., M. Sakbodin, and Z. Wang, *Regenerative Adsorption and Removal of H2S from Hot Fuel Gas Streams by Rare Earth Oxides.* Science, 2006. **312**(5779): p. 1508-1510.

44. Zhang, L., J.-M.M. Millet, and U.S. Ozkan, *Deactivation characteristics of Fe–Al–Cu water-gas shift catalysts in the presence of H2S.* Journal of Molecular Catalysis A: Chemical, 2009. **309**(1-2): p. 63-70.

45. Hla, S.S., et al., *Investigation of the effect of H2S on the performance of an iron/chromium-based high-temperature water–gas shift catalyst using simulated coal-derived syngas.* Catalysis Communications, 2009. **10**(6): p. 967-970.

46. Hakkarainen, R., T. Salmi, and R.L. Keiski, *Water-gas shift reaction on a cobalt-molybdenum oxide catalyst.* Applied Catalysis A: General, 1993. **99**(2): p. 195-215.

47. Liu, B., A. Goldbach, and H. Xu, *Sour water-gas shift reaction over Pt/CeO2 catalysts.* Catalysis Today, 2011. **171**(1): p. 304-311.

48. Copperthwaite, R.G., et al., *Cobalt Chromium Oxide: A Novel Sulphur Tolerant Water-Gas Shift Catalyst.* Applied Catalysis, 1990. **63**(1): p. L11-L16.

49. Mellor, J.R., R.G. Copperthwaite, and N.J. Coville, *The selective influence of sulfur on the performance of novel cobalt-based water-gas shift catalysts.* Applied Catalysis A: General, 1997. **164**(1-2): p. 69-79.

50. *Hydrogen from Coal Program Research, Development, and Demonstration Plan for the Period 2008 through 2016, External Draft, September 2009*, O.o.F.E. Department of Energy, National Energy Technology Laboratory, Editor. 2009. p. 18-20.

51. Ratnasamy, P. and S. Sivasanker, *Structural Chemistry of Co-Mo-Alumnina Catalysts.* Catalysis Reviews, 1980. **22**(3): p. 401-429.

52. de la Osa, A.R., et al., *Performance of a sulfur-resistant commercial WGS catalyst employing industrial coal-derived syngas feed.* International Journal of Hydrogen Energy, 2011. **36**(1): p. 44-51.

53. Andreev, A.A., V.J. Kafedjiysky, and R.M. Edreva-Kardjieva, *Active forms for water-gas shift reaction on NiMo-sulfide catalysts.* Applied Catalysis A: General, 1999. **179**(1-2): p. 223-228.

54. Nikolova, D., R. Edreva-Kardjieva, and T. Grozeva, *Water–gas shift activity of K-promoted (Ni)Mo/γ-Al2O3 systems in sulfur-containing feed.* Reaction Kinetics, Mechanisms and Catalysis, 2011. **103**(1): p. 71-86.

55. Wang, H., et al., *MgO–Al2O3 Mixed Oxides-Supported Co–Mo-Based Catalysts for High-Temperature Water–Gas Shift Reaction.* Catalysis Letters, 2008. **126**(1): p. 100-105.

56. Lian, Y., et al., *Potassium-decorated active carbon supported Co-Mo-based catalyst for water-gas shift reaction.* Journal of Natural Gas Chemistry, 2011. **20**(1): p. 77-83.

57. Hou, P., D. Meeker, and H. Wise, *Kinetic studies with a sulfur-tolerant water gas shift catalyst.* Journal of Catalysis, 1983. **80**(2): p. 280-285.

58. Hutchings, G.J., et al., *A comparative evaluation of cobalt chromium oxide, cobalt manganese oxide, and copper manganese oxide as catalysts for the water-gas shift reaction.* Journal of Catalysis, 1992. **137**(2): p. 408-422.

59. Laniecki, M. and W. Zmierczak, *Deactivation of Sulfur Tolerant Water-Gas Shift Catalysts Based on Ni-Mo-Y-Zeolites*, in *Studies in Surface Science and Catalysis*, H.B. Calvin and B.B. John, Editors. 1991, Elsevier. p. 799-802.

60. Yates, I.C. and C.N. Satterfield, *Intrinsic kinetics of the Fischer-Tropsch synthesis on a cobalt catalyst.* Energy & Fuels, 1991. **5**(1): p. 168-173.

61. Gottschalk, F.M. and G.J. Hutchings, *Manganese oxide water--gas shift catalysts initial optimization studies.* Applied Catalysis, 1989. **51**(1): p. 127-139.

62. Fornasari, G., et al., *Cobalt mixed spinels as catalysts for the synthesis of hydrocarbons.* Industrial & Engineering Chemistry Research, 1987. **26**(8): p. 1500-1505.

63. Lausche, A.C., J.A. Schaidle, and L.T. Thompson, *Understanding the effects of sulfur on Mo2C and Pt/Mo2C catalysts: Methanol steam reforming.* Applied Catalysis A: General, 2011. **401**(1-2): p. 29-36.

64. Laniecki, M. and M. Ignacik, *Water-gas shift reaction over sulfided molybdenum catalysts supported on TiO2-ZrO2 mixed oxides support characterization and catalytic activity.* Catalysis Today, 2006. **116**(3): p. 400-407.

65. Valsamakis, I. and M. Flytzani-Stephanopoulos, *Sulfur-tolerant lanthanide oxysulfide catalysts for the high-temperature water-gas shift reaction.* Applied Catalysis B: Environmental, 2011. **106**(1-2): p. 255-263.

66. Xue, E., M. O'Keeffe, and J.R.H. Ross, *A study of Pt/ZrO2 catalysts for water-gas shift reaction in the presence of H2S*, in *Studies in Surface Science and Catalysis*, F.V.M.S.M. Avelino Corma and G.F. José Luis, Editors. 2000, Elsevier. p. 3813-3818.

67. Bunluesin, T., R.J. Gorte, and G.W. Graham, *Studies of the water-gas-shift reaction on ceria-supported Pt, Pd, and Rh: Implications for oxygen-storage properties.* Applied Catalysis B: Environmental, 1998. **15**(1-2): p. 107-114.

68. Gorte, R.J., *Ceria in catalysis: From automotive applications to the water–gas shift reaction.* AIChE Journal, 2010. **56**(5): p. 1126-1135.

69. Mogensen, M., N.M. Sammes, and G.A. Tompsett, *Physical, chemical and electrochemical properties of pure and doped ceria.* Solid State Ionics, 2000. **129**(1-4): p. 63-94.

70. Trovarelli, A., *Catalytic Properties of Ceria and CeO2-Containing Materials.* Catalysis Reviews, 1996. **38**(4): p. 439-520.

71. Tabakova, T., et al., *FTIR study of low-temperature water-gas shift reaction on gold/ceria catalyst.* Applied Catalysis A: General, 2003. **252**(2): p. 385-397.

72. Li, Y., Q. Fu, and M. Flytzani-Stephanopoulos, *Low-temperature water-gas shift reaction over Cu- and Ni-loaded cerium oxide catalysts.* Applied Catalysis B: Environmental, 2000. **27**(3): p. 179-191.

73. Jacobs, G., et al., *Water-gas shift: in situ spectroscopic studies of noble metal promoted ceria catalysts for CO removal in fuel cell reformers and mechanistic implications.* Applied Catalysis A: General, 2004. **262**(2): p. 177-187.

74. Reddy, G.K., P. Boolchand, and P.G. Smirniotis, *Sulfur tolerant metal doped Fe/Ce catalysts for high temperature WGS reaction at low steam to CO ratios – XPS and Mössbauer spectroscopic study.* Journal of Catalysis, 2011. **282**(2): p. 258-269.

75. Tanaka, Y., et al., *Water gas shift reaction over Cu-based mixed oxides for CO removal from the reformed fuels.* Applied Catalysis A: General, 2003. **242**(2): p. 287-295.

76. Boisen, A., et al., *Support effects and catalytic trends for water gas shift activity of transition metals.* Journal of Molecular Catalysis A: Chemical, 2010. **315**(2): p. 163-170.

77. Jacobs, J.P., et al., *The Surface of Catalytically Active Spinels.* Journal of Catalysis, 1994. **147**(1): p. 294-300.

78. Zhu, J. and Q. Gao, *Mesoporous MCo2O4 (M=Cu, Mn and Ni) spinels: Structural replication, characterization and catalytic application in CO oxidation.* Microporous and Mesoporous Materials, 2009. **124**(1–3): p. 144-152.

79. Hutchings, G.J., et al., *Cobalt-manganese oxide water-gas shift catalysts. A kinetic and mechanistic study.* Journal of the Chemical Society, Faraday Transactions 1: Physical Chemistry in Condensed Phases, 1989. **85**(2): p. 363-371.

80. Gottschalk, F.M., et al., *Cobalt/manganese oxide water gas shift catalysts: I. Competition Between Carbon Monoxide Hydrogenation and Water Gas Shift Activity.* Applied Catalysis, 1988. **38**(1): p. 103-108.

81. Prins, R., V.H.J. De Beer, and G.A. Somorjai, *Structure and Function of the Catalyst and the Promoter in Co—Mo Hydrodesulfurization Catalysts.* Catalysis Reviews, 1989. **31**(1-2): p. 1-41.

82. Grenoble, D.C., M.M. Estadt, and D.F. Ollis, *The chemistry and catalysis of the water gas shift reaction : 1. The kinetics over supported metal catalysts.* Journal of Catalysis, 1981. **67**(1): p. 90-102.

83. Mamontov, E., et al., *Lattice Defects and Oxygen Storage Capacity of Nanocrystalline Ceria and Ceria-Zirconia.* The Journal of Physical Chemistry B, 2000. **104**(47): p. 11110-11116.

84. Fu, Q., et al., *Activity and stability of low-content gold-cerium oxide catalysts for the water-gas shift reaction.* Applied Catalysis B: Environmental, 2005. **56**(1-2): p. 57-68.

85. Fu, Q., A. Weber, and M. Flytzani-Stephanopoulos, *Nanostructured Au–CeO2 Catalysts for Low-Temperature Water–Gas Shift.* Catalysis Letters, 2001. **77**(1): p. 87-95.

86. Qi, X. and M. Flytzani-Stephanopoulos, *Activity and Stability of Cu−CeO2 Catalysts in High-Temperature Water−Gas Shift for Fuel-Cell Applications.* Industrial & Engineering Chemistry Research, 2004. **43**(12): p. 3055-3062.

87. Centeno, M.A., et al., *Catalytic combustion of volatile organic compounds on Au/CeO2/Al2O3 and Au/Al2O3 catalysts.* Applied Catalysis A: General, 2002. **234**(1–2): p. 65-78.

88. Sachtler, J.W.A., J.M. Kool, and V. Ponec, *The role of carbon in methanation by cobalt and ruthenium.* Journal Name: J. Catal.; (United States); Journal Volume: 56:2, 1979: p. Medium: X; Size: Pages: 284-286.

89. Vincent, A.L., et al., *Promotion of activation of CH4 by H2S in oxidation of sour gas over sulfur tolerant SOFC anode catalysts.* Applied Catalysis B: Environmental, 2011. **106**(1-2): p. 114-122.

90. *Hydrogen from Coal Research*. 2011; Available from: http://www.fe.doe.gov/programs/fuels/hydrogen/Hydrogen_from_Coal_R%26D.html.

91. Grange, P., *Catalytic Hydrodesulfurization.* Catalysis Reviews, 1980. **21**(1): p. 135-181.

92. Pechini, M., *Method of preparing lead and alkaline earth titanates and niobates and coating methods using the same to form a capacitor*. 1967: U.S.

93. Nishio, K., Tsuchiya, T., , *Sol-Gel Processing*, in *Handbook of Sol-Gel Science and Technology: Processing Characterization and Applications*, S. Sakko, Editor. 2005, Kluwer Academic Publishers: New York. p. 59-66.

94. Green, D.W. and R.H. Perry, *Perry's chemical engineers' handbook*. 8th ed. / prepared by a staff of specialists under the editorial direction of editor-in-chief, Don W. Green, late editor, Robert H. Perry. ed. 2008, New York: McGraw-Hill.

95. Caldwell, T.E., I.M. Abdelrehim, and D.P. Land, *Thiophene decomposition on Pd(111) forms S and C4 species: a laser-induced thermal desorption/Fourier transform mass spectrometry study.* Surface Science, 1996. **367**(1): p. L26-L31.

96. Simon, L.J., et al., *Thiophene decomposition on Pt-supported zeolites: a TPD study.* Applied Catalysis A: General, 2001. **218**(1–2): p. 161-170.

97. Babich, I.V. and J.A. Moulijn, *Science and technology of novel processes for deep desulfurization of oil refinery streams: a review□.* Fuel, 2003. **82**(6): p. 607-631.

98. Bligaard, T., et al., *The Brønsted–Evans–Polanyi relation and the volcano curve in heterogeneous catalysis.* Journal of Catalysis, 2004. **224**(1): p. 206-217.

99. Brunauer, S., P.H. Emmett, and E. Teller, *Adsorption of Gases in Multimolecular Layers.* Journal of the American Chemical Society, 1938. **60**(2): p. 309-319.

100. Bragg, W.L., *The structure of some crystals as indicated by their diffraction of X-rays.* Proc. R. Soc. London Ser. A, 1913. **89**: p. 248-277.

101. Shou-Yong, J., et al., *Investigation on lattice constants of Mg-Al spinels.* Journal of Materials Science Letters, 2000. **19**(3): p. 225-227.

102. M.F, Z., *Investigation of lattice constant, sintering and properties of nano Mg–Al spinels.* Materials Science and Engineering: A, 2004. **382**(1–2): p. 362-370.

103. Malavasi, L., et al., *High pressure X-ray diffraction study of MgMn2O4 tetragonal spinel.* Nuclear Instruments and Methods in Physics Research Section B: Beam Interactions with Materials and Atoms, 2005. **238**(1–4): p. 171-174.

104. Langford, J.I., D. Louer, and P. Scardi, *Effect of a crystallite size distribution on X-ray diffraction line profiles and whole-powder-pattern fitting.* Journal of Applied Crystallography, 2000. **33**(3 Part 2): p. 964-974.

APPENDICES

Appendix I: WGS Equilibrium Calculations

The following set of equations was used to solve the WGS equilibrium conversion via Microsoft Excel.

$$\frac{\Delta G^{\circ}}{RT} = \frac{\Delta G_0^{\circ} - \Delta H_0^{\circ}}{RT_0} + \frac{\Delta H_0^{\circ}}{RT} + \frac{1}{T}\int_{T_0}^{T} \frac{\Delta C_P^{\circ}}{R} dT - \int_{T_0}^{T} \frac{\Delta C_P^{\circ}}{R} \frac{dT}{T}$$

Recalling the relationship for C_P:

$$\frac{\Delta C_P^{\circ}}{R} = a + bT + cT^2 + dT^{-2}$$

The following equations are used in calculating ΔC_P values:

$$a = \sum_i^N \nu_i * a_i$$

$$b = \sum_i^N \nu_i * b_i$$

$$c = \sum_i^N \nu_i * c_i$$

$$d = \sum_i^N \nu_i * d_i$$

The integrals were evaluated as such:

Appendix I (Continued)

$$\int_{T_0}^{T} \frac{\Delta C_P^{\circ}}{R} dT = (aT + b\frac{T^2}{2} + c\frac{T^3}{3} - dT^{-1}]_{T_0}^{T}$$

$$\int_{T_0}^{T} \frac{\Delta C_P^{\circ}}{R} \frac{dT}{T} = (a \cdot ln(T) + bT + c\frac{T^2}{2} - \frac{1}{2} dT^{-2}]_{T_0}^{T}$$

Recalling the relationship for Gibbs free energy:

$$-\Delta G^{\circ} = RTln(K)$$

For a stoichiometric feed the equilibrium calculation was thus calculated:

$$X = \frac{1}{\frac{1}{\sqrt{K}} + 1}$$

Appendix I (Continued)

Table I.1: Thermodynamic data and constants for WGS.

		Specie	Specie	Specie	Specie	
Property	**Units**	**CO**	**H_2O**	**CO_2**	**H_2**	**Δ**
Stoich Coefficient		-1	-1	1	1	
Inlet flow	mol/min	7.03682E-05	6.95054E-05	0	0	
Outlet flow		C4*(1-X)	C4*(D4/C4-X)	X	X	
Universal Gas Constant	j/(mol*K)	8.31E+00				
Cp a term/R		3.38E+00	3.47E+00	5.46E+00	3.25E+00	**1.86E+00**
Cp b term/R		5.57E-04	1.45E-03	1.05E-03	4.22E-04	**-5.40E-04**
Cp c term/R		0.00E+00	0.00E+00	0.00E+00	0.00E+00	**0.00E+00**
Cp d term/R		-3.10E-07	1.21E-06	-1.16E-05	8.30E-07	**-1.16E-05**
ΔH°_f (WGS) (T=298 K)	J/mol	-110525	-2.42E+05	-3.94E+05	0.00E+00	**-4.12E+04**
ΔG°_f (WGS) (T=298K)	J/mol	-137149	-2.29E+05	-394359	0.00E+00	**-2.86E+04**
Kp Constants (Ratnasamy)		4.58E+03	4.33E+00			
$(\Delta G^\circ_0-\Delta H^\circ_0)/RT_0$		5.06E+00				

Appendix I (Continued)

Table I.2: Excel calculations for WGS thermodynamic properties.

T	integral $\Delta C_p°/R$	integral $\Delta C_p°/(RT)$	$\Delta G°/RT$	ln(K)	K	X	$\Delta G°$	Kp
298	0.00E+00	0.00E+00	-1.16E+01	1.16E+01	104704.48	0.996919	-2.86E+04	61805.335
299	1.70E+00	5.69E-03	-1.15E+01	1.15E+01	99045.696	0.996833	-2.86E+04	58710.1494
300	3.40E+00	1.14E-02	-1.14E+01	1.14E+01	93729.229	0.996744	-2.86E+04	55789.0746
301	5.09E+00	1.70E-02	-1.14E+01	1.14E+01	88732.323	0.996654	-2.85E+04	53031.3154
302	6.79E+00	2.26E-02	-1.13E+01	1.13E+01	84033.865	0.996562	-2.85E+04	50426.8044
303	8.49E+00	2.82E-02	-1.13E+01	1.13E+01	79614.256	0.996468	-2.84E+04	47966.1496
.	.	.	.	.	.	.	.	.
.	.	.	.	.	.	.	.	.
998	1.06E+03	1.87E+00	-7.16E-01	7.16E-01	2.0456168	0.58852	-5.94E+03	1.29301144
999	1.06E+03	1.87E+00	-7.12E-01	7.12E-01	2.0376434	0.588047	-5.91E+03	1.2870881
1000	1.06E+03	1.87E+00	-7.08E-01	7.08E-01	2.0297196	0.587575	-5.89E+03	1.28120367

Appendix II: Thiophene Equilibrium Calculations

The following set of equations was used to calculate equilibrium calculations. Since the Cp integrals were difficult to solve, numerical methods were employed to complete the calculations. First a successive substitution was attempted to solve for X. Exponential divergence was the result of successive substitution. Because ln (K) was relatively constant at every temperature, a sum of the squares method was subsequently employed. Equilibrium conversion as a function of temperature could thus be extracted.

$$\frac{\Delta G^\circ}{RT} = \frac{\Delta G_0^\circ - \Delta H_0^\circ}{RT_0} + \frac{\Delta H_0^\circ}{RT} + \frac{1}{T}\int_{T_0}^{T} \frac{\Delta C_P^\circ}{R} dT - \int_{T_0}^{T} \frac{\Delta C_P^\circ}{R} \frac{dT}{T}$$

The equation used for C_P was the following:

$$C_P = a + b\left[\frac{\frac{c}{T}}{\sin\left(\frac{c}{T}\right)}\right]^2 + d\left[\frac{\frac{e}{T}}{\cos\left(\frac{e}{T}\right)}\right]^2$$

The following equations are used in calculating ΔC_P values:

$$a = \sum_i^N \nu_i * a_i$$

$$b = \sum_i^N \nu_i * b_i$$

Appendix II (Continued)

$$c = \sum_{i}^{N} \nu_i * c_i$$

$$d = \sum_{i}^{N} \nu_i * d_i$$

$$e = \sum_{i}^{N} \nu_i * e_i$$

Because this integral was difficult to solve, it was solved numerically in two parts via the trapezoidal rule. It was solved cumulatively.

Recalling that Equilibrium constant:

$$K_C = \frac{[H_2S]^1[C_4H_8]^1}{[C_4H_4S]^1[H_2]^3}$$

The long form of this equation is thus:

$$K_C = \frac{[\frac{F_T X}{v_0(1+\varepsilon X)}]^1[\frac{XF_T}{v_0(1+\varepsilon X)}]^1}{[\frac{F_T(1-X)}{v_0(1+\varepsilon X)}]^1[\frac{F_T(\frac{F_H}{F_T}-3X)}{v_0(1+\varepsilon X)}]^3}$$

Solving for X to attempt a successive substitution method:

$$X = 1 - \frac{F_T X^2 (v_0(1+\varepsilon X))^2}{K_C(F_H - 3F_T X)^3}$$

After immediate divergence, K_C was simplified:

Appendix II (Continued)

$$K_C = \frac{F_T X^2 (v_0(1+\varepsilon X))^2}{(1-X)(F_H - 3F_T X)^3}$$

The Equilibrium constant was already solved for via

$$K = K_\gamma K_P$$

K_γ is 1 to for ideal gases. It also cancels out the units for K_P.

$$K_P = K_C (RT)^\delta$$

K_C was solved for via filling in all its properties and summing the squares and adding the temperature dependence of K_P.

Appendix II (Continued)

Table II.1: Thermodynamic data and constants for decomposition of thiophene.

Property	Units	C_4H_4S	H_2	H_2S	C_4H_8	Δ
Stoich Coefficient		-1	-3	1	1	-2
Inlet flow	mol/min	4.70E-06	0.002232	0	0	
Inlet flow (high H_2S)	mol/min	7.044E-06				
R	cm^3atm/(mol*K)	82.05746				
R	J/(kmol *K)	8.31E+03				
Cp a term	J/(kmol *K)	4.04E-06	2.76E-06	3.33E-06	6.00E-06	-3.00E-06
Cp b term	J/(kmol *K)	1.63E-05	9.56E-07	2.61E-02	2.08E-05	2.61E-02
Cp c term	J/(kmol *K)	1.46E-03	2.47E-03	9.12E-04	1.59E-03	-6.35E-03
Cp d term	J/(kmol *K)	1.32E-05	3.76E-07	-1.80E-06	1.29E-05	-3.20E-06
Cp e term	J/(kmol *K)	6.49E+02	5.68E+02	9.49E+02	7.07E+02	-6.95E+02
ΔH°_f (Tref =298.15 K)	J/kmol	1.15E-06	0	-2.06E-07	-5.40E-09	-1.37E-06
ΔG°_f (Tref =298.15 K)	J/kmol	1.27E-06	0	-3.34E-07	7.03E-07	-8.98E-07
v_0 (ccm)	Epsilon					
201	-0.0042					
201.5	-0.00629					

Appendix II (Continued)

Table II.2: Excel calculations for decomposition of thiophene.

											Divergent		Sum of squares		Sum of squares
1.92E-13											Xguess (successive subst)		Low Thio flow		High Thio flow
T	Cp	int Cp (Cumulative)		Cp/T	int Cp/T (cumulative)		ΔG°/RT	ln(K)	K	X guess	0.999999	Kc guess ($cm^3/mol)^2$	Kp (atm^{-2})	Kc guess ($cm^3/mol)^2$	Kp (atm^{-2})
293	2.61E-02	0		8.90E-05	0		-3.69E-13	3.69E-13	1.00E+00	0.9999	-1.72E+07	1.58E+09	2.73E+00	1.58E+09	2.727425046
294	2.61E-02	0.026088091		8.87E-05	8.89E-05		-1.86E-11	1.86E-11	1.00E+00	0.9999	-2.06E+16	1.58E+09	2.71E+00	1.58E+09	2.708902689
295	2.61E-02	0.052176176		8.84E-05	0.000177		-7.28E-11	7.28E-11	1.00E+00	0.9999	-2.47E+25	1.58E+09	2.69E+00	1.58E+09	2.690568375
296	2.61E-02	0.078264256		8.81E-05	0.000266		-1.63E-10	1.63E-10	1.00E+00	0.9999	-2.95E+34	1.58E+09	2.67E+00	1.58E+09	2.672419567
297	2.61E-02	0.104352333		8.78E-05	0.000354		-2.88E-10	2.88E-10	1.00E+00	0.9999	-3.53E+43	1.58E+09	2.65E+00	1.58E+09	2.654453772
298	2.61E-02	0.130440398		8.75E-05	0.000441		-4.47E-10	4.47E-10	1.00E+00	0.9999	-4.23E+52	1.58E+09	2.64E+00	1.58E+09	2.636668537
299	2.61E-02	0.156528461		8.73E-05	0.000529		-6.41E-10	6.41E-10	1.00E+00	0.9999	-5.06E+61	1.58E+09	2.62E+00	1.58E+09	2.619061451
.	.	.	.	.	.	.	.	.	.	.	.	.	.	.	.
.	.	.	.	.	.	.	.	.	.	.	.	.	.	.	.
798	2.61E-02	13.17417374		3.27E-05	0.026138		-1.16E-06	1.16E-06	1.00E+00	0.9999	#NUM!	1.58E+09	3.68E-01	1.58E+09	0.367690393
799	2.61E-02	13.20026122		3.27E-05	0.026171		-1.16E-06	1.16E-06	1.00E+00	0.9999	#NUM!	1.58E+09	3.67E-01	1.58E+09	0.366770592

Appendix II (Continued)

Table II.2 (Continued)

800	**2.61 E-02**	**13.22 63487**		**3.26 E-05**	**0.02 6203**		**- 1.16 E-06**	**1.16 E-06**	**1.00 E+00**	**0.9 999**	**#N UM !**	**1.58 E+09**	**3.66E-01**		**1.58 E+09**	**0.3658 54239**
Sum of squares									508. 0003				5.08E+ 02			508.00 02624
													1.8965 4E-12			1.5803 1E-12

Table II.3: Equilibrium conversion for flowrate of thiophene.

Equ Conv Low Thio flow	Equ Conv High Thio flow
0.989295777	0.983954361

Appendix III: Sample Chromatograms

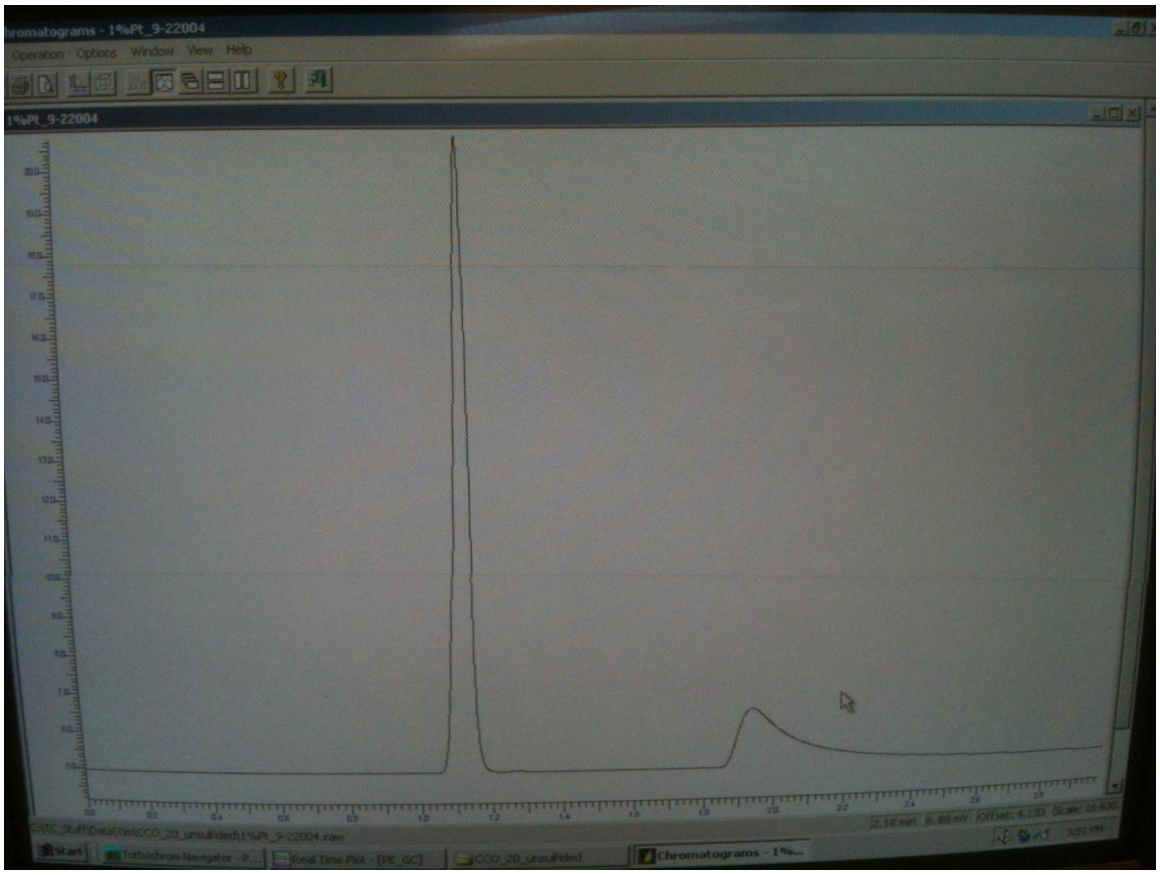

Figure III.1: Sample chromatogram showing inlet base conditions. CO peak is at ~ 1.1. H_2O peak is at ~ 1.9. S/G=1. GHSV = 65,500 hr^{-1}. Flow of reactants = 3.2 cm^3/min.

Appendix III (Continued)

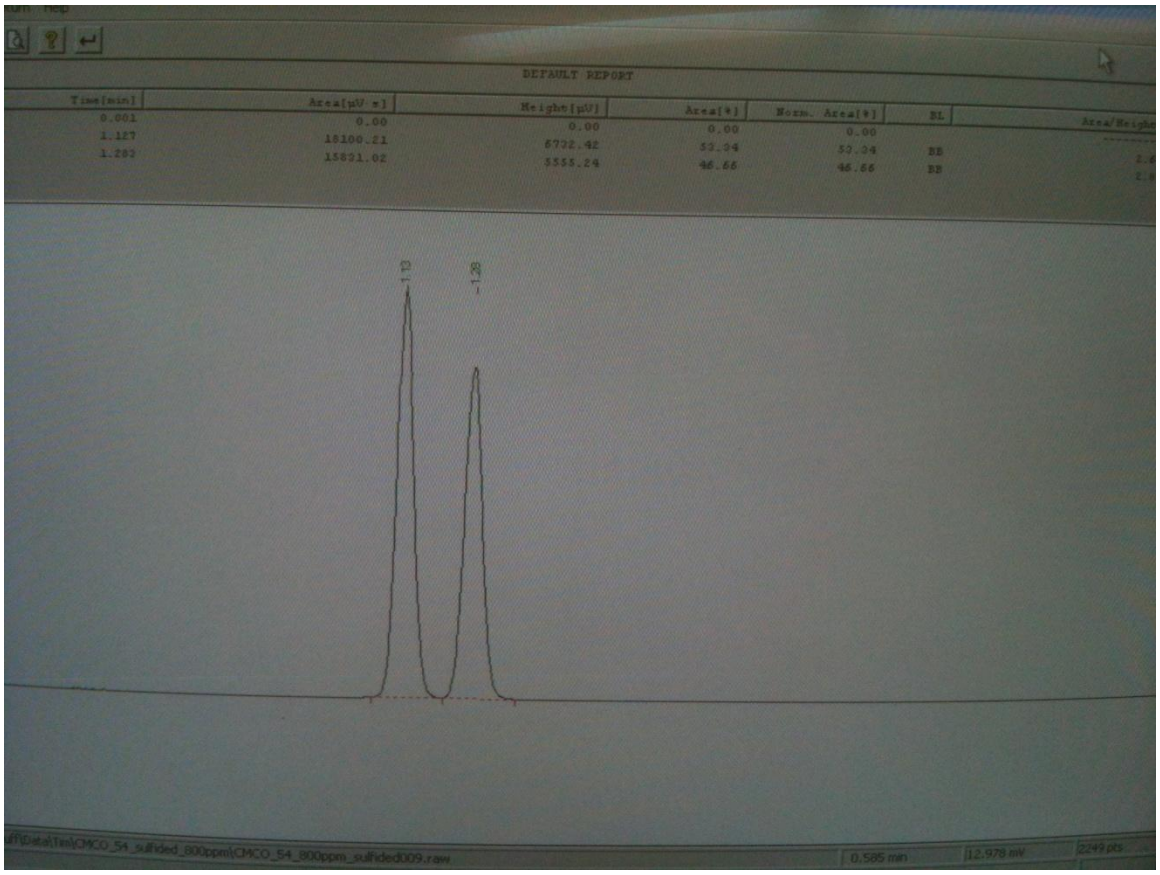

Figure III.2: Sample chromatogram from $Ce_{0.9}Mo_{0.1}Co_2O_4$ sulfided at 800 ppm at 400 °C.

Appendix III (Continued)

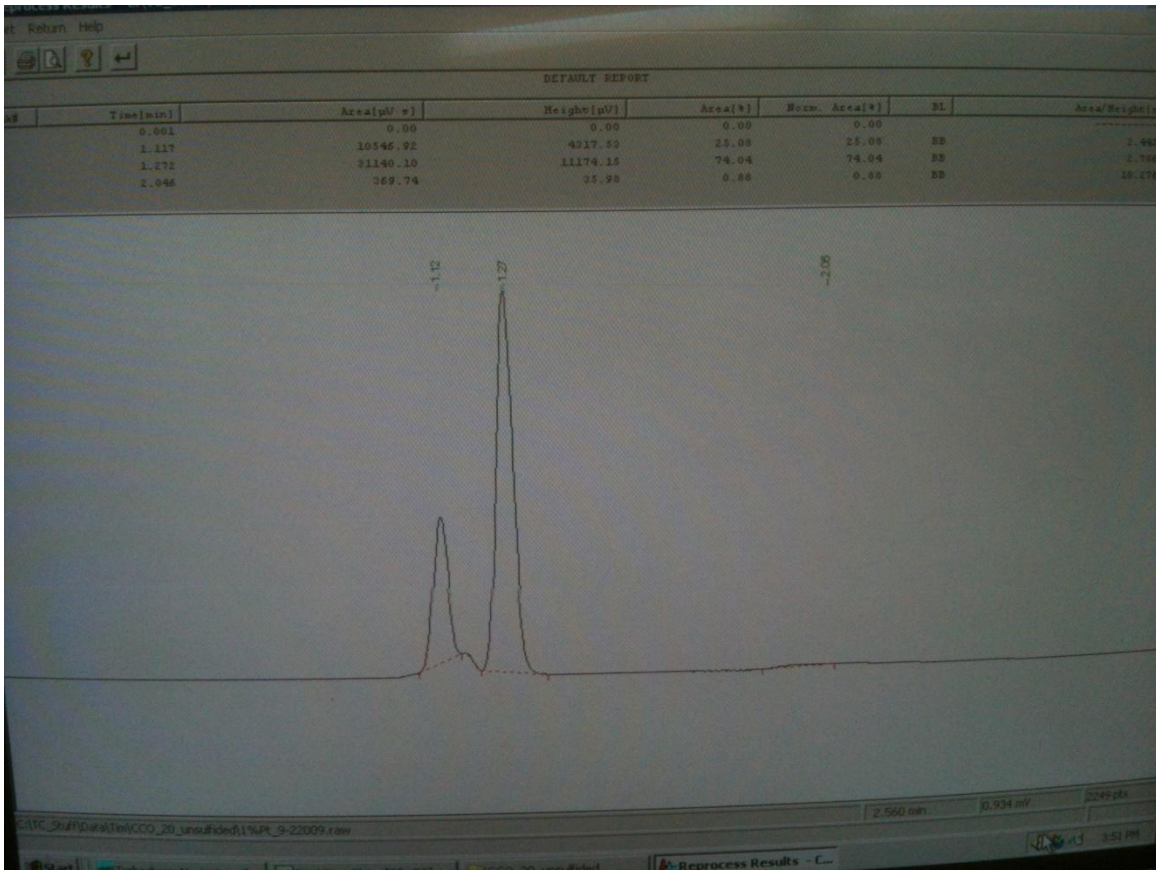

Figure III.3: Sample chromatogram for $CeCo_2O_4$. A slight peak is in-between the CO peak at 1.1 and the CO_2 peak at 1.25. This peak is CO conversion to methane.

Appendix IV: Sample GC Calculations

Table IV.1: Excel conversion calculations for $CeCo_2O_4$.

Baseline		Area	under	peak				F_{CO} (cm^3/min)	F_{H2O} (cm^3/min)	F_{he} (cm^3/min)	F_{He} with sulfur	F_{H2O} calc (mol/min)	wt of CCO (g)	CO calibration Constant	CO_2 calibration Constant	CH_4 calibration Constant	
	Inlet conditions							1.6	1.55	100	0	6.95054E-05	0.1004	15392	17703	12943	
Run	Average CO peak	CO peak	CO_2 peak	H_2O peak	CH_4 peak	CO Conversion (area based)		F_{CO} calc (cm^3/min)	F_{CO2} calc (cm^3/min)		F_{CO} calc (mol/min)	F_{CO2} calc (mol/min)	CO_{base}-CO_{rxn} (mol)	S/G (mol/mol)	ppm H_2S	MW CO	MW H_2O
1	245318	61922	346	64299				4.30041 58			0.00019 1863				0	28.01	18.0166
2	Average CO ccm	24651	0	67551				1.60154 6258			7.1453E-05				P (atm)	R (cm^3*atm*mol^{-1}*K^{-1})	T (K)
3	1.59380197 5	24667	0	69277				1.60258 5759			7.14993E-05				1	82.05746	373.15
4	Average CO mol/min	24397	0	67779				1.58504 4179			7.07167E-05						373.15
5	7.11074E-05	24575	0	72733				1.59660 8628			7.12327E-05						373.15
6	Average S/G (mol/mol)	24369	0	70733				1.58322 5052			7.06356E-05						
	0.9774707 03												CO_{base}- CO_{rxn} (mol)				
400 °C							F_{CH4} calc (cm^3/min)	F_{CO} calc (cm^3/min)	F_{CO2} calc (cm^3/min)	F_{CH4} calc (mol/min)	F_{CO} calc (mol/min)	F_{CO2} calc (mol/min)	CO consumed	Conversion (CO based)	Conversion (CO2 based)	Conversion CH4 based	

Appendix IV (Continued)

Table IV.1 (Continued)

7		**3740**	**150068**	**294**	**0**	**84.75%**	**0.00**	**2.43E-01**	**8.51E-01**	**0.00E+00**	**7.94E-06**	**2.78E-05**	**6.32E-05**	**88.84%**	**39.09%**	**0.00%**	
8		9089	183700	0	0	62.95%	0.00	5.91E-01	1.04E+00	0.00E+00	1.93E-05	3.39E-05	5.18E-05	72.88%	47.66%	0.00%	
9		5893	183522	0	0	75.98%	0.00	3.83E-01	1.04E+00	0.00E+00	1.25E-05	3.39E-05	5.86E-05	82.42%	47.61%	0.00%	
10		6524	180200	0	0	73.41%	0.00	4.24E-01	1.02E+00	0.00E+00	1.38E-05	3.32E-05	5.73E-05	80.53%	46.75%	0.00%	
11		9233	180021	0	0	62.36%	0.00	6.00E-01	1.02E+00	0.00E+00	1.96E-05	3.32E-05	5.15E-05	72.45%	46.75%	0.00%	
12		9564	179555	0	0	61.01%	0.00	6.21E-01	1.01E+00	0.00E+00	2.03E-05	3.31E-05	5.08E-05	71.46%	46.58%	0.00%	
13		6153	183338	0	0	74.92%	0.00	4.00E-01	1.04E+00	0.00E+00	1.31E-05	3.38E-05	5.81E-05	81.64%	47.58%	0.00%	
											1.64E-05		**average**	**76.90%**	**46.00%**	**0.00%**	
350 °C																	
14		5323	203488	0	1637	78.30%	0.13	3.46E-01	1.15E+00	4.13E-06	1.13E-05	3.75E-05	5.98E-05	84.12%	52.79%	5.81%	
15		6157	197779	0	1288	74.90%	0.10	4.00E-01	1.12E+00	3.25E-06	1.31E-05	3.65E-05	5.80E-05	81.63%	51.31%	4.57%	
16		6194	195889	0	1187	74.75%	0.09	4.02E-01	1.11E+00	3.00E-06	1.31E-05	3.61E-05	5.80E-05	81.52%	50.82%	4.21%	
17		5450	203399	0	1510	77.78%	0.12	3.54E-01	1.15E+00	3.81E-06	1.16E-05	3.75E-05	5.95E-05	83.74%	52.77%	5.36%	

Appendix IV (Continued)

Table IV.1 (Continued)

18		**5328**	**202274**	**0**	**1322**	**78.28%**	**0.10**	**3.46 E-01**	**1.15 E+00**	**3.34 E-06**	**1.13 E-05**	**3.74 E-05**	**5.98 E-05**	**84.10 %**	**52.60 %**	**4.69%**	
19		6030	198733	0	1061	75.42%	0.08	3.92 E-01	1.12 E+00	2.68 E-06	1.28 E-05	3.67 E-05	5.83 E-05	82.01 %	51.56 %	3.76%	
										3.37 E-06	1.22 E-05		**average**	**82.85 %**	**51.98 %**	**4.73%**	
300 °C																	
20		7341	197400	0	0	70.08%	0.00	4.77 E-01	1.12 E+00	0.00 E+00	1.56 E-05	3.64 E-05	5.55 E-05	78.09 %	51.21 %	0.00%	
21		7591	192337	0	0	69.06%	0.00	4.93 E-01	1.09 E+00	0.00 E+00	1.61 E-05	3.55 E-05	5.50 E-05	77.35 %	49.91 %	0.00%	
22		7885	195227	0	0	67.86%	0.00	5.12 E-01	1.10 E+00	0.00 E+00	1.67 E-05	3.60 E-05	5.44 E-05	76.47 %	50.66 %	0.00%	
23		8410	187117	0	0	65.72%	0.00	5.46 E-01	1.06 E+00	0.00 E+00	1.78 E-05	3.45 E-05	5.33 E-05	74.91 %	48.56 %	0.00%	
24		7876	191116	0	0	67.89%	0.00	5.12 E-01	1.08 E+00	0.00 E+00	1.67 E-05	3.53 E-05	5.44 E-05	76.50 %	49.59 %	0.00%	
25		7710	192566	0	0	68.57%	0.00	5.01 E-01	1.09 E+00	0.00 E+00	1.64 E-05	3.55 E-05	5.47 E-05	76.99 %	49.96 %	0.00%	
26		8430	185112	0	0	65.64%	0.00	5.48 E-01	1.05 E+00	0.00 E+00	1.79 E-05	3.42 E-05	5.32 E-05	74.85 %	48.03 %	0.00%	
													average	**76.45 %**	**49.70 %**	**0.00%**	

Appendix V: Miller Index Calculations

Spinel Peaks

Table V.1: Miller index calculations for spinel structures.

Peak#	2Θ	$\sin^2\Theta$	1	2	3	$h^2+k^2+l^2$	*hkl*	a (nm)
0	18.92	0.027014	1	2	3	3	111	0.81243
1	28.49	0.06055	2.241433	4.482866	6.724299	7		0.828918
2	31.29	0.072725	2.692144	5.384287	8.076431	8	220	0.808577
3	32.99	0.080617	2.984287	5.968575	8.952862	9		0.814566
4	36.81	0.099687	3.690199	7.380397	11.0706	11	311	0.809836
5	38.51	0.10875	4.025717	8.051434	12.07715	12	222	0.809831
6	41.83	0.127437	4.717446	9.434893	14.15234	14		0.808046
7	44.75	0.144907	5.364179	10.72836	16.09254	16	400	0.810091
8	47.45	0.161883	5.992597	11.98519	17.97779	18		0.812932
11	56.33	0.222796	8.247449	16.4949	24.74235	24	422	0.80015
12	59.33	0.244954	9.067696	18.13539	27.20309	27	511	0.809392
13	65.35	0.291463	10.78938	21.57875	32.36813	32	440	0.807797
14	69.37	0.323834	11.98769	23.97539	35.96308	36	442	0.812847
15	73.37	0.356905	13.21191	26.42382	39.63572	40	620	0.816155
	74.31	0.364784	13.50357	27.00713	40.5107	40	620	0.807293
16	76.87	0.386419	14.30447	28.60895	42.91342	43		0.813249
	78.31	0.398692	14.75877	29.51755	44.27632	44		0.809891
17	79.41	0.40811	15.10742	30.21484	45.32226	45		0.809537

Appendix V (Continued)

Fluorite Peaks

Table V.2: Miller index calculations for fluorite structures.

Peak#	2Θ	$\sin^2\Theta$	1	2	3	$h^2+k^2+l^2$	*hkl*	a (nm)
1	28.49	0.06055	1	2	3	3	111	0.542654
2	31.29	0.072725	1.201081	2.402163	3.603244			0
3	32.99	0.080617	1.331419	2.662839	3.994258	4	200	0.543044
4	36.81	0.099687	1.646357	3.292714	4.939071			0
5	38.51	0.10875	1.796046	3.592092	5.388138			0
6	41.83	0.127437	2.104656	4.209313	6.313969			0
7	44.75	0.144907	2.393192	4.786384	7.179576			0
8	47.45	0.161883	2.673556	5.347113	8.020669	8	220	0.541954
9	56.33	0.222796	3.679543	7.359086	11.03863	11	311	0.541704
10	59.33	0.244954	4.045491	8.090981	12.13647	12	222	0.539595
11	65.35	0.291463	4.813606	9.627213	14.44082			0
12	69.37	0.323834	5.348227	10.69645	16.04468	16	400	0.541898
13	73.37	0.356905	5.894402	11.7888	17.68321			0
14	76.87	0.386419	6.381843	12.76369	19.14553	19	331	0.540588
15	79.21	0.406395	6.711748	13.4235	20.13524	20	420	0.540829

Appendix VI: Propogation of Uncertainty for CO Conversion

In order to calculate the propagation of error in CO conversion, it must be known how the flow of CO was calculated. Flow was measured in a GC detector. The uncertainty associated with the flowmeter is ±.1 ccm. The uncertainty associated with the area, as taken by the data collector (Timothy Roberge) was ± 10 μV*s. The following linear relationship was derived to calibrate CO concentration from GC area under the peak.

$$A = 15392f$$

where A = GC area under peak in μV*s, and

f = flow of CO in ccm.

Solving for the calibration constant C_{CO}:

$$C_{CO} = \frac{A}{f}$$

From here the error in the CO calibration constant (C_{CO}) can be calculated:

$$\sigma_{C_{CO}} = \sqrt{(\frac{\partial C_{CO}}{\partial A})^2 \sigma_A^2 + (\frac{\partial C_{CO}}{\partial f})^2 \sigma_f^2}$$

with

$$\frac{\partial C_{CO}}{\partial A} = 1/f$$

Appendix VI (Continued)

$$\frac{\partial C_{CO}}{\partial f} = \frac{-A}{f^2}$$

Choosing f to be 1 ccm and A to be the average 15766.5 the uncertainty in the constant can be further calculated as such:

$$\sigma_{C_{CO}} = \sqrt{(\frac{1}{1})^2\, 10^2 + (\frac{-15766.5}{1^2})^2\, 0.1^2} = 1576.68\ \frac{\mu V * s}{ccm}$$

From this error for calculated flow could be calculated. Since flow was calculated by dividing the GC peak area by the calibration constant, the uncertainty in the flow of CO is given via the following equation:

$$\sigma_{fcalc} = \sqrt{(\frac{\partial f_{calc}}{\partial A})^2\ \sigma_A^2 + (\frac{\partial f_{calc}}{\partial C_{CO}})^2\ \sigma_{C_{CO}}^2}$$

$$\frac{\partial f_{calc}}{\partial A} = \frac{1}{C_{CO}}$$

$$\frac{\partial f_{calc}}{\partial cc} = \frac{-A}{{C_{CO}}^2}$$

A was taken to equal the average inlet area for a given sample ($CeCo_2O_4$) at 15766.5, while the calculated constant was 15392 and the following equation resulted:

$$\sigma_{fcalc} = \sqrt{(\frac{1}{15392})^2\, 10^2 + (\frac{-15766.5}{15392^2})^2\, (1576.65)^2} = 0.105\ ccm$$

Appendix VI (Continued)

This needs to be converted to moles via the ideal gas law; Pressure can be neglected since gauge pressure read 0 for all experiments:

$$\sigma_n = \sqrt{(\frac{\partial n}{\partial T})^2\ \sigma_T^2 + (\frac{\partial n}{\partial f_{calc}})^2\ \sigma_{f_{calc}}^2}$$

where

$$n = \frac{p f_{calc}}{RT}$$

$$\frac{\partial n}{\partial T} = -\frac{p f_{calc}}{RT^2}$$

$$\frac{\partial n}{\partial f_{calc}} = \frac{p}{RT}$$

Taking p to be 1 atm, f_{calc} to be 1.593801975 ccm (from the given sample $CeCo_2O_4$), and T is the GC detector column Temperature of 373 K. Uncertainty in T will be employed here even though the reaction temperature was not used to model reactor flow.

$$\sigma_n = \sqrt{(\frac{-1 * 1.593801975}{82.0575 * 373^2})^2\ 5^2 + (\frac{1}{82.0575 * 373})^2\ (0.105)^2} = 4.0 * 10^{-6}\ \frac{mol}{min}$$

Utilizing the ideal gas law, a simple unit conversion from σ_{fcalc} to σ_n equals 5.0 * 10^{-6} mol/min. However the calculated version of 4.0 * 10^{-6} will be used. Finally CO conversion is a function of f_{calc}:

$$X = \frac{F_{CO,0} - F_{CO}}{F_{CO,0}}$$

Appendix VI (Continued)

Both F_{CO} and $F_{CO,0}$ are calculated flows, therefore σ_n can be used for both differentials.

$$\sigma_X = \sqrt{(\frac{\partial X}{\partial F_{CO,0}})^2\ \sigma_n^2 + (\frac{\partial X}{\partial F_{CO}})^2\ \sigma_n^2}$$

$$\frac{\partial X}{\partial F_{CO,0}} = \frac{F_{CO}}{{F_{CO,0}}^2}$$

$$\frac{\partial X}{\partial F_{CO}} = -\frac{1}{F_{CO}}$$

Using the same experimental conditions as before (unsulfided $CeCo_2O_4$) $F_{CO,0} = 7.111 * 10^{-5}$ mol/min while the average F_{CO} for all experimental runs was $1.512 * 10^{-5}$ mol/min, the uncertainty in conversion can be calculated:

$$\sigma_X = \sqrt{(\frac{1.512 * 10^{-5}}{(7.111 * 10^{-5})^2})^2\ (4.0 * 10^{-6})^2 + (\frac{-1}{7.111 * 10^{-5}})^2\ (4.0 * 10^{-6})^2} = 0.0575$$

Therefore the final uncertainty in conversion is:

$$\sigma_X = 5.8\%$$

Appendix VII: Permissions

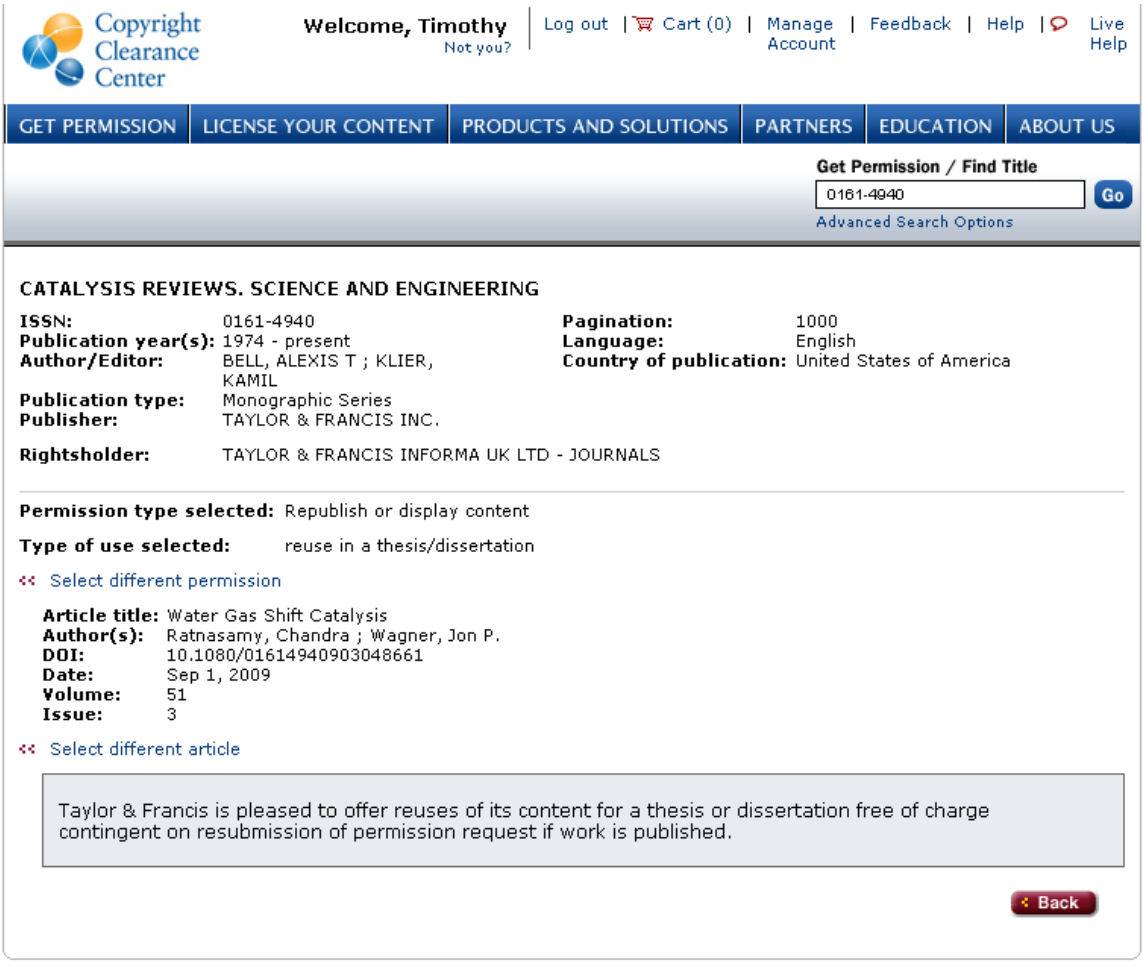

Copyright Clearance Center

Welcome, Timothy
Not you?

Log out | Cart (0) | Manage Account | Feedback | Help | Live Help

GET PERMISSION | LICENSE YOUR CONTENT | PRODUCTS AND SOLUTIONS | PARTNERS | EDUCATION | ABOUT US

Get Permission / Find Title
0161-4940 Go
Advanced Search Options

CATALYSIS REVIEWS. SCIENCE AND ENGINEERING

ISSN:	0161-4940	**Pagination:**	1000
Publication year(s):	1974 - present	**Language:**	English
Author/Editor:	BELL, ALEXIS T ; KLIER, KAMIL	**Country of publication:**	United States of America
Publication type:	Monographic Series		
Publisher:	TAYLOR & FRANCIS INC.		
Rightsholder:	TAYLOR & FRANCIS INFORMA UK LTD - JOURNALS		

Permission type selected: Republish or display content

Type of use selected: reuse in a thesis/dissertation

<< Select different permission

Article title: Water Gas Shift Catalysis
Author(s): Ratnasamy, Chandra ; Wagner, Jon P.
DOI: 10.1080/01614940903048661
Date: Sep 1, 2009
Volume: 51
Issue: 3

<< Select different article

Taylor & Francis is pleased to offer reuses of its content for a thesis or dissertation free of charge contingent on resubmission of permission request if work is published.

Back

Appendix VII (Continued)

This is a License Agreement between Timothy Roberge ("You") and Elsevier ("Elsevier") provided by Copyright Clearance Center ("CCC"). The license consists of your order details, the terms and conditions provided by Elsevier, and the payment terms and conditions.

All payments must be made in full to CCC. For payment instructions, please see information listed at the bottom of this form.

Supplier	Elsevier Limited The Boulevard,Langford Lane Kidlington,Oxford,OX5 1GB,UK
Registered Company Number	1982084
Customer name	Timothy Roberge
Customer address	9415 Crescent Loop Circle #202 Tampa, FL 33619
License number	2837211033373
License date	Jan 27, 2012
Licensed content publisher	Elsevier
Licensed content publication	Journal of Catalysis
Licensed content title	Sulfur tolerant metal doped Fe/Ce catalysts for high temperature WGS reaction at low steam to CO ratios – XPS and Mössbauer spectroscopic study
Licensed content author	Gunugunuri K. Reddy,P. Boolchand,Panagiotis G. Smirniotis
Licensed content date	1 September 2011
Licensed content volume number	282
Licensed content issue number	2
Number of pages	12
Start Page	258
End Page	269
Type of Use	reuse in a thesis/dissertation
Portion	figures/tables/illustrations
Number of figures/tables/illustrations	3
Format	both print and electronic
Are you the author of this Elsevier article?	No
Will you be translating?	No
Order reference number	
Title of your thesis/dissertation	NOVEL BLENDS OF SULFUR-TOLERANT WATER-GAS SHIFT CATALYSTS FOR BIOFUEL APPLICATIONS
Expected completion date	Mar 2012
Estimated size (number of pages)	110
Elsevier VAT number	GB 494 6272 12
Permissions price	0.00 USD
VAT/Local Sales Tax	0.0 USD / 0.0 GBP
Total	0.00 USD